FINAL TECHNICAL REPORT

Project Title: Intelligent Monitoring Systems and Advanced Well Integrity and Mitigation

Award Number: DE-FE-0026517

Date of Report: June 30, 2021

Principal Investigator: Scott McDonald

Authors: Julia Correa, Michael Commer, Shan Dou, Barry Freifeld, Jonathan Ajo-Franklin, Todd Wood, Michelle Robertson, and Scott McDonald

Abstract

Long-term seismic monitoring of carbon capture and storage projects is needed to verify that the injected gas is safely stored in the subsurface until permanence can be assured. Conventional surface seismic monitoring techniques are usually expensive, require highly invasive surface operations, and need significant time investments on the part of personnel for both the field effort and processing the acquired data. For these reasons, permanent reservoir monitoring technologies are preferred, as they can offer a cost-effective solution for long-term monitoring. As part of the monitoring program of the Archer Daniels Midland's large-scale injection of CO_2 in Decatur, Illinois, USA, a continuous seismic monitoring array was installed using a combination of surface orbital vibrator (SOV) sources and fiber-optic cables for distributed acoustic sensing (DAS) acquisition with the objective to build a continuous monitoring array. The aim of the presented project was to build a monitoring array and platform that integrates real-time seismic data with conventional data streams and provides continuous data analysis using dynamic computational models to deliver a comprehensive real-time assessment of subsurface conditions. It is in this context that the Intelligent Monitoring Systems and Advanced Well Integrity and Mitigation project was proposed with the objective to develop an integrated architecture that utilizes a permanent seismic monitoring network, combines the real-time geophysical and process data with reservoir flow and geomechanical models to create a comprehensive monitoring, visualization, and control system that delivers critical information for process surveillance and optimization.

Acknowledgements
Funding for LBNL was provided through the Carbon Storage Program, U.S. DOE, Assistant Secretary for Fossil Energy, Office of Clean Coal and Carbon Management through the NETL, under contract No. DE-FE0026517. The authors wish to acknowledge the contributions of Lawrence Berkeley National Laboratory's Geosciences Measurement Facility (gmf.lbl.gov) and its support of custom instrumentation solutions for earth, energy, and environmental science discovery.

Contents

List of Figures

1 Executive Summary

Archer Daniels Midland Company's (ADM) world scale agricultural processing and biofuels production complex located in Decatur, Illinois is the site for two large scale carbon capture and storage projects. The Illinois Basin-Decatur Project (IBDP) is a large-scale pilot that injected 1,000,000 metric tons of CO_2 over a three-year period (2011-2014) in order to validate the Illinois Basin's capacity to permanently store CO_2. The Illinois Industrial Carbon Capture and Storage Project (ICCS) is an industrial scale project demonstrating the integration of carbon capture and store (CCS) technology at an ethanol plant. The ICCS project has the capacity to inject and store over 1,000,000 metric tons of CO_2 per year. Both projects present a unique opportunity to gather crucial scientific and engineering data to advance CCS technologies and to add to the understanding of large-scale CO_2 storage in saline formations. A map showing the major elements of the ADM CCS facility is shown in Figure 1 and Figure 2 includes a simplified process flow diagram of the CCS operation and the stratigraphic column describing the storage site. In December 2014, the USEPA granted ADM the nation's first UIC Class VI operating permit. Under the Class VI regulatory framework, the permittee must execute project plans ensuring that wells are sited, constructed, operated, tested, monitored, and closed in a manner that is protective of underground sources of drinking water (USDWs). To achieve these program objectives, ADM developed a comprehensive plan to include extensive site characterization, well construction using materials that are compatible with and can withstand contact with CO_2, and comprehensive monitoring of all aspects of well integrity, CO_2 injection and storage, and groundwater quality during the injection operation and the post-injection site care period. With respect to site monitoring, ADM developed an integrated risk-based monitoring plan that combines reservoir modeling with monitoring components such as well integrity, reservoir and process conditions, and changes within the geologic system (i.e. plume size, CO_2 saturation & mobility, pressure front, and ground water quality).

Part of the monitoring plan involves tracking the extent of the carbon dioxide plume and generating data which support and improve the modeling that characterizes the storage site. One method, time-lapse seismic imaging, has been demonstrated as an effective technique for subsurface CO_2 monitoring in both enhanced oil recovery (Lazaratos and Marion, 1997; Wang et al. 1998; Majer et al. 2006; Gritto, et al. 2004) and in sequestration (Skov, 2002). Unfortunately, the use of this technology has significant drawbacks and limitations. To undertake a conventional 3D surface seismic or vertical seismic profile (VSP) survey, one must have an available borehole proximate to the survey area, obtain numerous land access permits, deploy an extensive temporary monitoring network, shoot multiple source locations, and subsequently process and interpret the acquired data. These surveys are exceptionally costly due to the significant deployment of manpower & equipment, landowner payments, and weather-related delays. In January 2015, the IBDP and ICCS projects spent over $3.5 million to conduct a 3D survey covering 3,000 acres. Another drawback is total execution time. Because these surveys require significant pre- and post-survey activities that include land access permitting, data processing, and data interpretation, a single survey can take over six months. Even when considering these drawbacks, the technology has a more

troubling limitation in that it only records a discrete snapshot in time and subsequent surveys are required to generate time-lapse imagery.

To meet the EPA's goal with respect to storing CO_2 in a manner that does not endanger the quality of USDWs, a storage site operator needs a monitoring system that delivers real-time critical information needed for process surveillance and optimization. For seismic technology to be effectively applied to geologic storage (GS) projects, one needs to develop a cost-effective intelligent monitoring system (IMS) that integrates real-time seismic data with conventional data streams and provides continuous data analysis using dynamic computational models to deliver a comprehensive real-time assessment of subsurface conditions. It is in this context that the Intelligent Monitoring Systems and Advanced Well Integrity and Mitigation project was proposed with the objective to develop an integrated IMS architecture that utilizes a permanent seismic monitoring network, and combines the real-time geophysical and process data with reservoir flow and geomechanical models to create a comprehensive monitoring, visualization, and control system that delivers critical information for process surveillance and optimization.

The application of seismic technology including passive microseismic acquisition and stimulation modeling, seismic guided drilling, and borehole seismic interpretation has significantly contributed to reducing the risk and cost of developing resources. Technology advances, novel applications, and real-time data integration strategies are necessary to enable seismic technology to play a significant role in CCS monitoring activities and further the adoption, deployment, and commercialization of CCS technologies. Long-term seismic monitoring of CCS projects is needed to verify that the injected gas is safely stored in the subsurface until permanence can be assured. Conventional surface seismic monitoring techniques are usually expensive, require highly invasive surface operations, and need significant time investments on the part of personnel for both the field effort and processing the acquired data. For these reasons, permanent reservoir monitoring (PRM) technologies are preferred, as they can offer a cost-effective solution for long-term monitoring. As part of the monitoring program of the Archer Daniels Midland's (ADM) large-scale injection of CO_2 in Decatur, Illinois, USA, a continuous seismic monitoring array was installed using a combination of surface orbital vibrator (SOV) sources and fiber-optic cables for distributed acoustic sensing (DAS) acquisition with the objective to build a continuous monitoring array.

Fiber-optic based DAS technology is capable of acquiring continuous on-demand seismic data with fine spatial sampling; because of this, it has become a popular technology in recent years for time-lapse vertical seismic profiling (VSP) (Mateeva et al., 2017). SOV sources are rotary seismic sources that generate horizontally and vertically polarized signals by rotating eccentric weights (Daley & Cox, 2001). SOV source technology is currently at TRL3 to TRL4. DAS sensors coupled with SOV sources have been tested in a variety of field experiments (Ajo-Franklin et al., 2017; Cheng et al., 2021; Correa et al., 2018), with successful applications using offset VSP geometry (Isaenkov et al., 2021).

The objective of the ICCS project is to store 5 million tons of CO_2, while demonstrating the integration of the CO_2 capture facility into the ethanol production plant. The permanent seismic monitoring component of the project aims to integrate the existing monitoring infrastructure on-

site, comprised of a combination of multi-level geophone arrays, pressure gauges, fiber-optic acoustic and temperature sensors, and surface seismic stations (Kaven et al., 2014; Williams-Stroud et al., 2019). DAS/SOV was added to the monitoring program as a potential method to improve the temporal resolution of the infrequent surface seismic acquisitions.

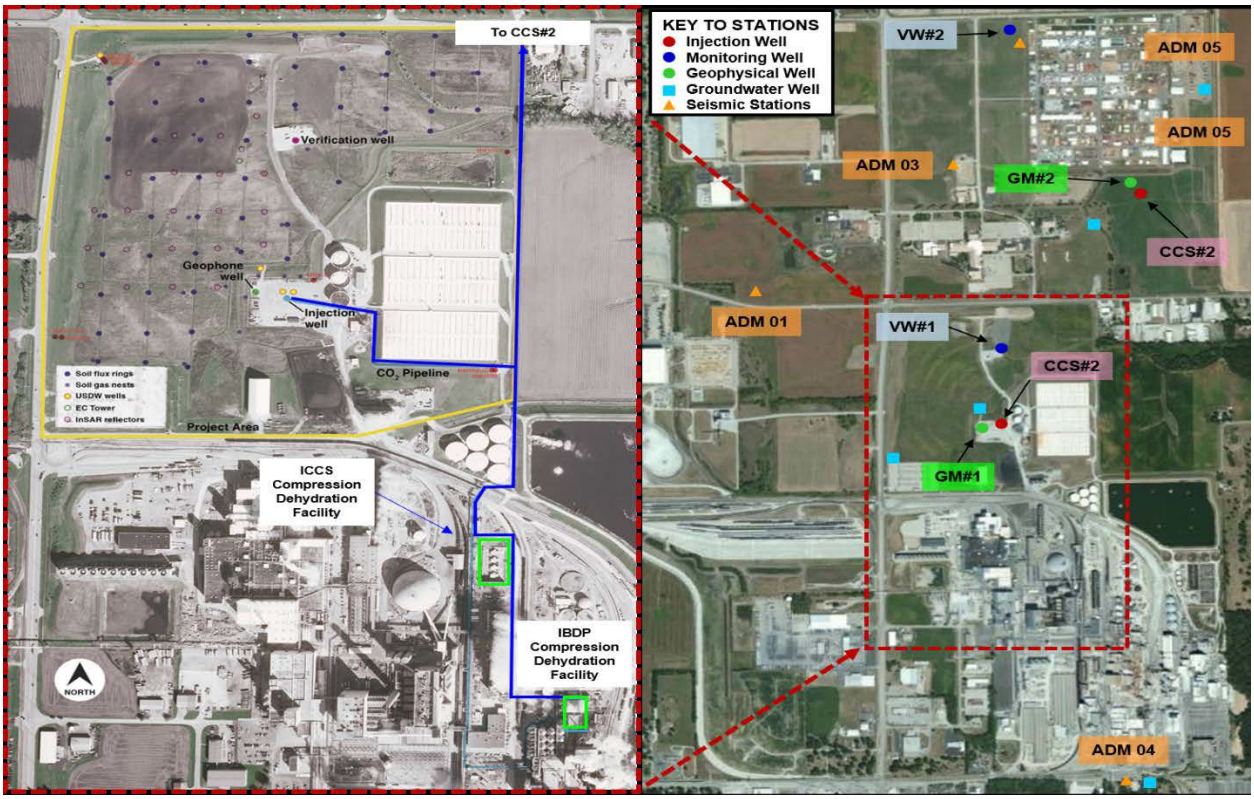

Figure 1. ADM site map showing the locations of the processing units, the transmission pipeline, injection well, and the various monitoring stations throughout the site.

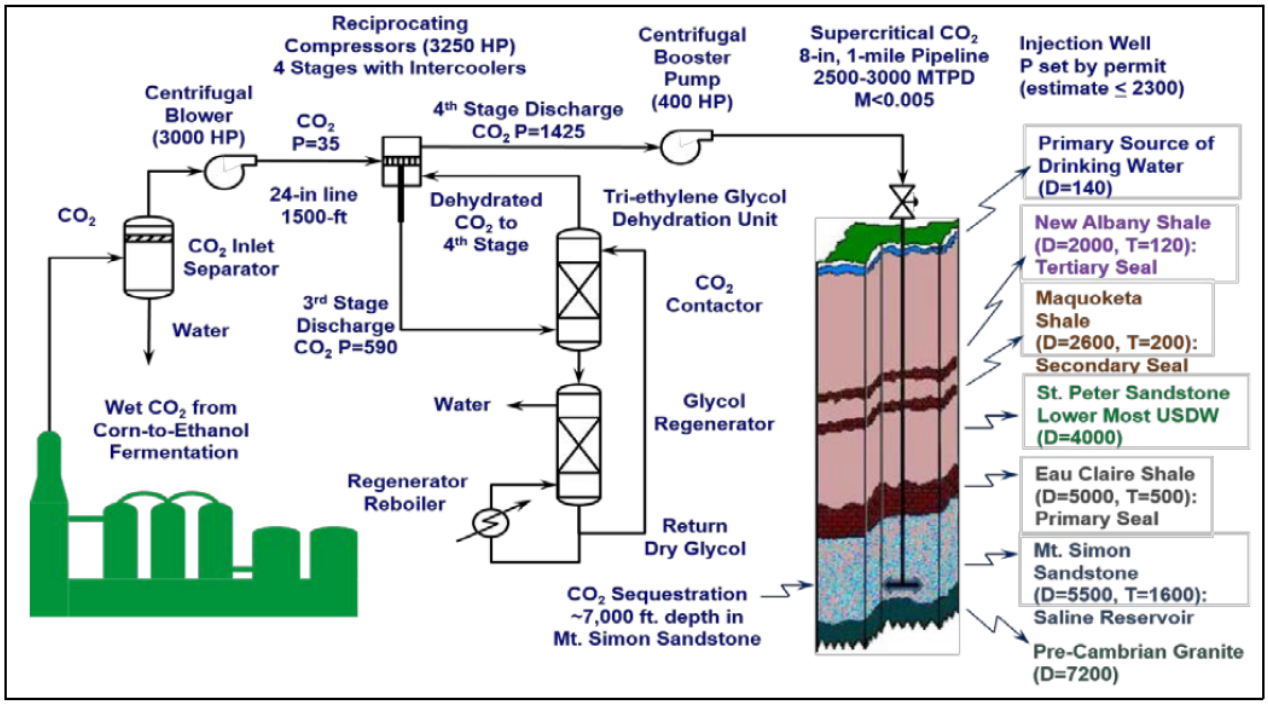

Figure 2. Simplified process flow diagram of the CCS operation and the stratigraphic column detailing key features in the geology at the storage site.

2 Project Goals

The project's primary objective is to develop an integrated IMS architecture that utilizes a permanent seismic monitoring network, combines the real-time geophysical and process data with reservoir flow and geomechanical models to create a comprehensive monitoring, visualization, and control system that delivers critical information for process surveillance and optimization that is specific to geologic storage projects. The IMS will use real-time closed-loop model calibration to provide reliable forecasts of reservoir conditions that allow optimization of operation and maintenance activities. The permanent seismic network will enhance reservoir surveillance by increasing the sensitivity of the monitoring system, improving subsurface resolution, thereby reducing the need for external seismic surveys. The combination of these factors will reduce the cost and risk associated with geologic storage projects. The specific project objective are as follows:

1. Design an IMS using a real-time multi-technology architecture that fully integrates and enhances the site's existing monitoring infrastructure that includes multi-level 3C seismic arrays, distributed acoustic sensing (DAS), multi-level pressure/temperature sensors, distributed temperature sensing (DTS), borehole seismometers, and surface seismic stations

2. Augment the site monitoring capabilities by installing several rotary seismic sources and integrating a network of surface DAS with the existing seismic system to create a continuous active source seismic monitoring (CASSM) array covering over two square kilometers and extending to a depth of 6,300 feet.

3. Develop terabyte-level data processing solutions for real time monitoring of reservoir conditions and time lapse imaging of the CO_2 plume.

4. Commission and operate the monitoring system in an industrial setting under actual conditions.

5. Validate and document the economic and environmental benefits of the monitoring system.

6. Update the monitoring verification and accounting best practices guide to include IMS and CASSM monitoring systems.

7. Incorporate DAS channels in routine location of microseismicity using the combination of borehole and surface seismic stations.

8. Develop near real-time data processing techniques to overcome the passive seismic monitoring limitations of low signal-to-noise ratio data recorded on the DAS array.

3 Project Milestones

IMS ADM Decatur Project
Responsibility Assignment Matrix (RAM)

	ADM	LBNL	Silixa	USGS	SCS	Richland	ISGS
Project Management	A	P	P	P	P	P	P
Design IMS for Decatur site	R	A	P	P	P		
Install DAS and Rotary Sources	A	I	R	P			
Develop IMS data processing solution	R	A		P			
Monitoring passive microseismicity	R	I		A			
Commission monitoring system	A	P		P			
Data collection and reservoir modeling	P	A		P			
Hydrogeologic Modeling	A			P	I		I
Community Outreach	P					A	P
Project Reporting	A	P	P	P	P	P	P

Legend	
Participant	P
Accountable	A
Review Required	R
Input Required	I
Sign-off Required	S

Figure 3. Matrix showing assigned responsibility for each team. LBNL is accountable for "Design IMS for Decatur site", "Develop IMS data processing solution", and "Data collection and reservoir modelling".

Table 1: Milestone log (FY-2016)

Milestone Description*	Fiscal Year 2016				Planned Start Date	Planned Completion Date	Actual Start Date	Actual End Date	Comment (notes, explanation of deviation from plan)
	Q1	Q2	Q3	Q4					
Phase I Project Prerequisites									
Task 1-2: Project Management and Planning & Project Fact Sheet	A								
Task 3: NEPA	B								
Phase II IMS Design									
Task 1 IMS Data Acquisition and Processing Equipment					10/1/2015	3/31/16			
Task 2 IMS DAS Surface Cable and Rotary Sources CASSM.	C				10/1/2015	3/31/16			AOP Tracked
Task 3 IMS Software Design and Development	D	F			10/1/2015	3/31/16			
Task 4 Passive Microseismicity Monitoring		E			10/1/2015	3/31/16			
Task 5 IMS Final Design Review			G		10/1/2015	9/30/16			
Task 6 IMS Equipment Procurement					10/1/2015	6/30/16			
Task 7 Construction and Environmental Permits					10/1/2015	6/30/16			
Phase III IMS Installation									
Task 1 Develop Construction Plan to Facilitate Executions of Task 2.0 – 4.0.					3/31/2016	9/30/16			
Task 2 IMS Data Acquisition and Processing Equipment Installation				I	6/30/2016	9/30/16			
Task 3 IMS DAS Surface Cable and Rotary Sources CASSM Installation			H	J	6/30/2016	9/30/16			AOP Tracked

Table 2: Milestone log (FY-2017)

Milestone Description*	Fiscal Year 2017				Planned Start Date	Planned Completion Date	Actual Start Date	Actual End Date	Comment (notes, explanation of deviation from plan)
	Q1	Q2	Q3	Q4					
Phase III IMS Installation									
Task 2 IMS Data Acquisition and Processing Equipment Installation	K				10/1/2016	12/30/16			
Task 3 IMS DAS Surface Cable and Rotary Sources CASSM Installation	L				10/1/2016	12/30/16			
Task 4 IMS Control, Monitoring and Data Acquisition, Software Installation		M			1/1/2017	1/30/17			
Phase IV IMS Commissioning and Operation									
Task 1-3 IMS Commissioning		N			1/31/2017	3/31/17			AOP Tracked
Task 4 IMS Operation				O	3/1/2017	9/30/17			AOP Tracked
									**Note: Milestone reporting accompanies quarterly report, one month after end of quarter.

Table 3: Milestone log (FY-2018)

Milestone Description*	Fiscal Year 2018				Planned Start Date	Planned Completion Date	Actual Start Date	Actual End Date	Comment (notes, explanation of deviation from plan)
	Q1	Q2	Q3	Q4					
Phase IV IMS Commissioning and Operation									
Task 4 IMS Operation – subtask 4.2				P	3/1/2017	10/31/18			AOP Tracked
Task 4 IMS Operation – subtask 4.3				Q	10/1/2017	10/31/18			AOP Tracked
									**Note: Milestone reporting accompanies quarterly report, one month after end of quarter.

Milestones list

Phase I Project Prerequisites

Milestone 1-1 (A) Phase I Task 1 & 2 AOP Tracked Milestone
Title: Project Management Planning and Project Fact Sheet
Planned Completion (Reporting) Date: Q1 12/31/15
Verification Method: Quarterly Progress report and supplement

Milestone 1-2 (B) Phase I Task 3
Title: NEPA
Planned Completion (Reporting) Date: Q1 12/31/15
Verification Method: Quarterly Progress report and supplement

Phase II Field Testing of Emerging Technologies

Milestone 2-2 (C) Phase II Task 2 AOP Tracked Milestone
Title: Report on installation plan for IMS Surface cable and rotary sources
Planned Completion (Reporting) Date: Q2 3/31/16
Verification Method: Quarterly Progress report and supplement

Milestone 2-1 (D) Phase II Task 3
Title: Provide a report that details the planned architecture for the IMS data acquisition system and processing flow, including functionality of significant processing nodes and interface structure
Planned Completion (Reporting) Date: Q2 12/31/15
Verification Method: Quarterly Progress report and supplement

Milestone 2-1 (E) Phase II Task 4
Title: Report on functionality of microseismic monitoring system and real-time event detection system

Planned Completion (Reporting) Date: Q2 3/31/16
Verification Method: Quarterly Progress report and supplement

Milestone 2-1 (F) Phase II Task 3
Title: Detail real-time DAS crosscorrelation and stacking algorithm and provide analysis of synthetic data evaluation with different levels of synthetic noise
Planned Completion (Reporting) Date: Q2 3/31/16
Verification Method: Quarterly Progress report and supplement

Milestone 2-2 (G) Phase II Task 5
Title: Report on system installation hazard review and hazard mitigation measures
Planned Completion (Reporting) Date: Q3 6/30/16
Verification Method: Quarterly Progress report and supplement

Phase III IMS Installation

Milestone 3-1 (H) Phase III Task 3 AOP Traced Milestone
Title: Report on final DAS surface cable and rotary source CASSM design
Planned Completion (Reporting) Date: Q3 6/30/16
Verification Method: Quarterly Progress report and supplement

Milestone 3-2 (I) Phase III Task 3
Title: As-built report on installed DAS infrastructure
Planned Completion (Reporting) Date: Q4 9/30/16
Verification Method: Quarterly Progress report and supplement

Milestone 3-2 (J) Phase III Task 2
Title: As-built report on IMS data acquisition and processing equipment
Planned Completion (Reporting) Date: Q4 9/30/16
Verification Method: Quarterly Progress report and supplement

Milestone 3-3 (K) Phase III Task 2
Title: Completion of IMS data acquisition and processing equipment installation
Planned Completion (Reporting) Date: Q1 12/31/16
Verification Method: Quarterly Progress report and supplement

Milestone 3-3 (L) Phase III Task 3
Title: IMS infrastructure installation complete
Planned Completion (Reporting) Date: Q1 12/31/16
Verification Method: Quarterly Progress report and supplement

Milestone 3-4 (M) Phase III Task 4
Title: IMS Control, Monitoring, and Data Acquisition, Software Installation complete
Planned Completion (Reporting) Date: Q2 1/31/17
Verification Method: Quarterly Progress report and supplement

Phase IV IMS Commissioning and Operation

Milestone 4-1 (N) Phase IV Tasks 1-3 AOP Traced Milestone
Title: Report on commissioning of IMS equipment and related controls
Planned Completion (Reporting) Date: Q2 3/31/17
Verification Method: Quarterly Progress report and supplement

Milestone 4-2 (O) Phase IV Task 4 AOP Traced Milestone
Title: Detailed report on data quality and processing during first two quarters of operation
Planned Completion (Reporting) Date: Q4 9/30/17
Verification Method: Quarterly Progress report and supplement

Milestone 4-3 (P) Phase IV Task 4 operation AOP Traced Milestone
Title: Final detailed report on data quality and processing, during entire operating period
Planned Completion (Reporting) Date: Q4 10/31/18
Verification Method: Quarterly Progress report and supplement

Milestone 4-4 (Q) Phase IV Task 4 operation AOP Traced Milestone
Title: Detailed report on comparison of real time IMS data with state-of-the-art detailed models, analyzing any mismatch
Planned Completion (Reporting) Date: Q4 10/31/18
Verification Method: Quarterly Progress report and supplement

4 Results and Discussion

4.1 IMS Conceptual Design and Planning

System Architecture

We have divided our architecture analysis into two sections. The first encapsulates the algorithmic steps of the IMS, a second separate section describes the physical data-flow and instrumentation interfaces. Within the algorithmic architecture, major components include the seismic analysis section, the joint flow inversion, P/T instrumentation, and microearthquake (MEQ) analysis/display.

As illustrated in Figure 4, the IMS general software architecture is comprised of three major parts which are (1) data input, (2) core processes (processing and analysis), and (3) output. The seismic input data streams are given by CASSM and MEQ. The non-seismic data component is, for brevity, referred to as flow data and includes downhole P/T, fluid saturations and fluid flow rates, and distributed temperature sensing. The historical database includes existing seismic reflectivity profiles and well logs and predates the beginning of the actual continuous monitoring data stream.

The IMS algorithm design features two main output functionalities. The first module includes analysis methods that address the detection of short-term reservoir state changes that may affect integrity, safety and permanence. A second module aims at continuously enhancing long-term prediction capabilities. The incoming data stream is pre-processed to be fed into an optimization framework that seeks to refine hydrogeological parameters of a reservoir flow model.

Near-real-time event detection

The first component of the IMS algorithm meets the demands of assessing storage performance and reservoir integrity in near-real time. To enable short-term decisions on the injection schedule, the seismic and flow-type monitoring data stream is analyzed for anomalous time-lapse variations that may indicate potentially critical reservoir condition changes. We designed the system for investigating various approaches for an automated detection of off-normal reservoir conditions:

- Difference-to-baseline above certain thresholds for P/T, saturation
- Rapid temporal and/or spatial P/T changes
- Rapid saturation changes

This real-time analysis module is also interacting with the reservoir flow model for the purpose of verification forward modeling. Forward modeling of state changes, such as

- large-scale unexpected plume movement,
- unexpected saturation variations,
- leakage into shallow units

aids in the identification of critical state changes. The reproduction of anomalous data events by such forward modeling will be a strong indicator for confirming or ruling out false alarms.

Further considered for the identification of critical state conditions are more advanced algorithms, such as for example pattern recognition algorithms.

Long term reservoir state forecasting

The second main functionality of the IMS software meets the demand of long-term predictions of reservoir storage capability and integrity. A joint inversion framework based on the inverse flow and transport modeling code iTOUGH2 is the centerpiece, with the inclusion of the DAS data simulator into the hydrological parameter optimization algorithm pending. Joint inversions of the available flow and seismic data will be performed periodically in order to update and refine the reservoir model. This model reflects the current hydrogeological state in the reservoir environment.

The inclusion of CASSM data into the reservoir model updating procedure can be done in various ways where we consider two approaches, distinguished by a different degree of coupling to the hydrogeological flow modeling. The approach with the stronger coupling involves the finite-difference modeling of time-lapse gathers in order to directly compute an objective function between the measured and simulated time-lapse gathers. For this purpose, we included the seismic forward modeling component into the joint inversion method. The joint inversion approach that involves a looser coupling between the seismic and flow data involves using the CO2 saturation maps derived from the CASSM analysis as (additional) proxy hydrological data input.

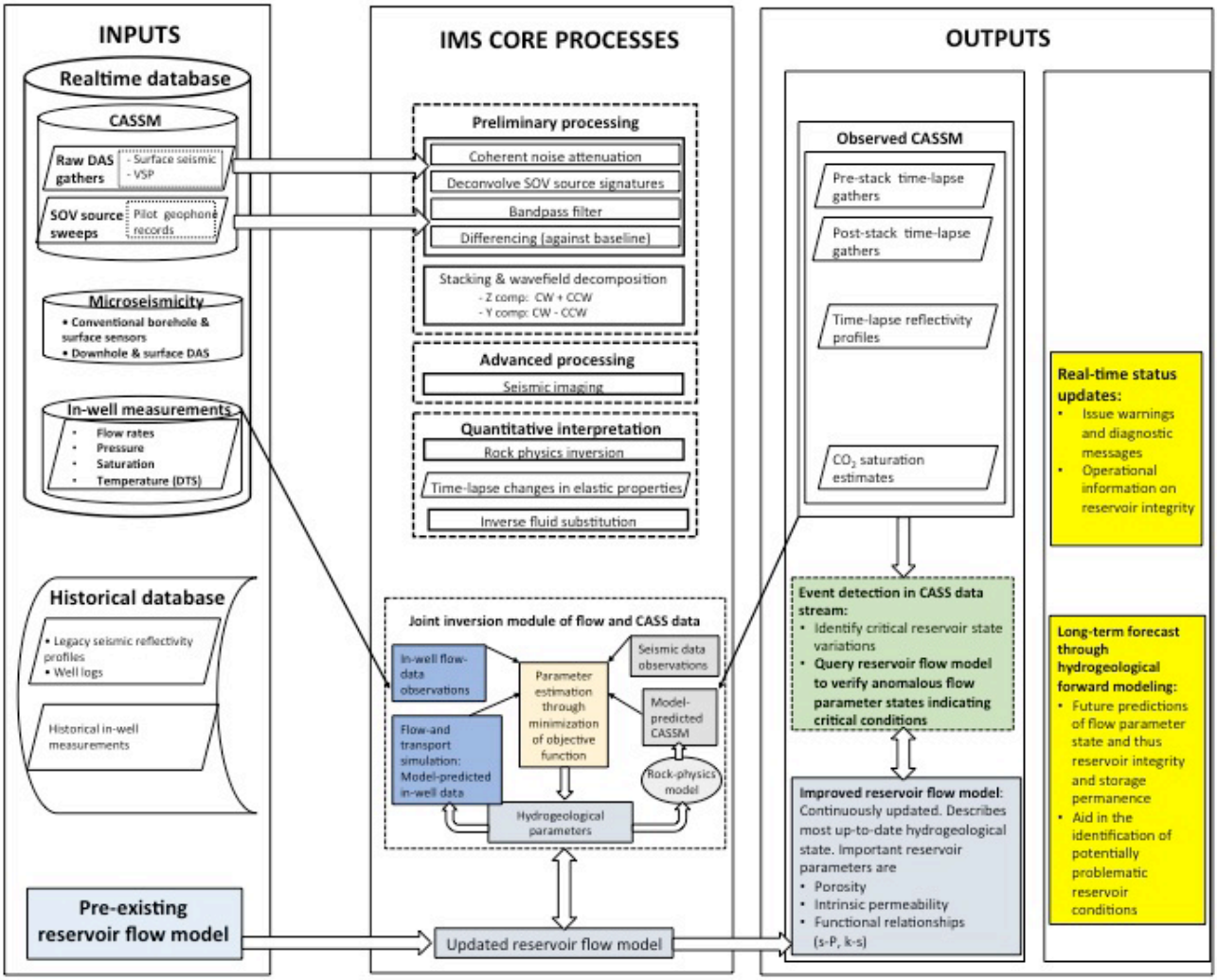

Figure 4. Processing nodes interface structure.

DAS Surface Cables and SOV sources

In order to decide on the optimal monitoring equipment to be deployed, the Otway Project Site and Aquistore have been the primary testing locations for the components that were selected for inclusion into the ADM IMS system (Daley et al., 2014; Harris et al., 2017; Pevzner et al., 2017). Several different fiber types and constructions were evaluated at the Aquistore Site in November 2015 and at the Otway Site in February, 2016. Figure 5 shows two different cables collocated in a trench at the Aquistore site. The upper cable is a helically wound cable (HWC) with an outer diameter of 25 mm and the lower cable is a tactical fiber-optic cable with a diameter of approximately 6.25 mm. Seismic data collected at the Otway Site using an SOV shows that the HWC is more sensitive to reflected P-wave energy than the straight tactical cable. Figure 6 shows common shot gathers from the Otway Site comparing the HWC to straight fiber using VSP data.

Figure 5. Two co-located fiber-optic cables from the Aquistore site, showing the helical wound cable (top) and straight tactical cable (bottom).

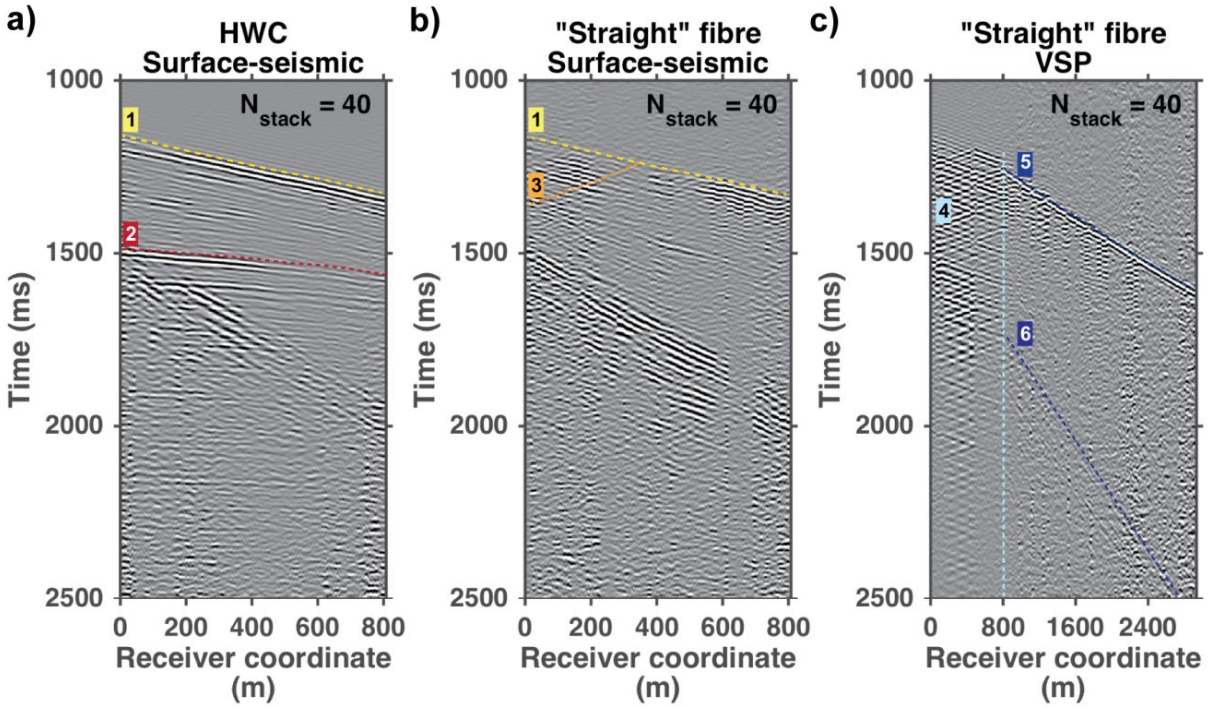

Figure 6. Permanent seismic monitoring data consisting of 1) surface seismic data (common shot gather) recorded with helically wound cable (HWC) (a) and "straight" fiber (b), and 2) VSP data recorded with "straight" fiber (c). The red arrows in (a) point at reflection arrivals impinging near perpendicular to the cable. The origin of the time axes is earlier than the beginning of the sweep time. 1, P refraction; 2, reflection; 3, surface reflection of P refraction; 4, borehole reverberation; 5, primary downgoing P-wave; 6, tube wave.

Based on lessons learned from the Aquistore and Otway Projects we installed HWC at the ADM site, and we also modified the design of the SOV foundations. The original steel rebar cage and

threaded mounted rods installed at the Otway Site eventually failed due to the inability of the threaded rods to resist the shear forces generated by the SOVs. To resist the shear forces beneath the surface steel mounting plate, structural steel I-beams were added along with a lower plate. The threaded rods now only need to act to resist tension, while the I-beams resist shear. The new rebar cage with I-beam cage is seen in Figure 7.

Figure 7. Rebar cage with I-beam reinforced mounting plates. Each rebar cage has a mount for both a small 4 T-f SOV and a 10 T-f SOV (Otway Project).

4.2 IMS Software Design and Development

Acquisition geometry and spatial sampling

Figure 8 shows the layout of the CASSM system. The routing of NW and NE DAS lines and locations of the SOVs is detailed in the figure. The monitoring array at the ADM field site includes two surface transects as well as borehole DAS arrays; in this report we focus our analysis of the southeast-northwest branch of the "L-shaped" layout. Figure 9a depicts the SE/NW array superimposed on approximate outlines of the CO2 plumes at different times after the initiation of injection. As shown in Figure 9a, three surface orbital vibrators (SOV1, SOV2, and SOV3) were modeled at distances that are 100 m, 600 m, and 950 m away from the injection well CCS2. Two downhole DAS arrays were also modeled for VSP acquisition in CCS2 and VW2, reaching maximum depths of 1919 m and 1493 m, respectively. A buried surface DAS array with an approximate burial depth of 10 m below the surface runs from CCS2 to VW2, covering an offset range of 791 m. Figure 9b depicts the predicted reflection fold (CMP) at locations along the plume profile assuming a DAS channel spacing of 1m, a proxy for coverage and potential S/N improvement. Significantly, with just the three SOVs the modeling shows we can achieve CMP fold of at least 100 in the area that is within 850-meter radius away from CCS2. Seismic sampling in the 50-meter vicinity of the injection well CCS2 is particularly good (with fold count as high as 750).

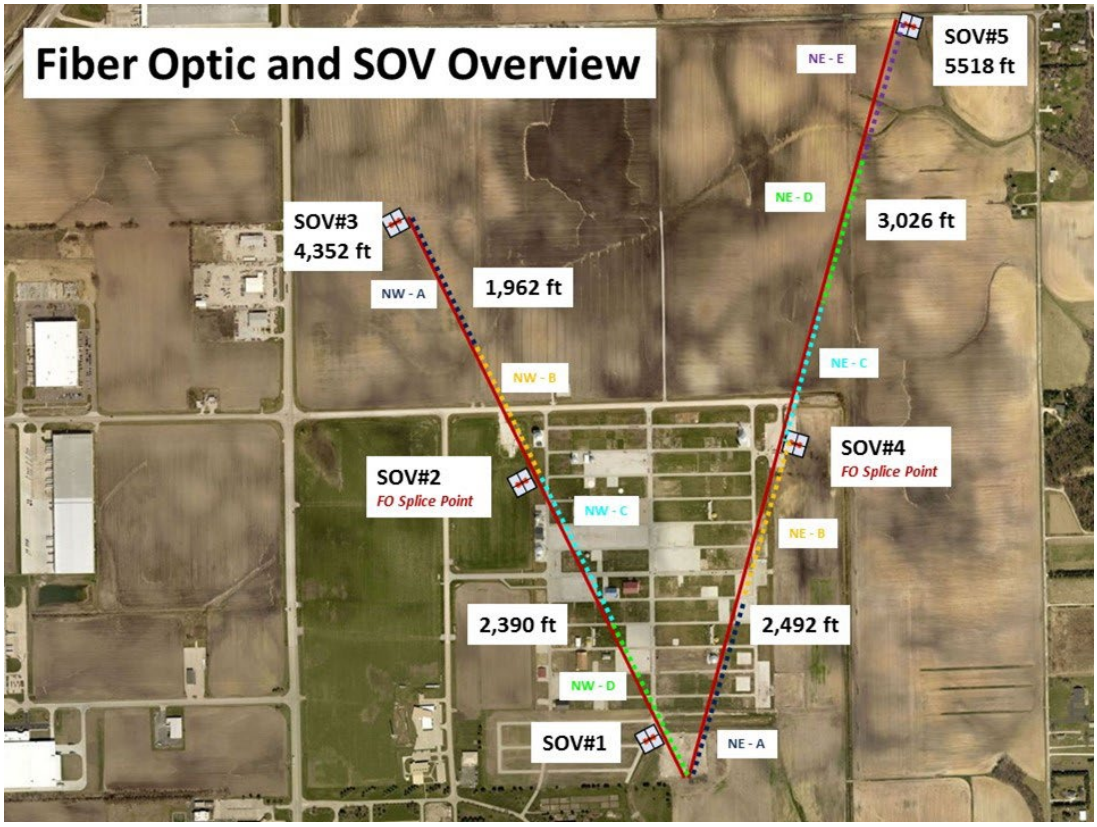

Figure 8. Layout of the CASSM system's showing the location of DAS cables and SOVs.

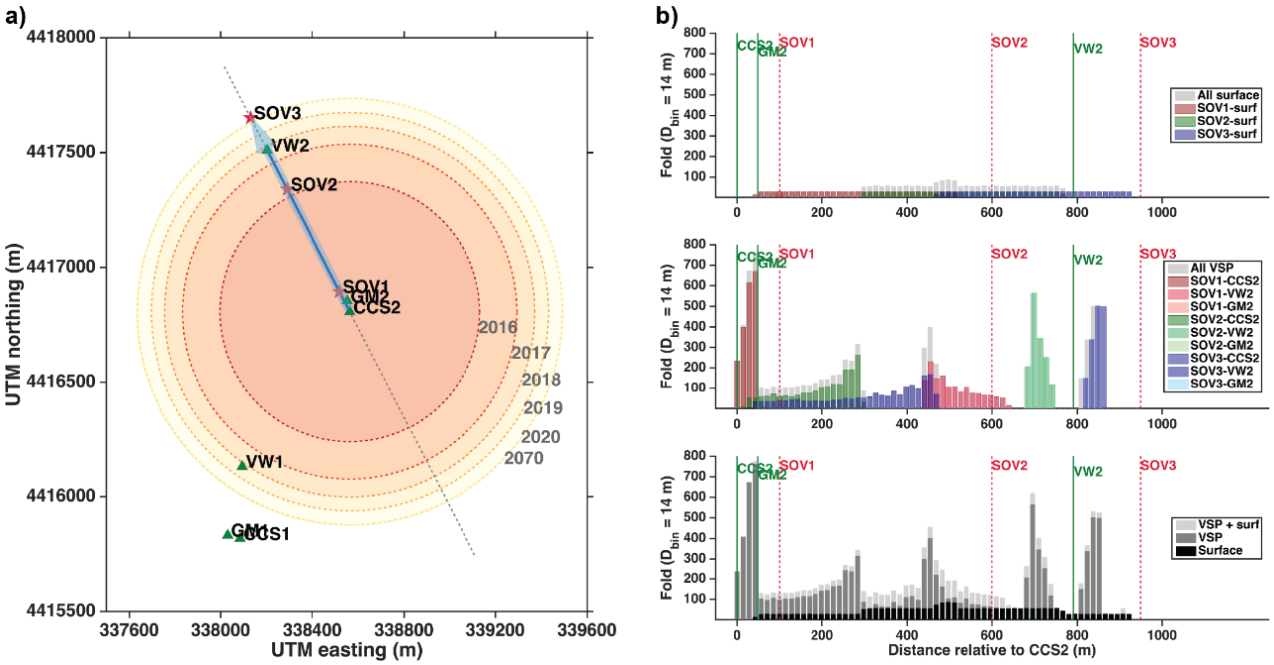

Figure 9. Spatial sampling of the survey layout. (a) Acquisition geometry, and (b) fold distribution along the southeast-northwest seismic transect (highlighted by the arrow in (a)). SOV = surface orbital vibrator; Dbin = diameter of the common midpoint (CMP) bins used in fold counting. Circles in (a) denote surface projections of the simplified plume fronts for the time span from 2016 to 2070 (color-coded in chronological order). Reflection interface of the fold map is the base of the CO2 injection zone at CCS2.

Conceptual CO_2 plume evolution sequence

To gain a fundamental understanding of the seismic response likely induced by the presence and evolution of the CO2 plume, we avoid using sophisticated plume geometry that could hinder seismic interpretation. Instead, we use a simplified model consisting of bounded ellipsoidal volumes of sequentially increasing size to represent the plume front (Figure 10). The CO2 saturation is the highest at the injection center (95%) and tapers toward the edge of the plume. The detectable CO2 front is defined at a saturation level of 15%. The plume center is located at the center of the CCS2 perforation zone (2068 m below the ground surface), and the plume is terminated at the bottom by a low-permeability mudstone baffle (2091 m below the ground surface). We modeled six vintages for the years of 2016, 2017, 2018, 2019, 2020, and 2070. The cross-sectional radius of the plume increases from 567 m (CY 2016) up to 932 m (CY 2070), and the maximum height of the plume increase from 71m (CY 2016) to 103 m (CY 2070). Throughout the plume evolution sequence, we only consider radial expansion of the plume. Vertical movement of CO2 (buoyancy-driven) is not considered in this test.

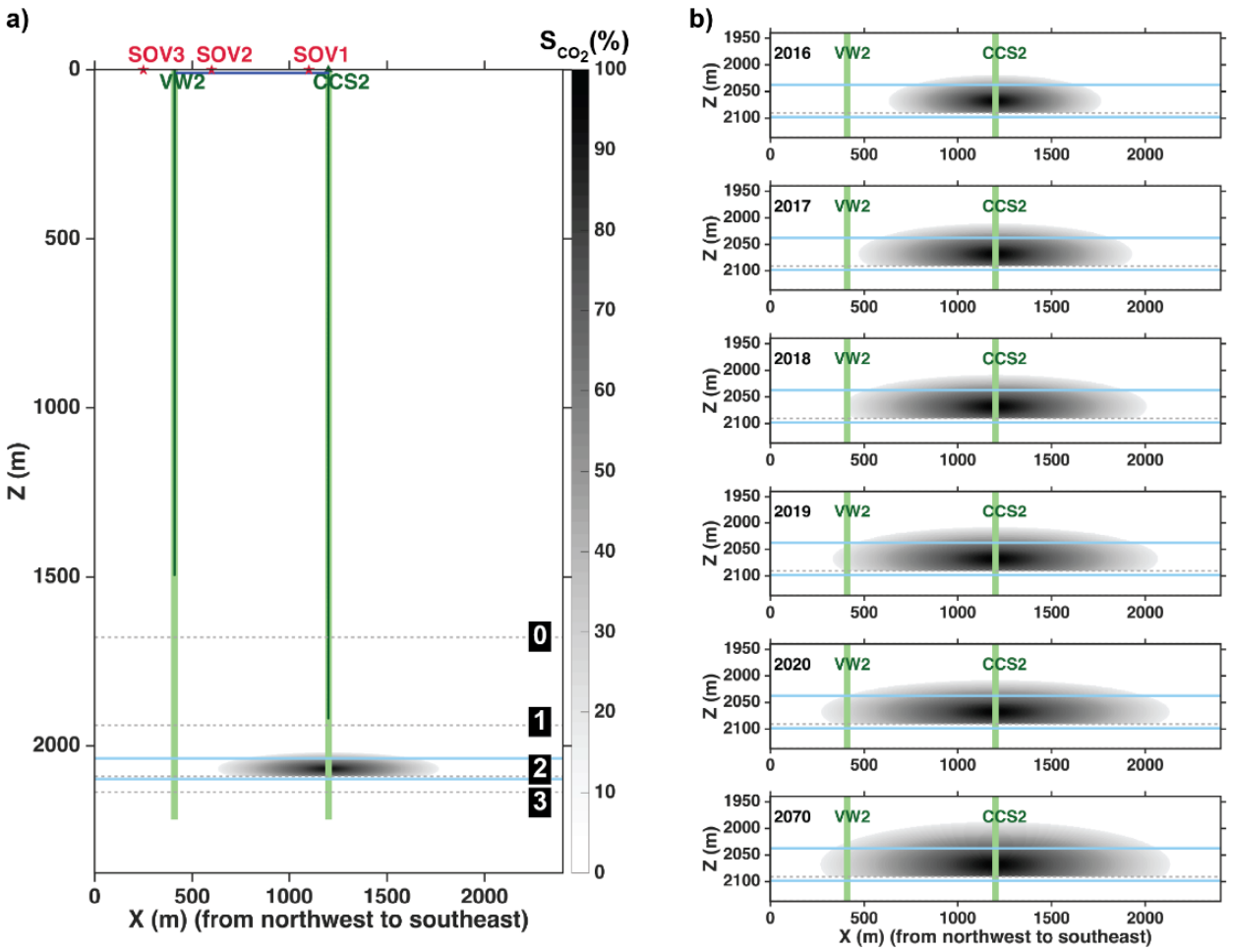

Figure 10. Conceptual CO2 plume model and evolution history. (a) Full-scale profile of the CO2 distribution in CY2016, and (b) zoom-in view of the plume profile evolving in the time span OF CY2016–CY2070. Dash lines 0, 1, 2, and 3 denote the major interfaces within the Mt. Simon saline reservoir. 0 = top of Mt. Simon formation; 1 = interface separating middle and lower Mt. Simon intervals; 2 = top of the mudstone baffle near the base of Mt. Simon; 3 = base of Mt. Simon. In between the two horizontal blue lines is the perforation zone for CO2 injection in CCS2. Light green lines denote the full depth extent of the well CCS2 and VW2. Dark green lines denote the downhole DAS arrays.

2D viscoelastic model construction

Prediction of seismic response to variations in CO2 saturation requires creation of appropriate maps of seismic properties, using a rock physics forward model, as well as an approach to generate the background seismic properties prior to CO2 injection. In this study, we use a simple blocked model based on existing CCS2 well log data to provide background properties and utilize a combination of Gassmann fluid substitution & the Reuss effective fluid model for predicting the effects of CO2 saturation.

The baseline model is assumed to have only 1D property variations and is based upon the extensive set of well logs collected before the completion of CCS2, shown above in Figure 11. A log-blocking strategy is applied to produce a simplified model that includes only a limited number of impedance contrasts located within the target interval, mainly (1) the interface separating middle and lower Mt. Simon intervals, (2) the top of the mudstone baffle near the base of the lower Mt. Simon interval, and (3) the interface separating lower Mt. Simon and pre-Mt. Simon intervals (Figure 11). The blocking strategy leaves the overburden unchanged (0–102 m) and preserves the two-way travel-time of the reflections associated with the above-mentioned impedance contrasts. This simplification allows easier observation of changes due to CO2 injection without the separation of multiples related to propagation through the overburden.

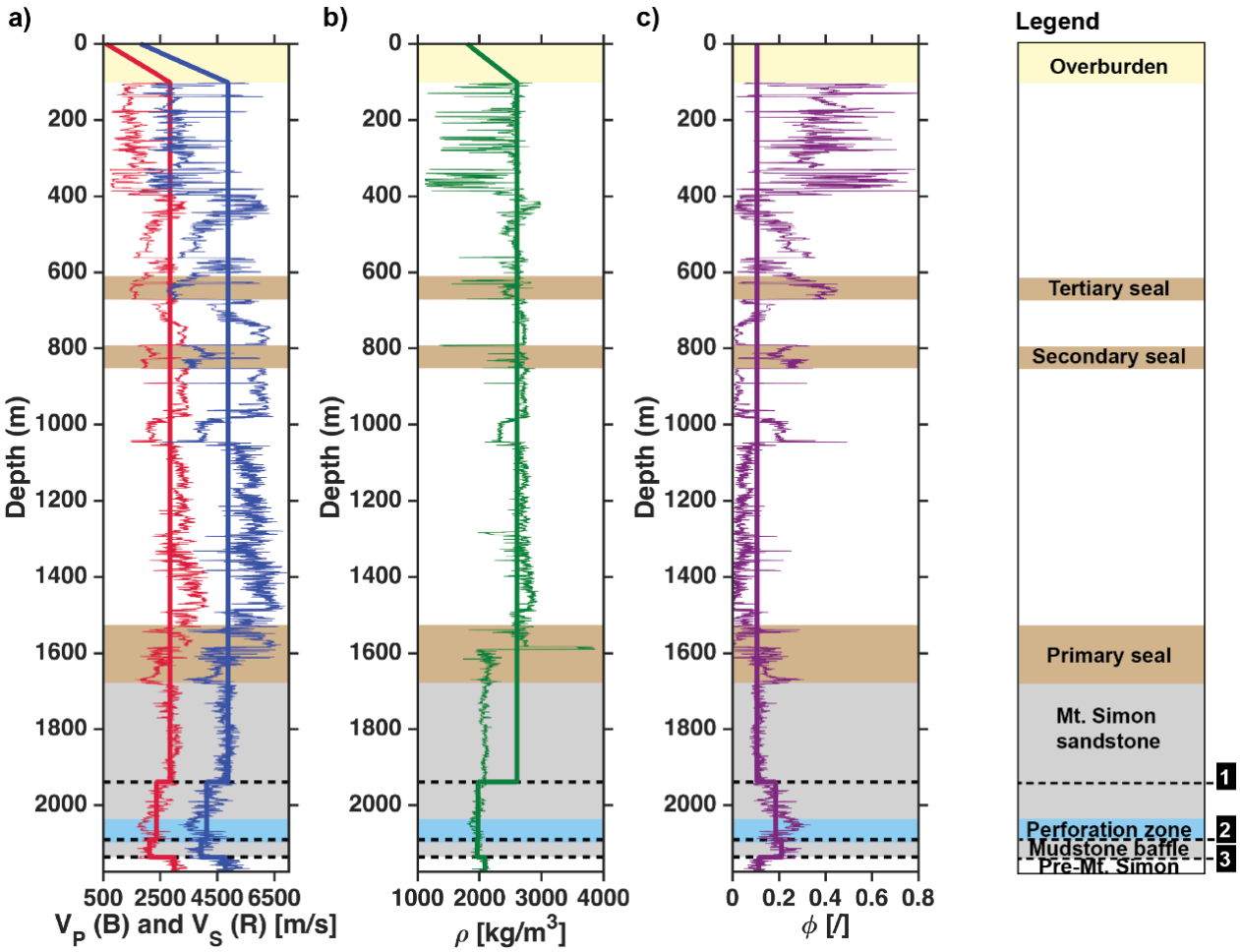

Figure 11. 1D baseline model based upon CCS2 well log data. (a) P- (blue) and S-wave (red) velocities, (b) density, and (c) porosity. Colored thin lines denote the well log data. Colored thick lines denote the 1D baseline model constructed with a well-log blocking strategy. Dash lines 1, 2, and 3 denote the three reflection interfaces in the target zone: 1 = interface between the middle and lower Mt. Simon intervals; 2 = top of the mudstone baffle near the base of Mt. Simon; 3 = base of Mt. Simon.

Rock physics forward model & plume velocity structure

To generate the seismic properties of the plume model, we apply a three-step fluid substitution scheme: First, the bulk properties of the pore-filling fluid mixture of CO2 and brine are modeled with Wood's relation (e.g. a Reuss effective fluid model). Second, the dry-frame properties of the reservoir are derived from the brine-saturated baseline model (provided by sonic logs shown in Figure 11a) by using the inverse Gassmann equation. Finally, the fluid properties of the brine-CO2 mixture and dry-frame properties of the Mt. Simon sandstone are plugged into Gassmann equation to obtain P-wave velocity and density of the plume region. Figure 12b shows the P-wave velocity reduction (relative to baseline values) caused by the injected CO2 for all six time-lapse vintages that are being investigated in this test. The P-wave velocity reduction within the plume is in the range of 6%–8%. Due to the fact that the Reuss/Wood fluid model is a harmonic mean, the seismic response due to CO2 injection largely occurs when scCO2 first invades a region and there is only a weak sensitivity to intermediate saturations.

$$\Delta V_P(\%) = \frac{V_P^{monitor} - V_P^{baseline}}{V_P^{baseline}} \times 100\%$$

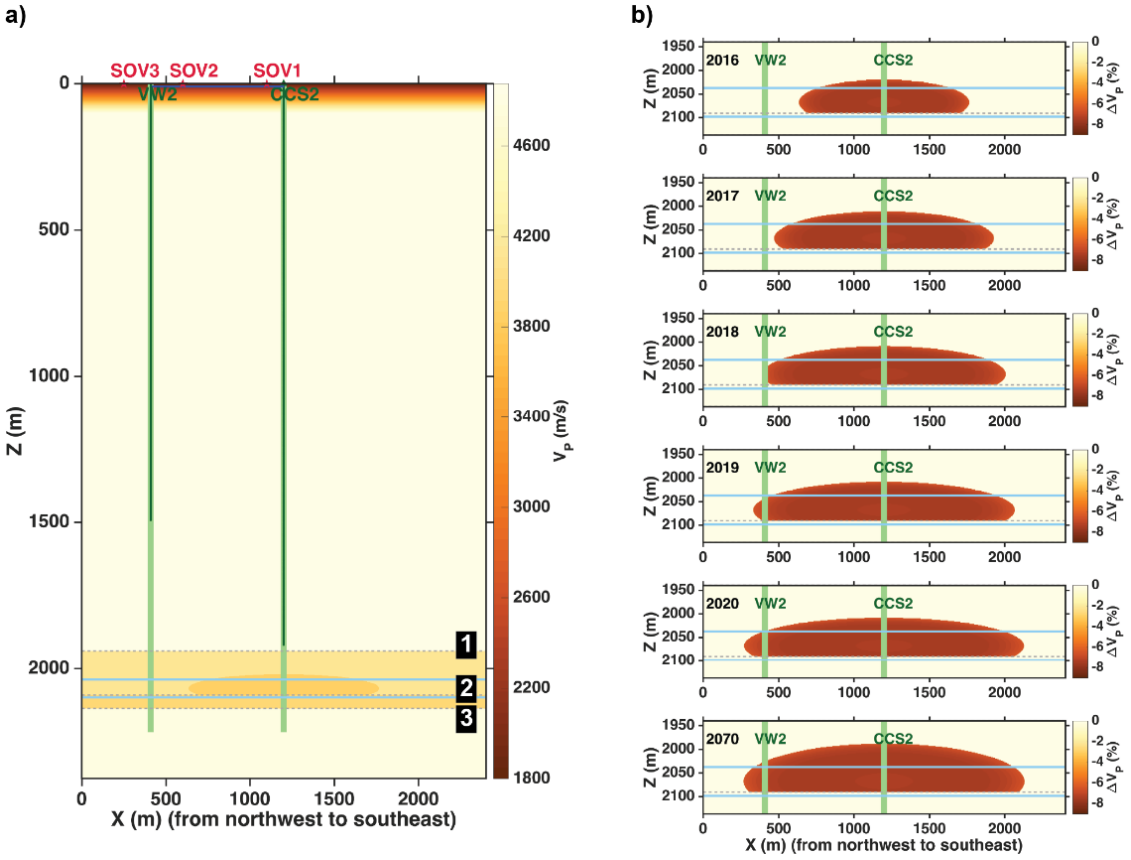

Figure 12. Seismic profile of the VP model. (a) Full-scale profile of the VP model for the year of 2016, and (b) zoom-in view of the seismic profile evolving in the time span of CY2016–CY2070. Dash lines 1, 2, and 3 denote the three reflection interfaces in the target zone: 1 = interface separating middle and lower Mt. Simon intervals; 2 = top of the mudstone baffle near the base of Mt. Simon; 3 = base of Mt. Simon.

Seismic forward modeling of the time-lapse responses

With a time-lapse model of changes in seismic properties calculated, we then use the forward solver of DENISE (Köhn et al. 2012), a 2D time-domain isotropic (visco)elastic finite-difference modeling and full waveform inversion (FWI) code, to generate synthetic data corresponding the field source-receiver geometries as illustrated in Figure 8. Note that to enable efficient calculation, the receiver spacing of the modeled DAS array is increased to 2 m.

Existing studies usually employ fully elastic models and completely ignore the influences of seismic attenuation. However, such modeling tends to overestimate signal intensities, particularly for free-surface and inter-bed multiples. To simulate more realistic overburden conditions and to effectively attenuate multiples, we conduct viscoelastic modeling using nominal seismic Q values for lithology types present in the model ($Q_{overburden}$ = 10; $Q_{mudstone}$ = 50; $Q_{sandstone}$ = 100; $Q_{granite}$ = 200). The input parameters for our modeling runs are listed in Table 4. The computation time for the entire northeast-southwest transect was ~4 minutes on the Cray XC30 Edison at NERSC (http://www.nersc.gov/users/computational-systems/edison/) using 361 CPUs.

Table 4: Key parameters of the finite-difference modeling.

Parameters	Values
Order of the finite-difference operators	12th order in space; 2nd order in time
Grid size	1.5 m
Model dimension (horizontal, vertical)	2764.5 m, 2992.5 m (1843 grids, 1995 grids)
Time step size	0.13 ms
Wave propagation time	2.5 s
Input source wavelet	Bandlimited spike wavelet (20–80 Hz)
Output wavefield	Horizontal- and vertical-component particle velocities (Vx and Vz)
Boundary conditions	Free surface on the top, 10-grid perfectly matched layer (PML) on the sides
Modeled receiver spacing	2 m
Number of receivers	Surface DAS: 395 Downhole DAS in CCS2: 960 Downhole DAS in VW2: 747
Number of SOVs	3

Examples of the synthetic data

In this section we include some examples designed to highlight attributes of the synthetic datasets, particularly reflection arrivals from the reservoir unit. Figure 13 and 14 show examples of synthetic gathers simulated for surface and VSP geometries with SOV1 as the source. Figure 13a and 14a are travel-time predictions of the primary reflections within the target interval consisting of pure (PP and SS) and converted seismic modes (PS and SP). Within each mode window (marked by colored patches), we predicted four sets of travel-time curves for four interfaces (ordered from the

shallowest to the deepest): (1) the interface separating middle and lower Mt. Simon intervals; (2) the maximum height of the CO2 plume; (3) the mudstone baffle surface that terminates the bottom of the plume; (4) the interface separating Mt. Simon and pre-Mt. Simon intervals. For the four groups of corresponding events in the synthetic gathers, reflections occurring at interface 1 (the earliest arrivals shown in Figure 13a and 14a) is not affected by the plume and thus serve as reference modes for contrasting time-lapse changes occurring in the rest of the three reflection groups.

Next, we analyze the characteristics of the time-lapse signals. Time-lapse signals usually manifest themselves as both amplitude changes and time shifts of the primary reflections. Because velocity reductions caused by the plume are small (less than 8%), direct comparisons between baseline and monitor gathers only reveal subtle differences such as the slight "pull-down" of the SP mode immediately below the SP window in Figure 13c, and the faint up-going phases in Figure 14c that have curved moveout due to changes in incident and exit angles of the ray paths resulting from the convex plume front. Because strong phase alterations are absent, we anticipate time shift to play a relatively minor role among the usable time-lapse signals. Amplitude changes, on the other hand, appear to be the prominent indicators of the CO2 distributions.

We then examine the intensity of the time-lapse signals. After taking differences between the baseline and the monitor survey, we can see that time-lapse signals have intensity that is smaller than but comparable to the amplitude of the primary reflections occurring within the target interval (Figure 13d and 14d).

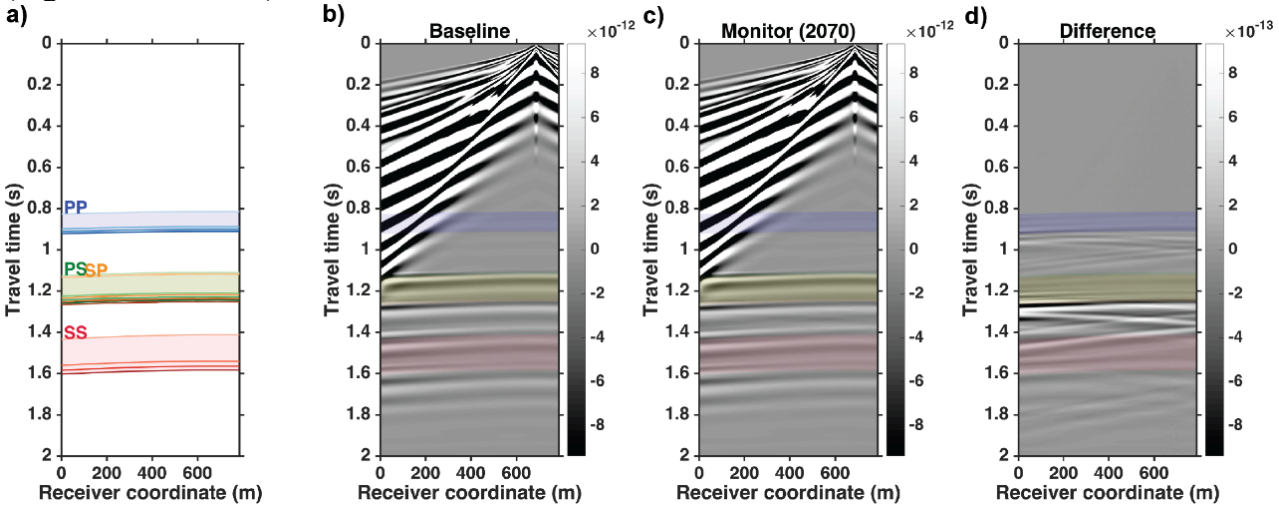

Figure 13. Synthetic examples of surface DAS records generated by SOV1. (a) Predicted travel time curves of primary reflections, (b) synthetic baseline gather, (c) synthetic monitor gather for CY2070, and (d) time-lapse difference between monitor and baseline gathers. (b) and (c) are clipped at 0.1 standard deviation relative to mean amplitude of the baseline gather. Clipping level in (d) is set at 10% of the clipping level in (b) and (c). A time-dependent gain factor of t2 (t = traveltime) is applied to (b), (c), and (d) for geometric divergence correction.

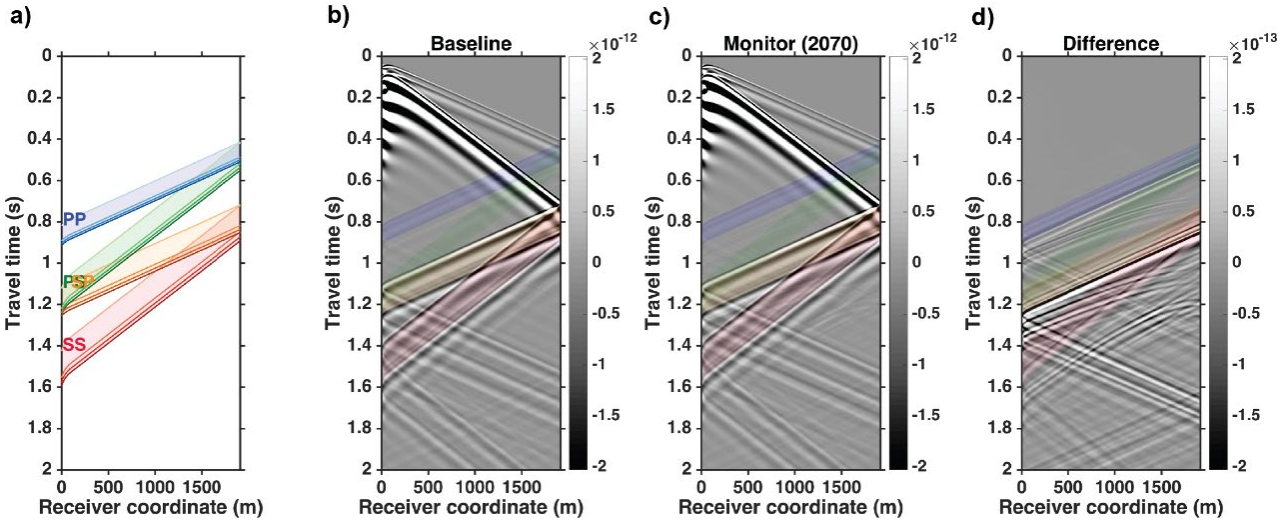

Figure 14. Synthetic examples of downhole DAS records (CCS2) generated by SOV1. (a) Predicted travel time curves of primary reflections, (b) synthetic baseline gather, (c) synthetic monitor gather for CY2070, and (d) time-lapse difference between monitor and baseline gathers. (b) and (c) are clipped at 0.1 standard deviation relative to mean amplitude of the baseline gather. Clipping level in (d) is set at 10% of the clipping level in (b) and (c). A time-dependent gain factor of t2 (t = traveltime) is applied to (b), (c), and (d) for geometric divergence correction.

Other noticeable characteristics of the time-lapse changes are the strongest time-lapse signal is the amplitude change of the reflection that occurs at the above-mentioned interface 3, the mudstone baffle surface that terminates the bottom of the CO2 plume. The sequence of closely spaced time-lapse signals neighboring the interface-3 reflections are related to the plume itself. These signals can be classified into two types. The first type shows straight moveout parallel to the moveout of the interface-3 reflections and the amplitudes show nearly few variations with offset. The second type has curved moveout and exhibits amplitude variations with offset (AVO). The straight-line arrivals are likely related to inter-bed multiples between interface 1 and 3, whose time difference is magnified when their ray paths traversing through the low-velocity plume. The curved signals likely result from reverberations within the plume itself, during which their incident and exit angles are altered by the convex plume front. Time-lapse signals of the converted SP mode have the strongest intensity, both for the surface and VSP geometries.

Detectability, interpretability, and repeatability requirements

In the following sections, we conduct quantitative analyses on synthetic gathers of single vintage and multi-year vintage sequence. In doing so, we aim to address the detectability and interpretability of the simulated time-lapse signals, as well as the required repeatability for the CASSM system. The analyses are based upon two metrics: (1) the normalized root-mean-squared (NRMS) amplitude difference between the baseline and monitor data, and (2) the time shift caused by the presence of the supercritical CO2. We seek answers to the following questions:

- Detectability: How large are the changes between the baseline and monitor data?

- Interpretability: Are the distribution of the time-lapse changes correlated with the saturation distributions of the supercritical CO2? Can the vintage sequence of the time-lapse changes reveal the evolution and migration of the CO2 plume?
- Repeatability: How repeatable does the CASSM system need to be in order to reliably record time-lapse signals? As NRMS also is frequently used as a repeatability metric, the NRMS distributions obtained in our test can help determine the threshold level of CASSM repeatability.

Single vintage example

We first assess the detectability of the time-lapse signal. Figure 15 shows a single-vintage example for the modeled CO2 distribution in CY2016. The distributions of NRMS and time shift computed for pure PP phase (Figure 15a) illustrate the most promising source-receiver combinations from which we can see pronounced changes. For the VSP geometry, downhole DAS array in the injection well CCS2 consistently show the strongest time-lapse signals, with maximum NRMS ranging from 80% to 90% and maximum time shift up to 4 ms. For the surface DAS array, SOV1, the source that is the closest to the injection well CCS2, is able to produce strong time-lapse signals that occupy more than 1/3 of the achievable CMP extent, with maximum NRMS of 75% and maximum time shift of 2.5 ms.

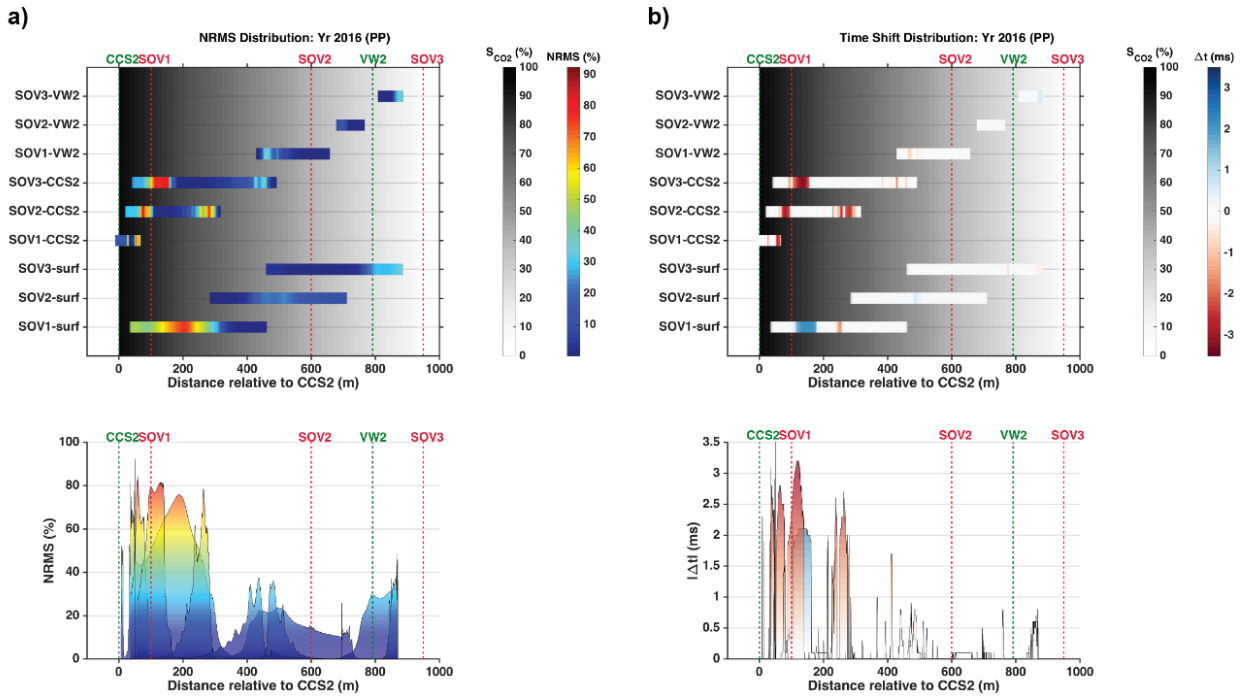

Figure 15. Time-lapse metrics of a single vintage (CY2016) for pure phase PP. (a) Normalized rms amplitude difference (NRMS) between the baseline and monitor surveys, and (b) the corresponding time shift.

Next, we focus on the interpretability of the time-lapse signals. Although the time-lapse signals show intensity distributions that are affected both by acquisition geometries and by variations in CO2 saturation, the locals at which high- and low-intensity signals are present correlate well with variations of the CO2 saturation and local thicknesses of the plume sampled by the ray paths. As expected, high-intensity clusters mostly concentrate in the vicinity of the injection well CCS2 (where highest CO2 saturation and plume thickness are present).

Lastly, we examine the modeled NRMS from the perspective of CASSM repeatability. The repeatability (Kragh and Christie, 2002) is calculated as

$$\mathbf{NRMS} = \mathbf{200}\ \frac{\mathbf{RMS(b-m)}}{\mathbf{RMS(b)+RMS(m)}}\ .$$

We use a NRMS range of 10% to 30%, typically considered "good" NRMS values in the seismic monitoring literature (Johnston 2013), as a criterion for assessing time-lapse feasibility.

In Figure 15a, we can see that within a 300-meter radius around the injection well CCS2, the high-intensity time-lapse signals yield NRMS values in the range of 50% to 90%, which are substantially higher than the repeatability thresholds. For the portion of CMP that falls outside of the 300-meter radius, despite that <10% "gaps" are present at offsets of ~300 m and ~700 m relative to CCS2, the rest of the NRMS values generally vary in the range of 20% to 50%. These NRMS values, though overlapping with the above-mentioned threshold range, remains higher than the 10% NRMS lower limit. With carefully designed CASSM system, the majority of the time-lapse signals should be detectable.

Vintage sequence example

Figure 16 shows wavefield examples of time-lapse difference for the vintage sequence CY2016–CY2070. Comparing later vintages (CY2017–CY2070) against the very first vintage (CY2016), both the moveout alteration and time separation of the inter-bed and in-plume multiples become more and more pronounced. Reflections bouncing off the impedance contrast at the top of the plume show slight advancing, indicating upward growth of plume front. From these direct observations, it is clear that the evolution of the time-lapse signals reflects the expansion of the plume.

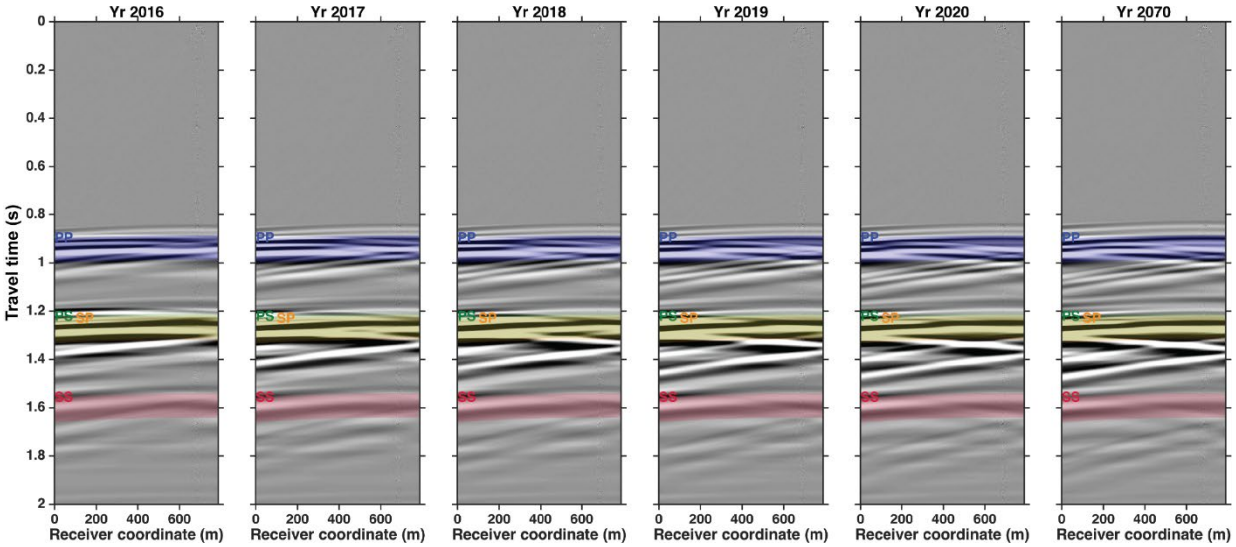

Figure 16. Examples of time-lapse signals for vintage sequence CY2016–CY2070 (source = SOV1; receiver = surface DAS array). Color-shaded patches denote the 0.1-second time window used for computing NRMS and time shift.

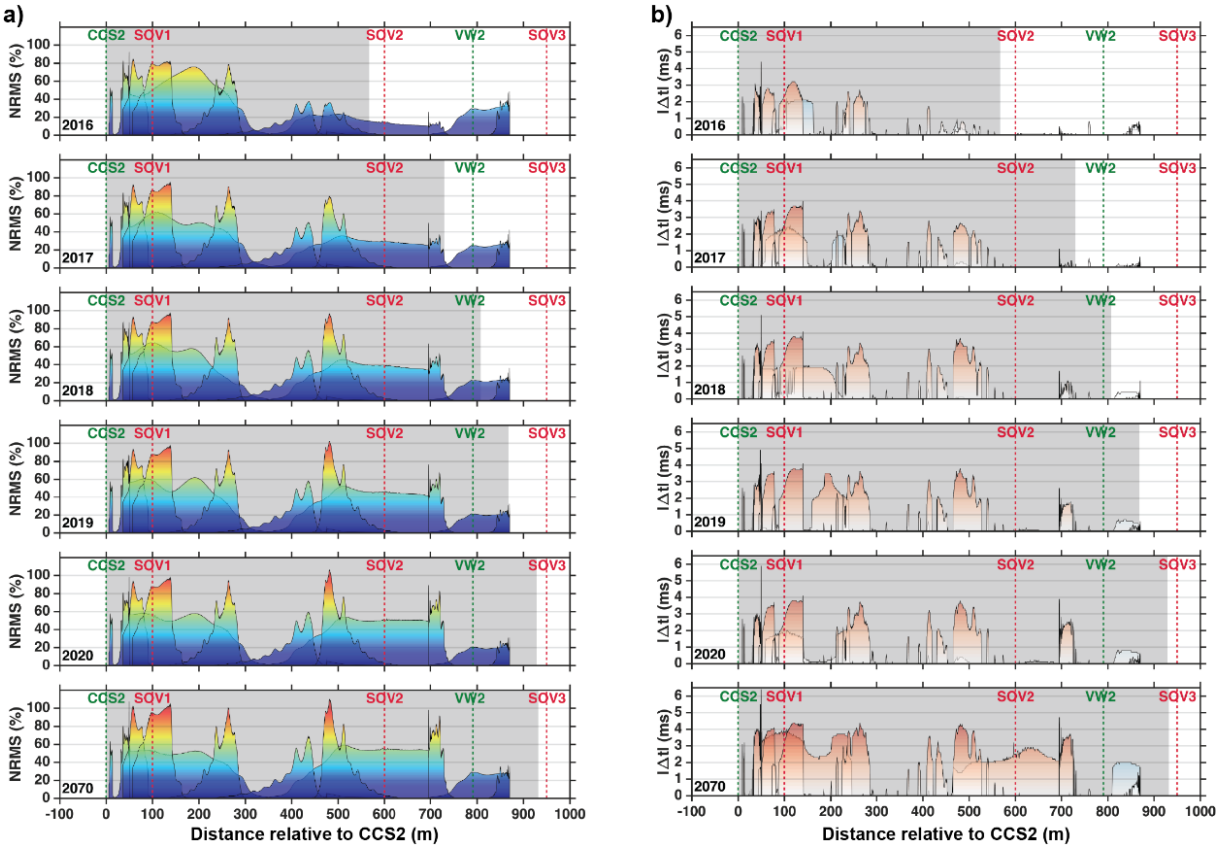

Figure 17. Time-lapse metrics of vintage sequence CY2016–CY2070 for pure phase PP. All the source and receiver combinations are collectively displayed (overlain on top of each other). (a) NRMS, and (b) time shift. The gray background denotes the lateral extent of the CO2 plume (i.e., the semi-major axis length of the elliptical plume).

Figure 18 shows the evolution of NRMS and time shift for the same vintage sequence. For both metrics, the locations of the dominant peaks do not change. For NRMS, although the relative amplitudes of these peaks vary as the plume expands, the spatial positions of these peaks do not change. For time shift values, while the dominant peaks maintain a consistent spatial distribution, a few peaks also noticeably emerge and/or disappear. Such time shift changes are likely related to the moveout and travel time changes of the inter-bed and in-plume multiples. The fixed time shift peaks are likely related to the primary reflections occurring within the target interval. The stability of the NRMS and time shift peaks shown in Figure 9 indicate that changes in primary reflections constitute the most pronounced portion of the time-lapse signals.

In addition, the evolution of the time-lapse metrics is also consistent with the small aspect ratio of the plume. That is, the overall thickness of the plume is small (vary between 71 m and 103 m) whereas the lateral extent of the plume is large (vary between 567 m and 932 m). This is illustrated by the larger vintage-to-vintage changes occurring outside the 300-meter radius around CCS2 (e.g., the maximum NRMS value increases from 30% to 110%; the maximum time shift from 1 ms to 5 ms) and the smaller changes occurring within the 300-meter radius (e.g., the maximum NRMS value increase from 95% to 110%; the maximum time shift increase from 4.5 to 6.5 ms).

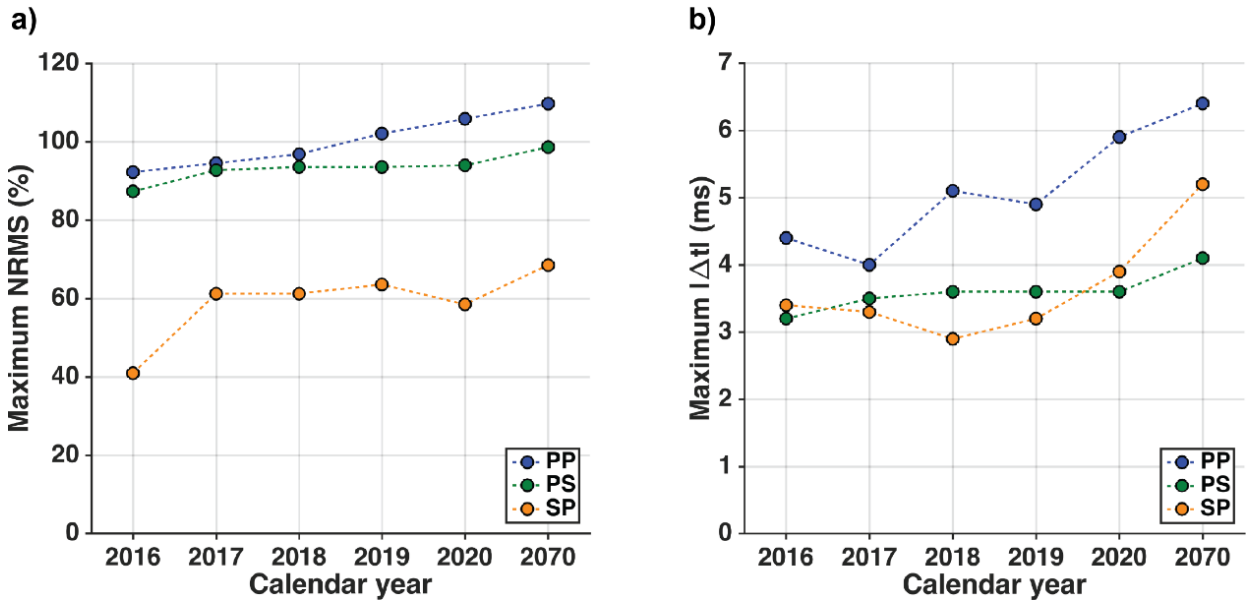

Figure 18. Vintage-to-vintage variations of (a) maximum NRMS and (b) maximum time shift.

Figure 18 summaries the maximum NRMS and time shift for pure phase PP and converted phases PS and SP across the vintage sequence. Intuitively, one would anticipate all the metrics to increase monotonically as plume expands over time. Figure 18 shows that although they all show general trends of increasing with time, most metrics (except for NRMS values of PP phases) show various degrees of fluctuations deviating from the anticipated monotonic trends. This likely results from phase distortions associated with the inter-bed and in-plume multiples.

Although pure phase PP is most-commonly used in reflection seismic, it is worth noting that all three phase groups show comparable maximum time shift and maximum NRMS values that are

above the 10%–30% repeatability thresholds described earlier. This indicates promising utility of converted modes for the ADM CCS monitoring program.

The effects of incoherent noise

The tests presented previously are for noise-free cases. In practice, seismic records are always contaminated by both coherent noise correlated in space and/or time, and incoherent noise. Coherent noise often plays a critical role in deciding processing flow and is more challenging to attenuate, but it tends to be survey-specific and thus difficult to simulate via synthetic tests. For this reason, we presently only focus on examining the effects of incoherent noise.

Simple mean stack is effective at attenuating incoherent noise, and the improvements in signal-to-noise ratio (SNR) is known to be proportional to $\sqrt{N}$, where N is the number of stacks. However, we do not yet know whether the same factor of $\sqrt{N}$ also applies to SNR improvements of time-lapse signals. Given that the amplitudes of the time-lapse signals are significantly weaker than those of the primary reflections (e.g., as shown in Figure 13 and 14), we seek answers to the following questions:

- How do the SNR improvements of the time-lapse signals scale with stack count N?
- The weaker time-lapse signals may require more stacks to reach preferred SNR. How does the number of stacks required for time-lapse surveys compare to the number of stacks required for stand-alone surveys?

We contaminate the clean synthetic gathers with additive white Gaussian noise (AWGN). The amplitude of AWGN is set to be comparable to the maximum amplitude of the time-lapse signals. The goal is to completely overwhelm the difference wavefield (monitor – baseline) with AWGN, and then observe the amount stacks that is required to make the time-lapse signals reemerge and subsequently reach desirable SNR. Figure 19a shows that after 200 stacks, the monitor data shown in Figure 19a appear nearly noise-free, as shown by the lack of "graininess" in the background and the crispy look of all the primary reflections. In contrast, Figure 19b shows that for the post-stack difference wavefield, the background "graininess" remains visible as due to the low amplitude of the time-lapse signals. Nevertheless, the time-lapse signals are clearly observable for PP, PS and SP phases.

Next, we examine the relationship between $\sqrt{N}$ and SNR both for primary reflections and time-lapse signals. Figure 20a shows that for primary reflections, the improvements in SNR scales linearly with $\sqrt{N}$ (as expected), and with 200 stacks, the SNR rapidly increase from 24 to ~270 (a 11-fold improvement). In comparison, the time-lapse signals show deviation from the linear scaling between SNR and $\sqrt{N}$. With slower rate of improvements, the SNR of the time-lapse signals only increase from 1 to 3 (a 3-fold improvement). From this test, we conclude that compared to a stand-alone seismic survey, 3–4 times more stacks are likely needed for retrieving high-SNR time-lapse signals.

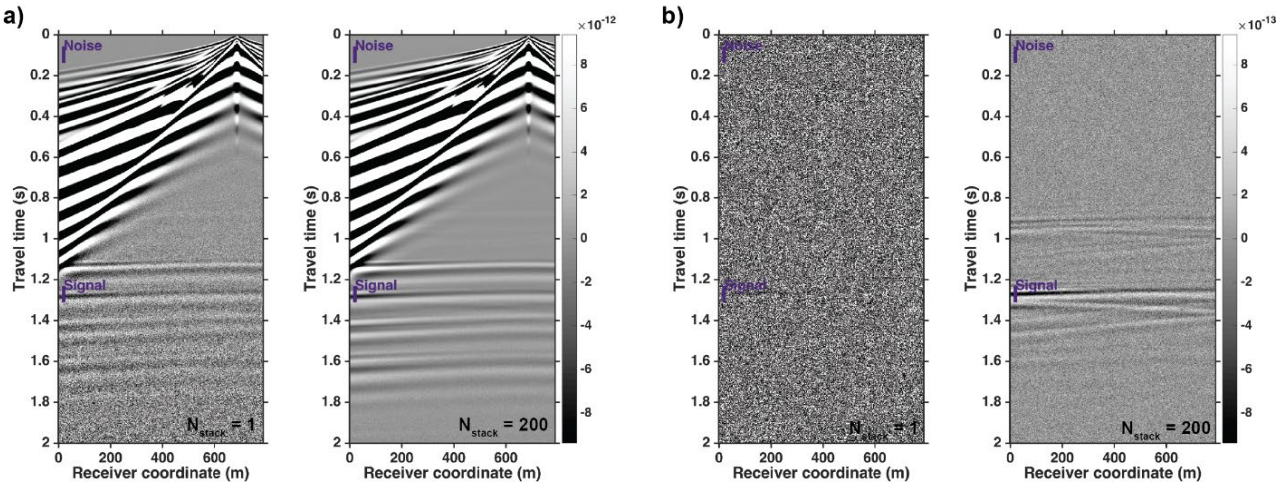

Figure 19. Synthetic shot gather examples (source = SOV1; receiver = surface DAS array) illustrating the effects of additive white Gaussian noise (AWGN). (a) Single stack (left) and 200-stack (right) of noise-contaminated monitor data, and (b) single stack (left) and 200-stack (right) of noise-contaminated time-lapse data. Level of AWGN is comparable to the maximum amplitude of the noise-free time-lapse signals. Purple bars denote signal and noise windows used for computing SNR.

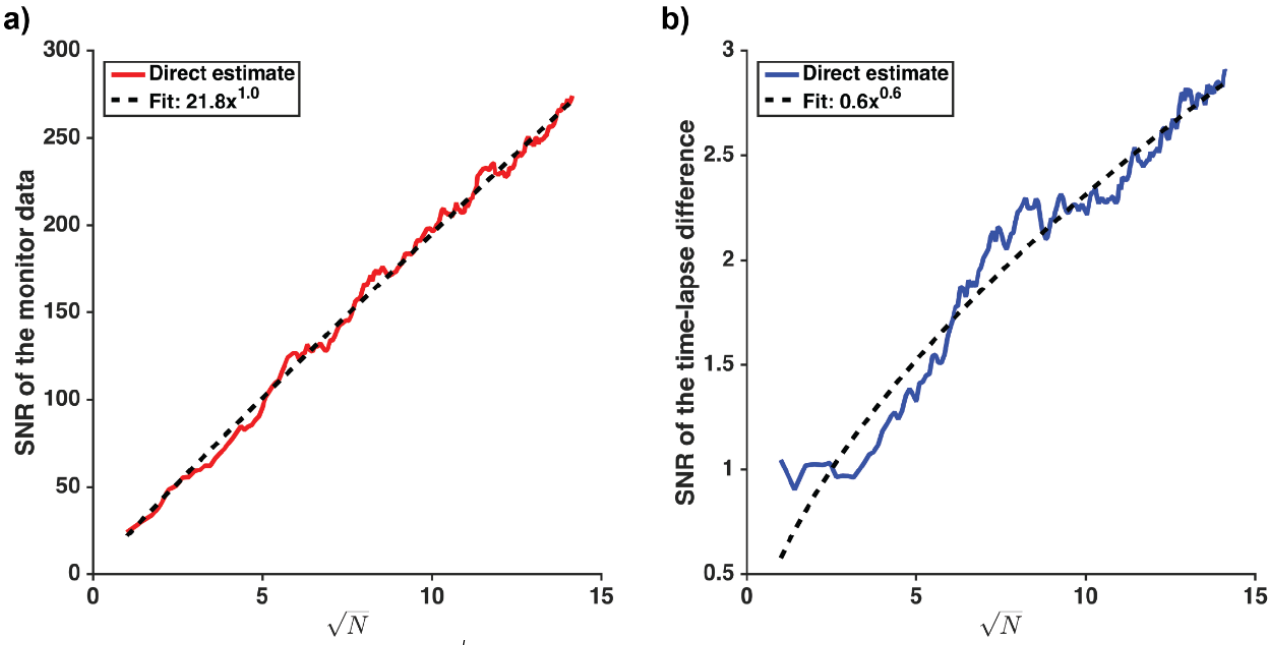

Figure 20. SNR as function of √N (N is the stack count). (a) For monitor data shown in Figure 11a, and (b) for time-lapse data shown in Figure 11b.

4.3 IMS Installation and Commissioning

Installation of IMS data acquisition and processing equipment

The IMS data acquisition system consists of three main components: (1) the SOV seismic sources, (2) the fiber-optic DAS monitoring network, and (3) the DAS interrogators and computer systems. Chapter 5.2 presented the layout for the HDD installed DAS cables and the SOV array. Figure 21 shows the two iDAS interrogators (Silixa LTD, Elstree UK) mounted on vibration isolation tables and the IMS monitoring rack that interfaces with downhole equipment in the CCS#2 monitoring well. On the right is shown the Ethernet router which connects via fiber-optic lines to the SOV network and a central control PC.

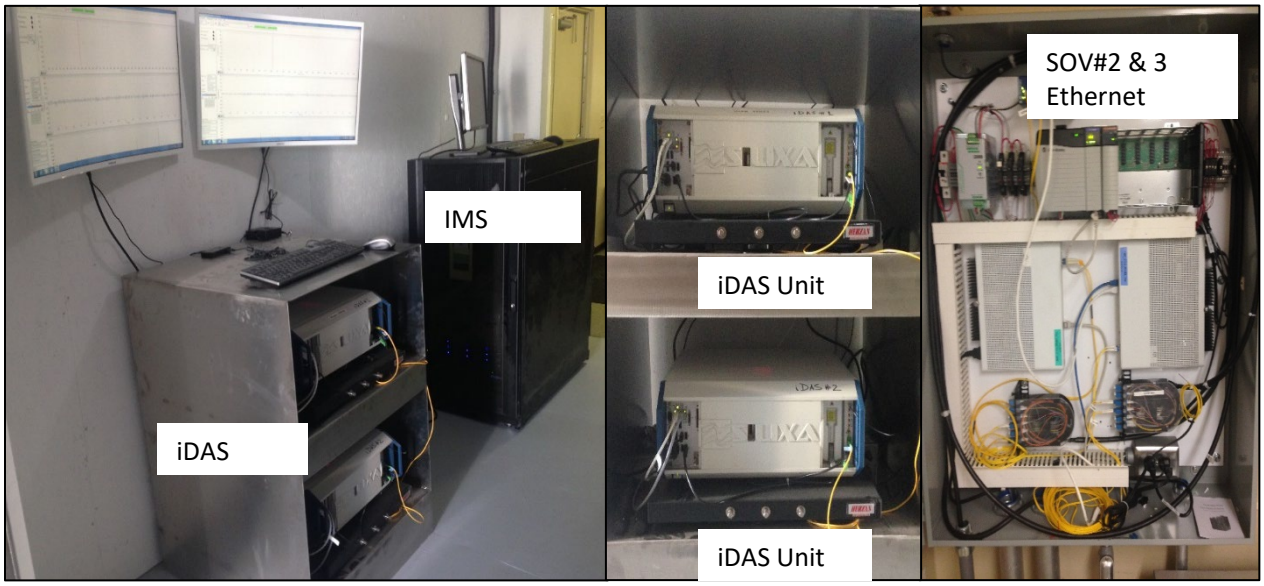

Figure 21. Setup of the IMS Server & iDAS units in the CCS#2 building and SOV#2. On the right, Ethernet switch inside the VW#2 building.

Installation of IMS DAS surface cable

The IMS DAS surface cable was installed at roughly a depth of 8 m using HDD drilling. Figure 22 shows the HDD rig, which allowed for a trenchless installation. After drilling for a length of 300 to 400 m, the HDD bit was directed up to the surface, and a pulling attachment replaced the drill bit. The helical DAS cable and a grout line were subsequently installed and a cement/fly ash grout used to fill the boring. Figure 23 and 24 shows the DAS cable and grout line being pulled into the HDD boring. The path of the DAS cable was mapped using a handheld detector (Figure 25) that records a signal emitted from a sonde mounted behind the drill bit. The later placement of the DAS cable can be located within +/- 30 cm and vertical location to within +/- 60 cm. The grout mix was prepared at an off-site cement batch plant and pumped using a standard industrial grout pump (Figure 26).

Figure 22. Horizontal directional drilling preparing to install the helical cable.

Figure 23. Cable and Conduit pull back.

Figure 24. Cable reels feeding DAS cable and grouting conduit into bore hole.

Figure 25. Location and depth monitoring.

Figure 26. Grouting DAS cable.

Installation of rotary sources CASSM

Five 10 ton-force SOV rotary sources were installed with two each along the NE and SW DAS lines, and the fifth SOV at the intersection of the two lines (Figure 8). A six-foot deep excavation was dug at each location and a steel foundation reinforcement and rebar cage was installed (Figure 28). The total length and width of each concrete pad was also 6ft, giving a total mass of approximately 20 tons to counteract the SOV forces. Beneath each SOV at a depth of 10 feet below grade was installed a 3-C geophone which recorded the SOV source term. On top of each concrete pad and steel reinforcement the SOV motor was bolted (Figure 29). An electrical control panel was set within 30 ft of the SOV motor, and attached to 460 VAC 3-phase power and a fiber-optic ethernet connection. The control electronics for the SOV consists of a 15 HP variable frequency drive, an embedded PC, 24-bit seismic digitizer and GPS time clock. A central PC server would schedule the SOV sweep tasks, and send commands to the SOV embedded PCs with instructions on when and how to sweep. After each sweep the GPS time-stamped geophone data was transmitted back to the central PC for further processing.

Figure 27. Foundation excavation.

Figure 28. Structural SOV anchor assembly.

Figure 29. Installed SOV motor and electronic panel.

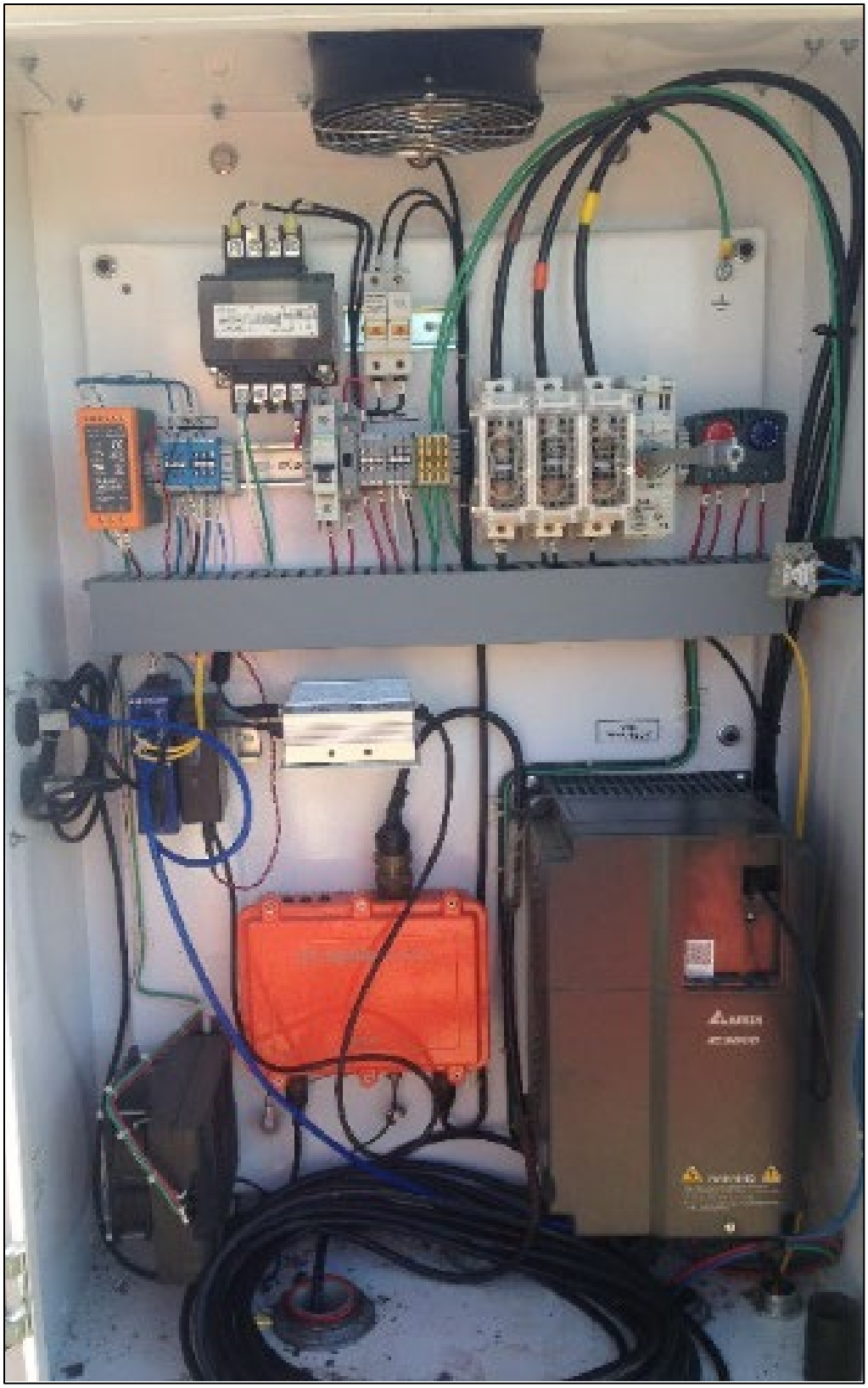

Figure 30. Electronic panel installation.

4.4 IMS Operations

Preliminary seismic data analyses

Figure 31 and 32 are single-sweep examples of DAS data acquired using the surface array and SOV4. Both examples show good signal-to-noise ratio for DAS channels that are located less than 350 meters away from the SOVs; within this offset range, the energy distribution of DAS recordings spans the broad range of 10–80 Hz. As can be seen from the raw data gather, refracted P-waves are visible in addition to surface wave arrivals.

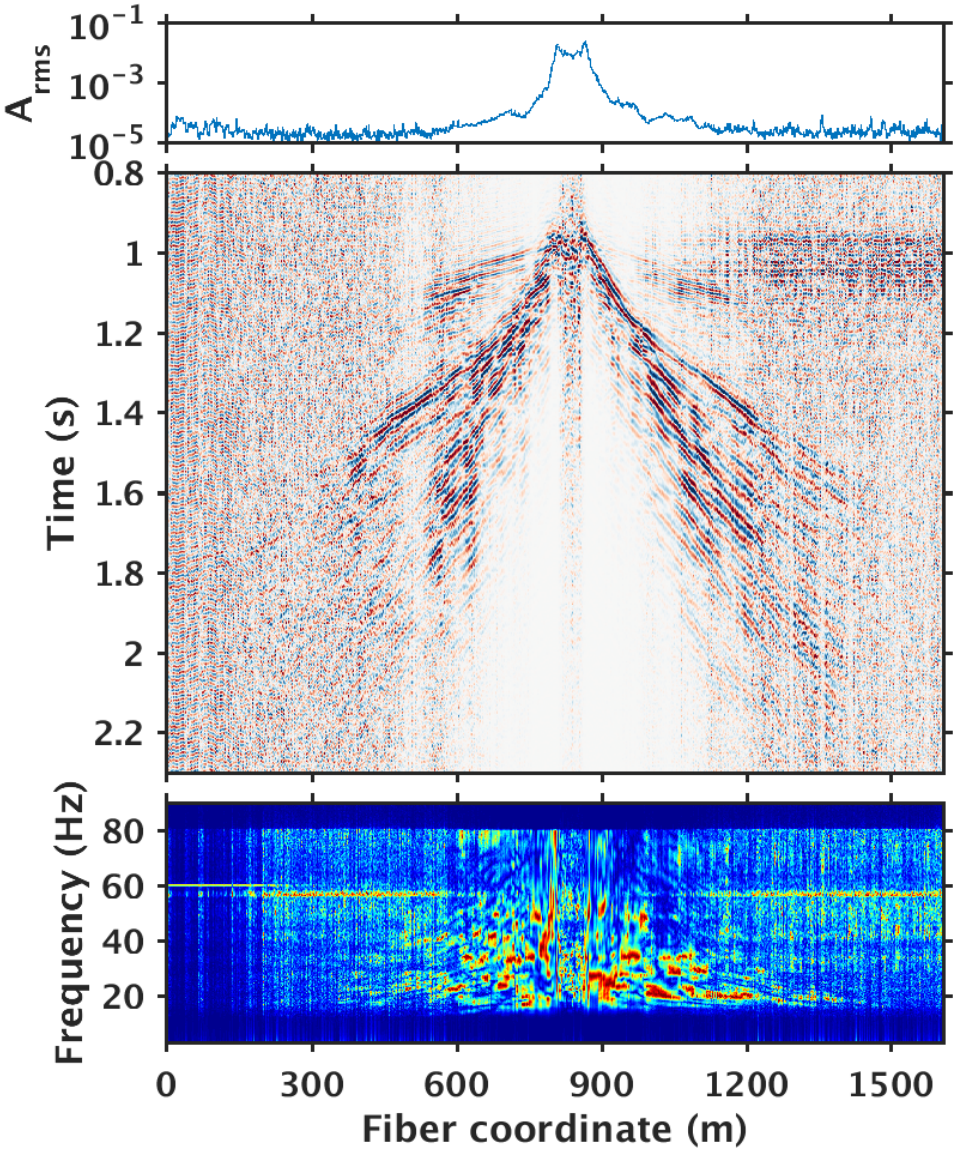

Figure 31. Example of SOV4 sweep recorded by the northeast DAS surface array.

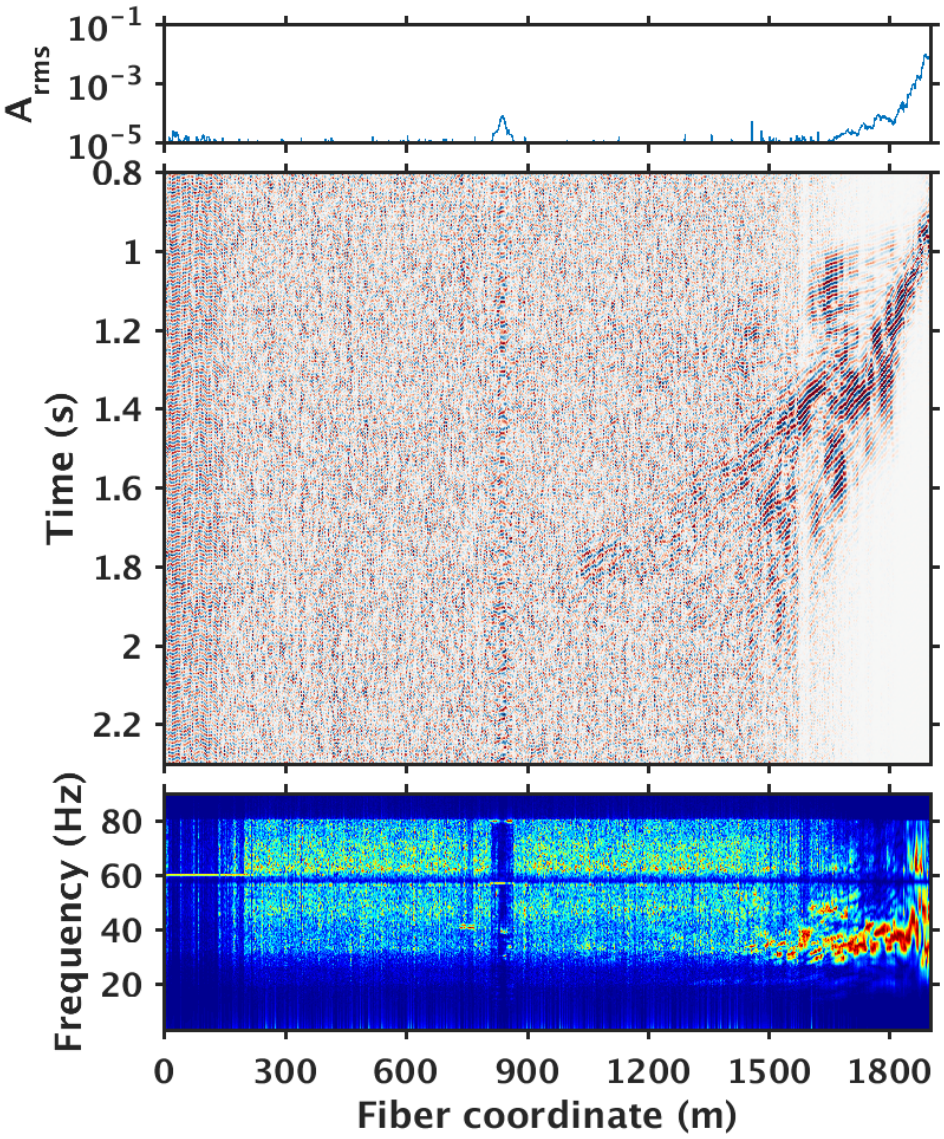

Figure 32. Example of SOV5 sweep recorded by the northeast DAS surface array.

Big Data engineering challenges

With the DAS interrogator systems (2 Silixa iDAS units) generating close to 2 TB/day of data from the fiber-optic arrays, our IMS system is confronting big data engineering challenges rarely seen in traditional monitoring projects. While the substantial data flow does present a challenge, we are in the unique position of developing an IMS system with sufficient on-site bandwidth, processing performance, and storage to accommodate these data rates. Along the course of acquisition, we faced issues regarding the bandwidth of the internet connection at the field site and data transfer for analysis. To improve Q/C capabilities, we explored data compression schemes to assist in transfer and storage constraints. However, the internet connection, which was through the ADM's on-site network, presented a challenge for data transfer and analysis as there was high

latency experienced by data processors at LBNL. The latency significantly affected the progress of the data processing.

For data management, Python tools for automatic data archiving have been set up to group raw DAS data files into two categories: (1) data files associated with SOV sweeps; (2) data files corresponding to ambient noise and microseismicity. Such archiving structure allows triaged data transfer at a time when direct data streaming between the ADM site and LBNL was not yet established.

Ghost event and its impact

Surface DAS arrays for the ADM project are buried at ~6m below the surface via horizontal directional drilling (HDD). This deep installation is helpful in minimizing the influences of near-surface variations, but it also introduced "receiver ghosts" events into the acquired seismic gathers.

Figure 33 is a simplified illustration of the ghost event. When receivers are buried a few meters below the surface, they receive not only primary reflections and refractions, but also "ghost reflections" that are downward reflections from the ground surface. The inference of the upward primary wave fields and the downward ghost reflections creates notches in the spectrum, thus limiting the usable bandwidth.

For the ADM surface seismic data, Figure 34 shows ghost notches both on source-monitoring geophones and near-source DAS channels. Because broadband seismic records are the sum of their harmonic constituents, the residual frequencies become more pronounced and thus lead to ringing effects in seismic gathers (e.g., Figure 35). This leads to difficulties in correctly identifying primary reflections, and such coherent events cannot simply be suppressed via vertical stacking.

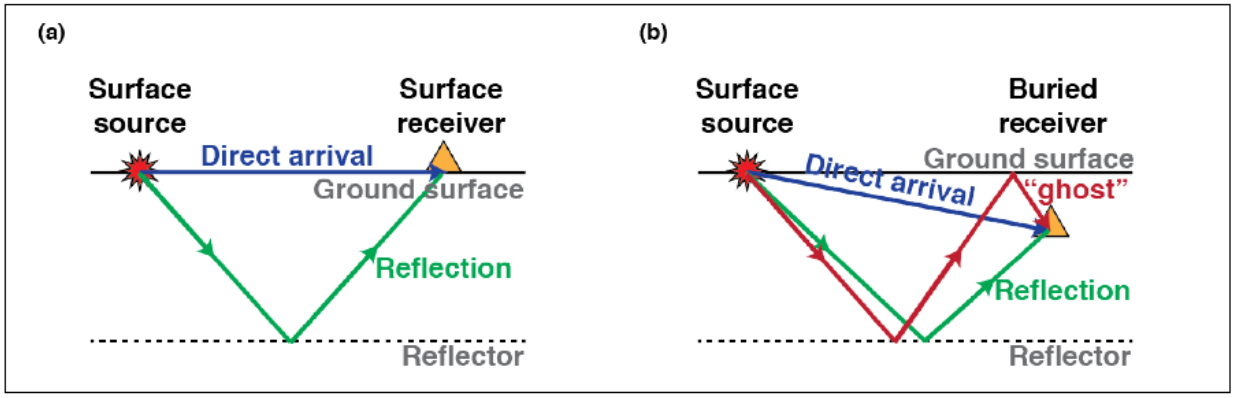

Figure 33. Simplified illustration of receiver ghost events: (a) Examples of major ray paths for surface source-surface receiver configuration; (b) ray path of a ghost reflection for a buried receiver.

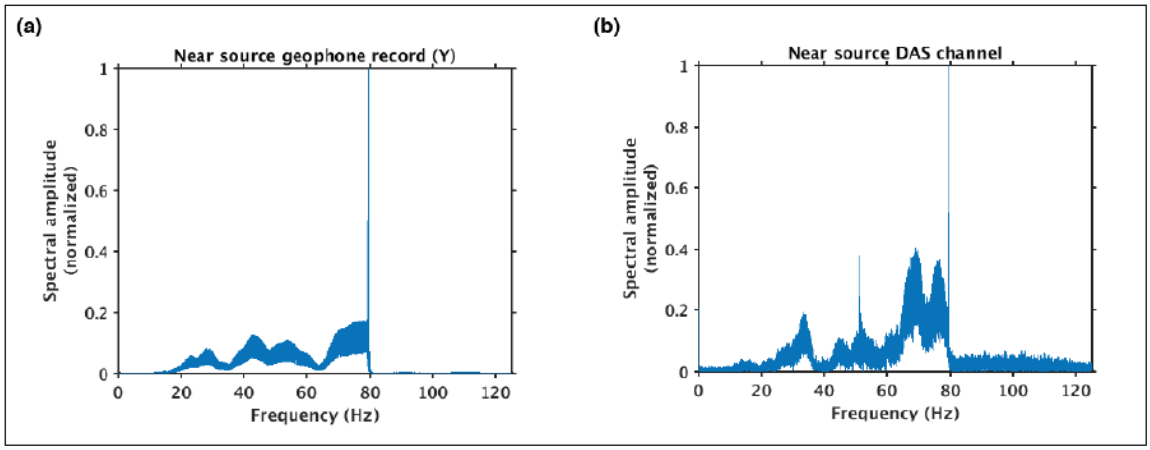

Figure 34. Ghost notches affect both source-monitoring geophones (a) and DAS channels (b).

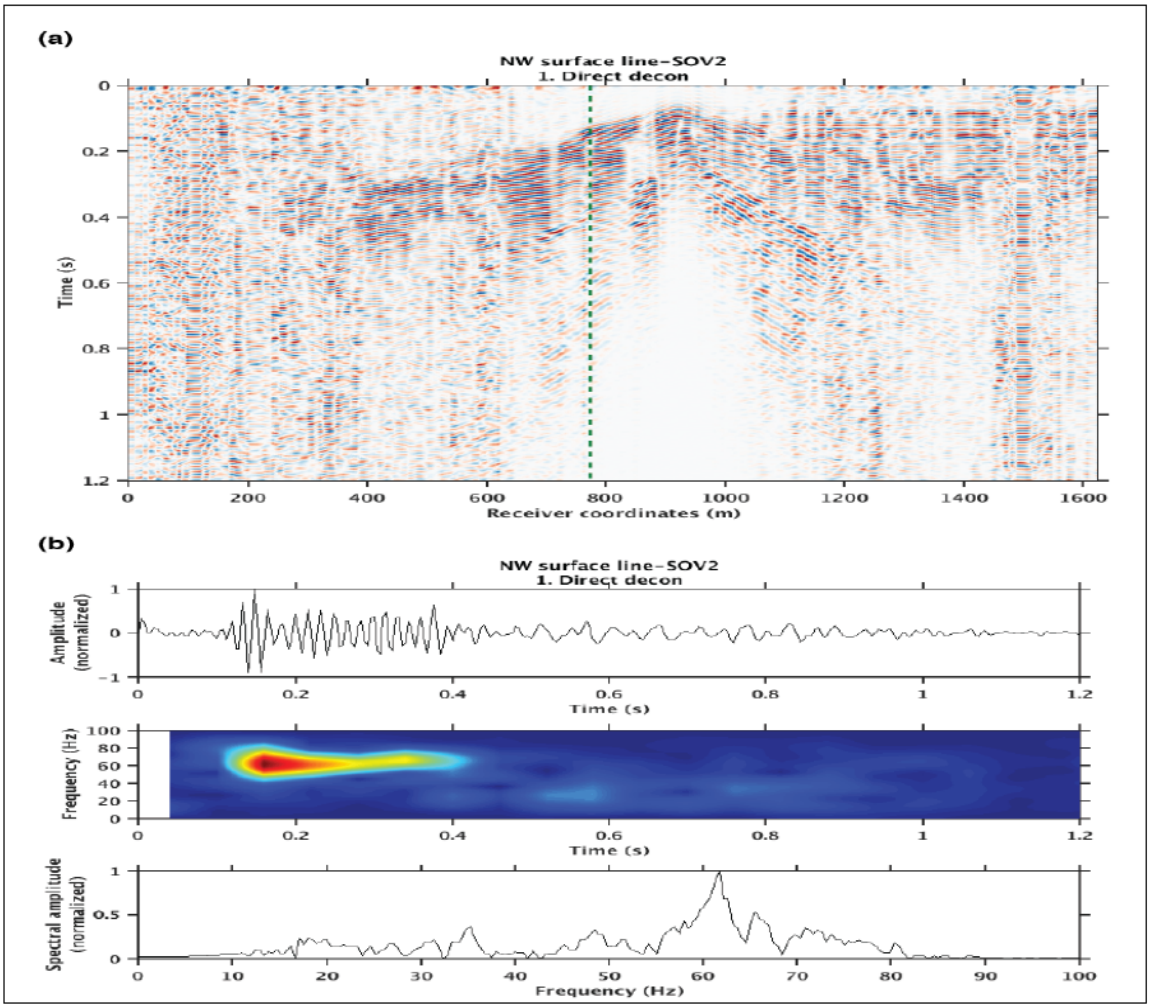

Figure 35. Example of ringing effects in a shot gather (after removal of source signature and ground rolls): (a) Time-space display of a surface seismic common-shot gather; (b) zoom-in view of a near-offset trace (labeled by green dash line in panel a) with a strong ringing component at 62 Hz.

Preliminary deghosting results

Spectral shaping is a frequently-used deghosting approach, in which practitioners reshape the notchy spectra into a more desirable shape. Currently we have not completed the development of a spectral template to filter to "deghost" the data, we are attempting to both preserve the dominant frequency band (10–80 Hz) while suppressing the ringing band around 60 Hz. Figure 36 is an example of a shaping filter we used to re-adjust the weights of the harmonic constituents.

We tested two ways of applying the spectral shaping. The first approach is to reshape the spectra after source-signature removal. From Figure 37, one can see a discernable change however the improvements are not sufficient. The second approach is to reshape the spectra both before and after source-signature removal. From Figure 38, one can see more noticeable improvements in the compactness of the resulting gathers.

The sweep generated by the SOV motor is recorded by a near-field geophone, which provides the source signature used for the deconvolution process. During the commissioning of the system, a 3-component geophone was installed for each SOV location at a depth of 60 ft. This depth was chosen as it was expected it would decrease the effects of the near-surface on the sweep signature while decreasing ambient noise. Given that the data processing techniques presented here were not sufficient to achieve the desirable data quality with no ghost effect, the next step was to reinstall the geophone at a shallower depth where the ghost notch would not interfere on the frequency band of interest. Therefore, in 2018, a shallow geophone was installed at 10 ft depth for each SOV location, in an attempt to improve the source signal. Figure 39 shows the sweep signature in time for the original geophone at 60 ft and the shallower geophone at 10 ft. Figure 40 shows a comparison of the frequency spectrum of the geophone signature at 60 ft depth (orange) and at 10 ft depth (green). A clear notch at approximately 50 Hz is seen on the 60 ft geophone. The notch seen in the frequency spectrum is probably a "ghost" reflection, which generates destructive interference at 50 Hz. When the geophone was installed at 10ft depth, the notch was not seen on the data.

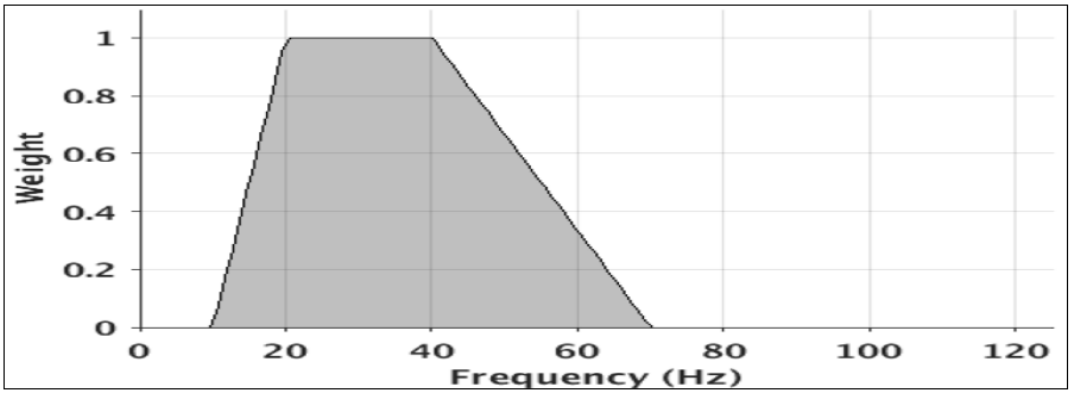

Figure 36. Spectral shaping filter (flat at 20–40 Hz) used for deghosting.

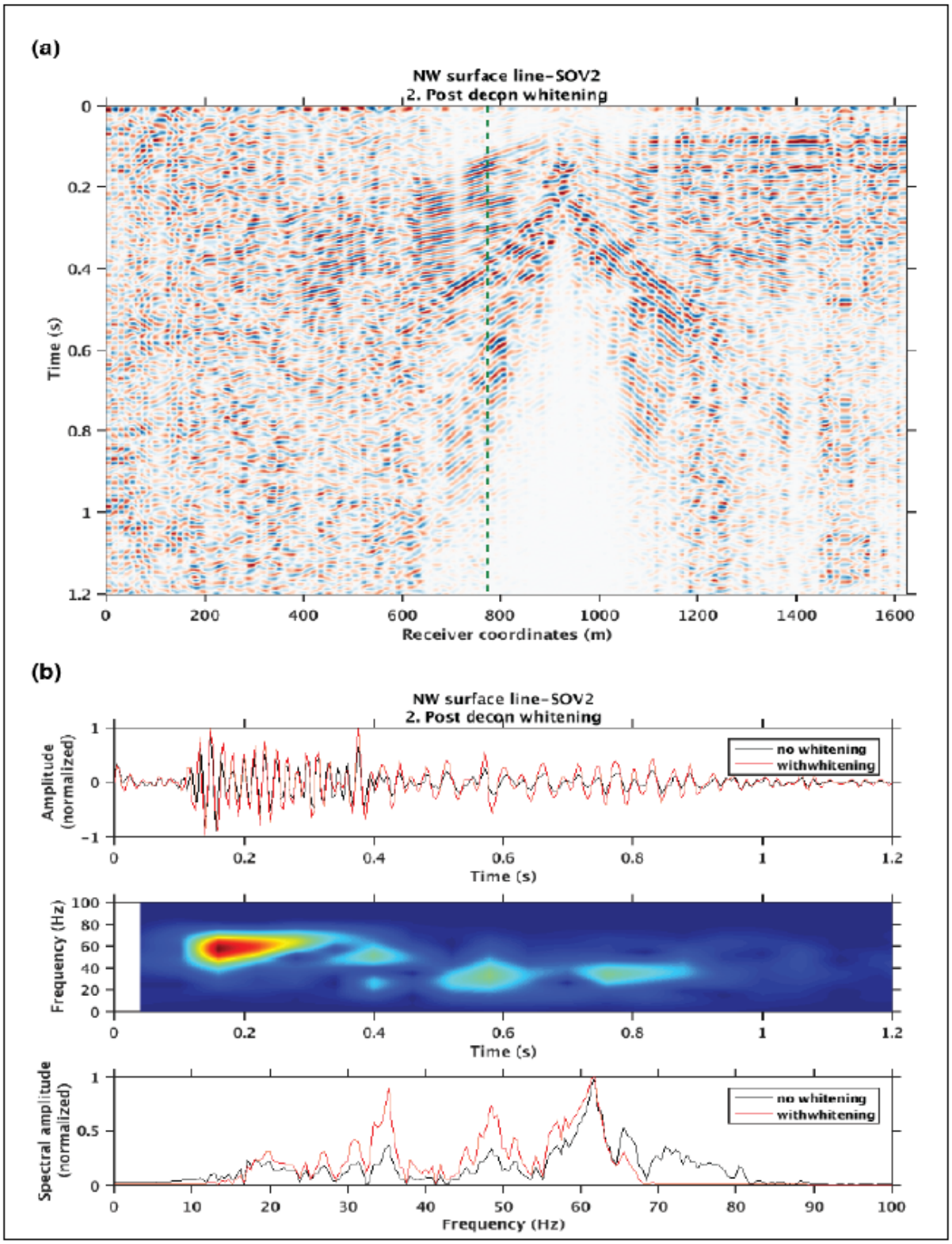

Figure 37. Same common-shot gather as in Figure 35, but with spectral shaping applied to after source-signature removal (i.e., post-deconvolution spectral whitening).

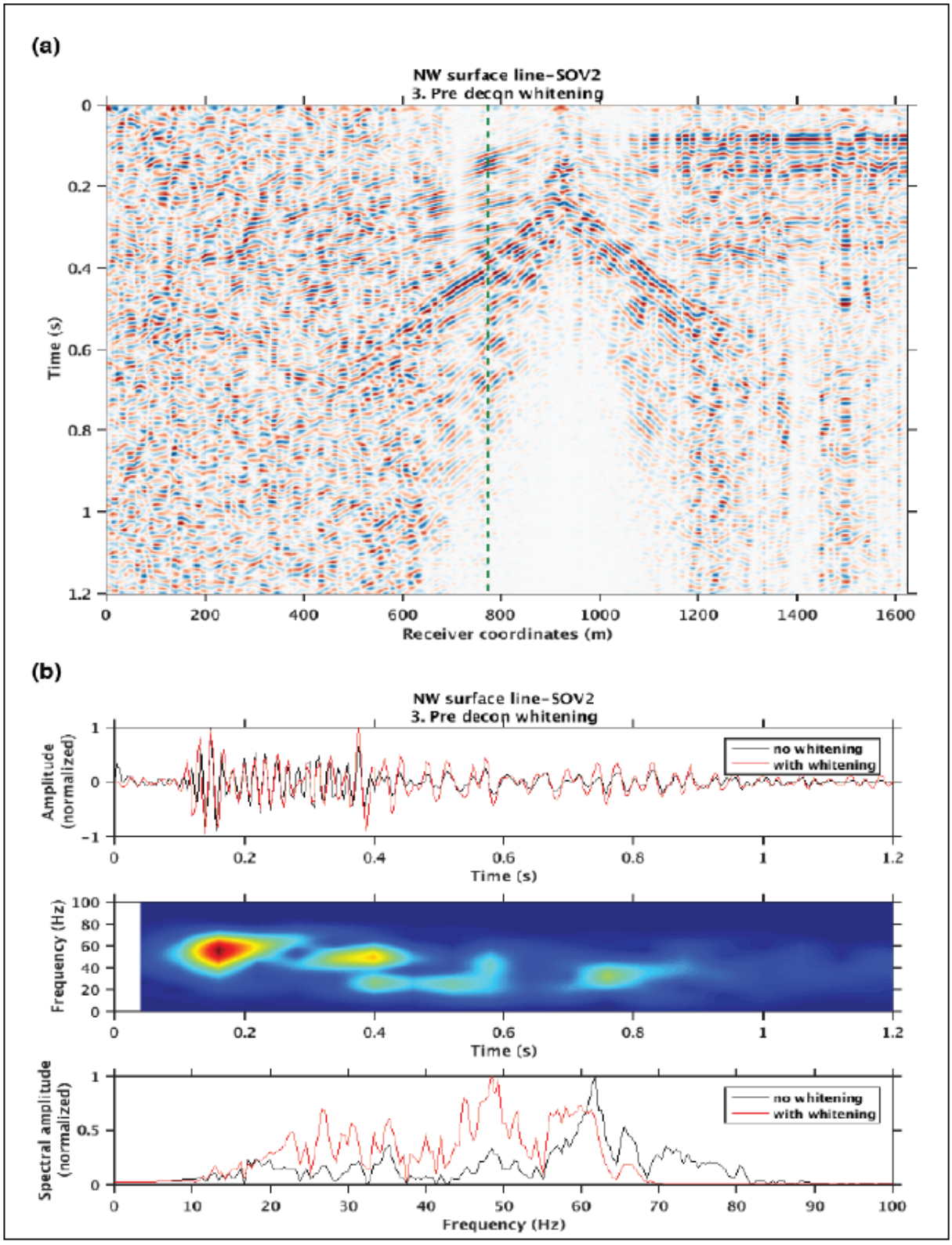

Figure 38. Same common-shot gather as in Figure 35, but with spectral shaping applied to both before and after source-signature removal.

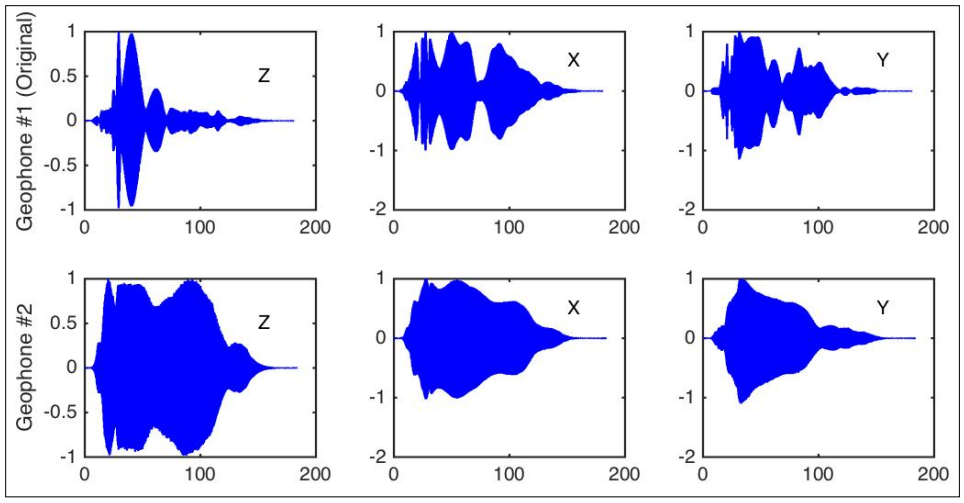

Figure 39. Three component near-field geophone record, in time. Top row shows the geophone instaled at 60 ft depth. The bottom row shows the record for the geophone installed at 10 ft depth.

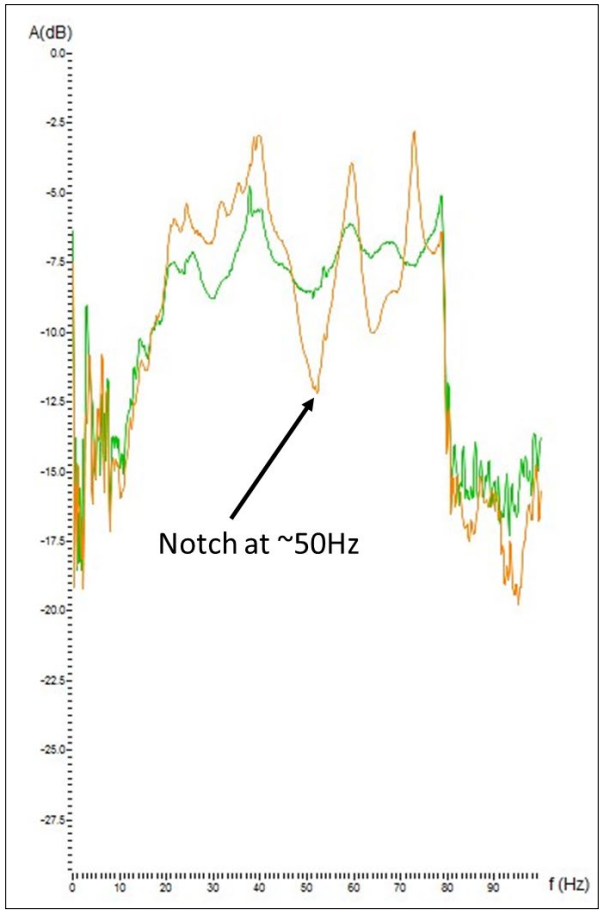

Figure 40. Amplitude spectrum of the original geophone installation at 60 ft depth (orange) and the new installation of the geophone at 10 ft depth (green).

Pre-processing

The pre-processing step involves matching the DAS with the sweep files generated by the SOV sources. The DAS data is matched with the sweeps by using a script in Matlab. The DAS data is acquired simultaneously, while the sweeps are recorded by the local SOV geophone and contain the time the sweep started. The script compares the start time of the sweep and matches it with the DAS monitoring (recording) files. Next, the data is deconvolved with the sweep to obtain a zero-phase wavelet. The geographical coordinates are then assigned to the data after deconvolution and the data is then saved on SGY files.

After saving the data in SGY file, the data files are upload into a seismic processing software (RadEx Pro). The first step is to stack the daily sweeps (30 per SOV) for each individual SOV. The sweeps are stacked for each direction of the rotation (15 clockwise (CW) & 15 counter clockwise (CCW)) for each SOV. Figure 41 shows the data acquired by the NW DAS line stacking the sweeps from SOV#2. Please note that as you stack the sweeps, the SOV seismic source signal as recorded by the DAS unit becomes stronger as the random noise stacks out (increasing the signal to noise ratio). Additionally, 5 adjacent traces were stacked to further increase the signal to noise ratio.

Noise Attenuation and Data Enhancement

The noise attenuation step involves the attenuation of random (background) noise and noise associated with ground roll. Ground roll is a type of coherent noise generated by a surface wave, typically a low-velocity, low-frequency, high-amplitude Rayleigh wave. Ground roll can obscure signal and degrade overall data quality but can be alleviated through the use of filters and stacking parameters. Therefore, several different tests were performed with the objective to develop a data processing flow that attenuates most of the noise, while protecting signal fidelity. First, a band pass filter was applied from 5 to 85 Hz (taper from 5-10 and from 75 – 85). The ground roll noise affects a large portion of the dataset, especially for the SOV sources located closer to the DAS line (i.e. SOV#1, SOV#2, and SOV#3 are near the NW line). Because ground roll noise is generated by slow moving surface waves, they arrive at a similar time as the SOV generated P-wave reflections moving through the target area (injection zone - Mt Simon Sandstone). Regarding the more distant SOV sources, the surface waves arrive after the reflected P-waves and have little effect on data quality. To attenuate ground roll noise, a “ground roll” model was developed to predicted (simulate) the noise (surface waves) experienced at our site. To develop the ground roll model, first a band pass filter is applied from 5 to 30 Hz, which approximates the ground roll frequency band. Next, an FK filter is applied to separate the velocities up to 1800 m/s. Finally, the ground roll (noise) simulated by the model is subtracted from the dataset. The final step of the noise attenuation data processing flow is the application of a 2D spatial filter followed by FX Predictive Filter. Figure 42 shows the data for SOV#2 data acquired on NW DAS line before and after noise attenuation. The left panel shows the data before noise attenuation. The middle panel shows the ground roll noise predicted by the model. The right panel shows the data set after

subtracting the ground roll noise. After noise attenuation, spiking deconvolution is applied to enhance the wavelet shape followed by predictive deconvolution to decrease the ringing in the near surface. Figure 43 shows the dataset before and after picking and predictive deconvolution for monitoring data acquired on the NW DAS line using SOV#3 as the seismic source.

2-D geometry is applied to the data, with bin size of 15m. After that, normal moveout (NMO) correction is applied to the data. The velocities used are 1-D velocities that were chosen by testing with the common depth point (CDP) gather. The CDP bin are then stacked. Figure 44 shows the stacked data for NW line and SOV#3. P reflection can be seen until approximately 800 ms.

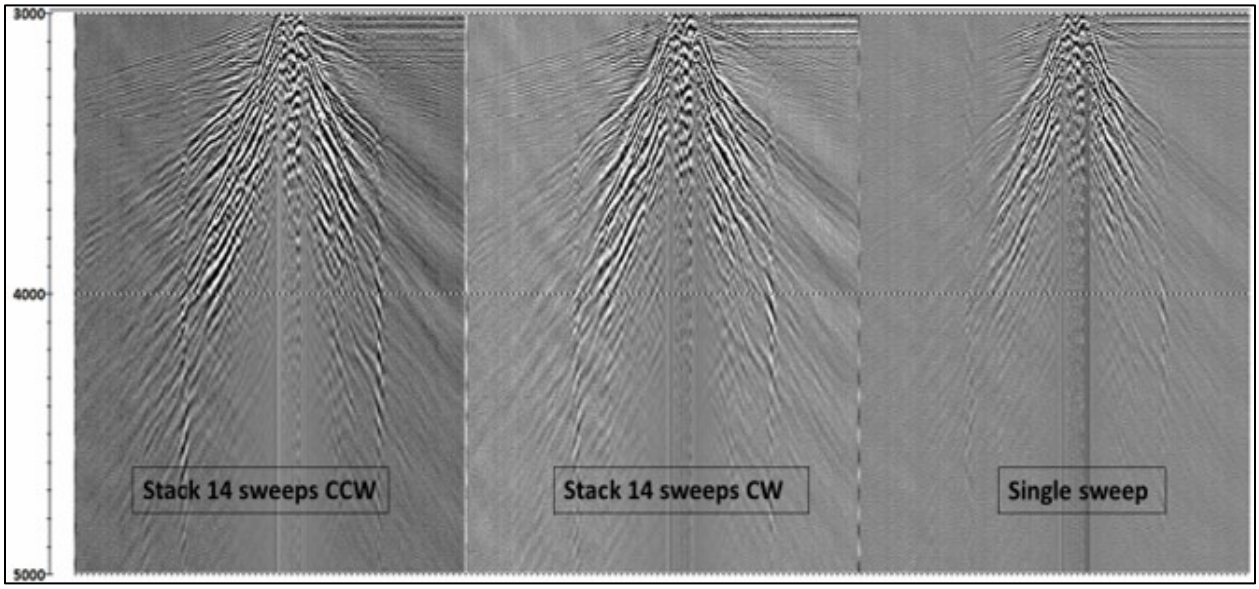

Figure 41. From left to right: DAS data on NW line stacked over 14 different sweeps from SOV#2 in one direction; DAS data on NW line stacked over 14 different sweeps from SOV#2 on the other direction; DAS data on NW line acquired with a single sweep from SOV#2 source.

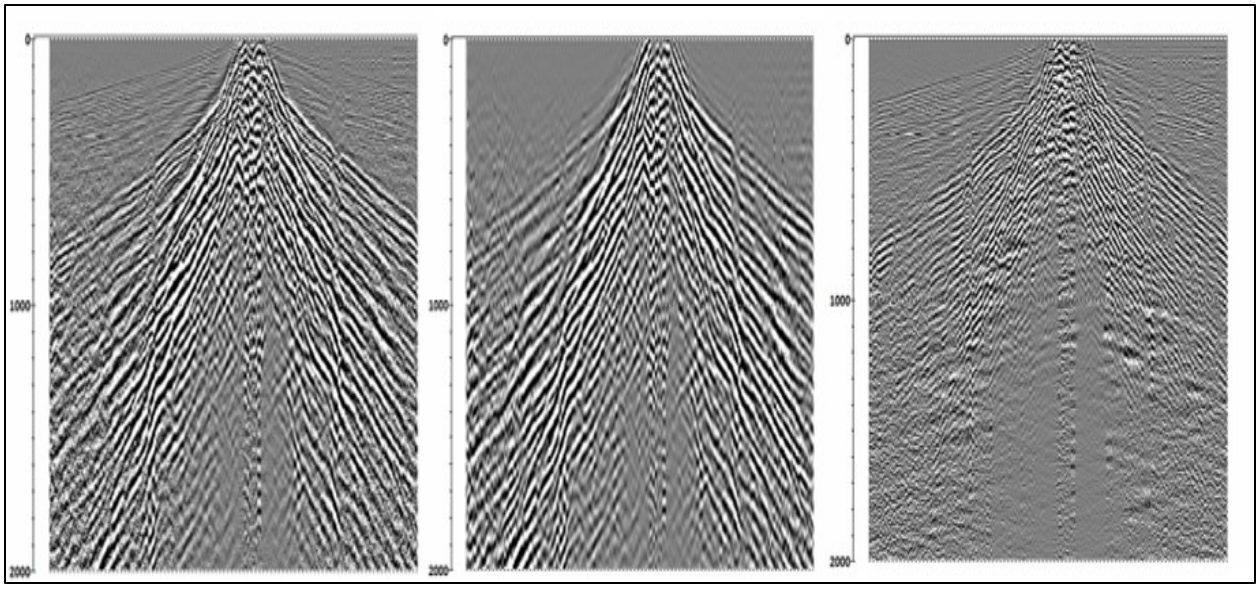

Figure 42. DAS/SOV#2 data acquired on NW line after noise attenuation. The data before noise attenuation is on the left. The middle panel is the modeled noise produced by ground roll. The right panel is the data set after subtracting by the ground roll noise.

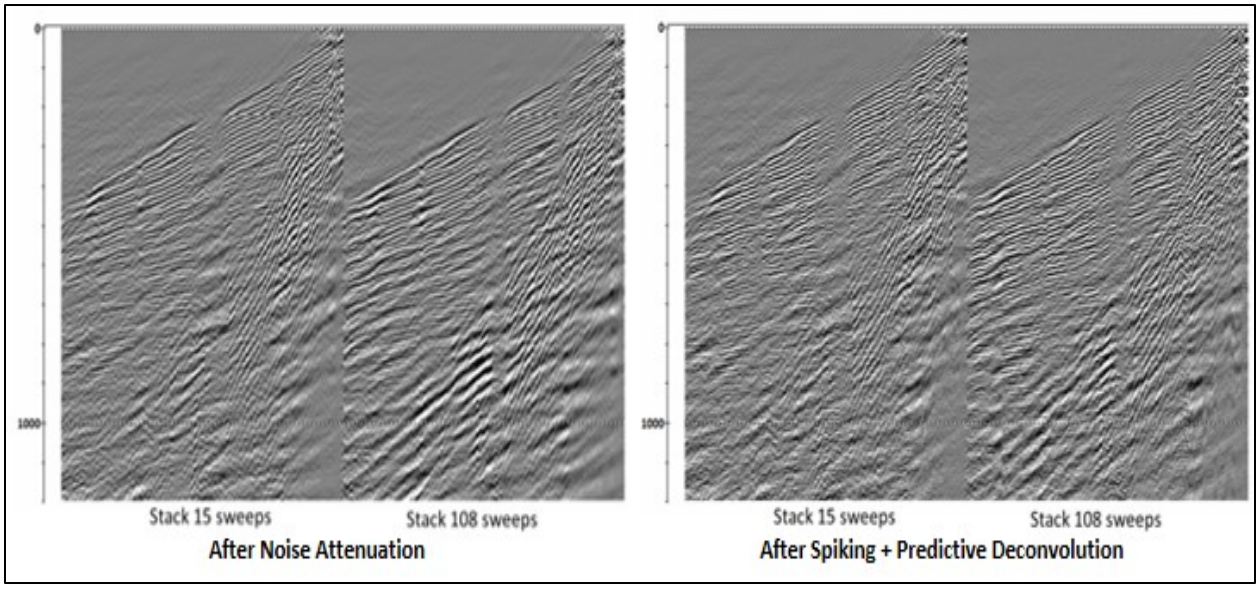

Figure 43. Comparison of data acquired on NW line using SOV#3, before and after deconvolution.

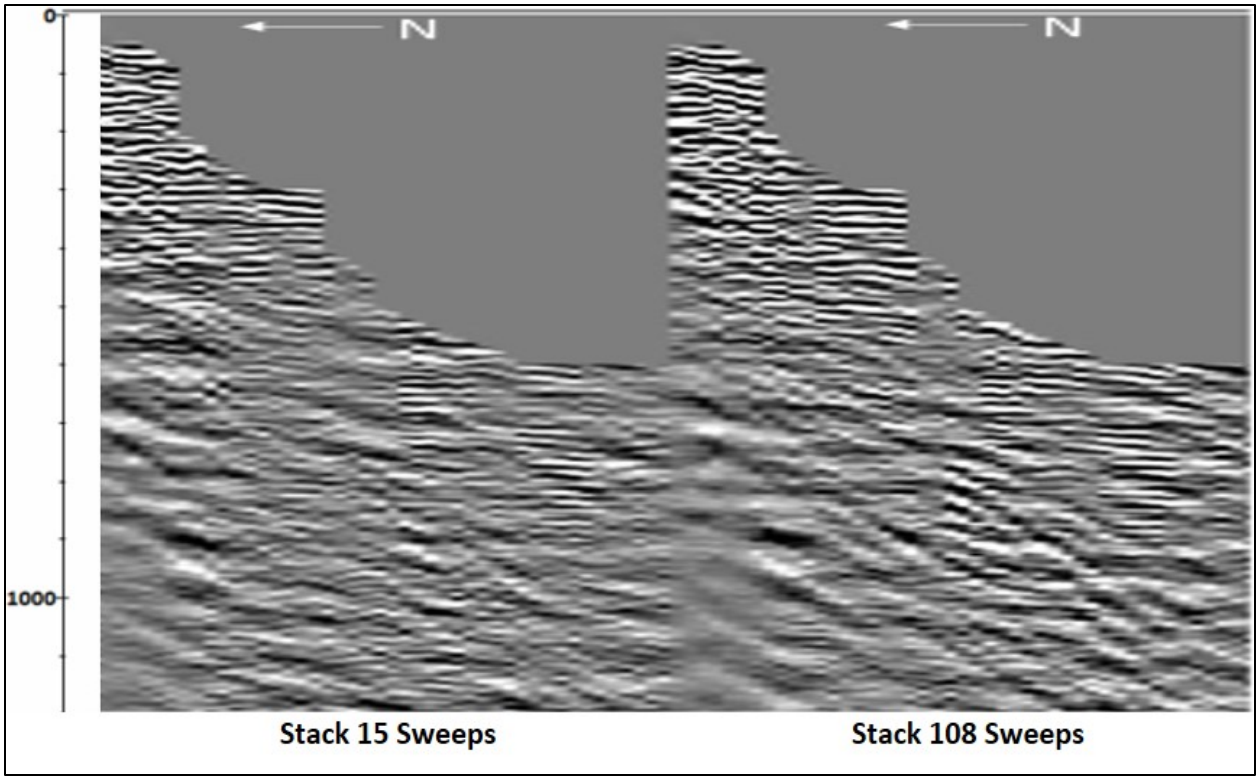

Figure 44. CDP stack for line NW/SOV#3 using 15 sweeps (left panel) and 108 sweeps (right panel).

Sweep Design Test

A sweep design test was performed on March 13th 2019. The objective of the test was to determine if modification of the current sweep parameters will improve data quality. The historic sweep parameters consist of a 0 to 80 Hz sweep cycle using a 30s acceleration time and a 150s deceleration time. During the test, the acceleration parameter was changed from 30s to 90s. Figure 45 compares the noise attenuated data acquired on the NW line using SOV#4. The left panel is a 5 sweep data stack of the test sweep cycle using a 90s acceleration time. The middle panel is a 5 sweep data stack using the historic (30s acceleration) sweep cycle acquired on the same day. The right panel is a stack of 90 sweeps, acquired during February, using the historic sweep parameters. Note that a stack of 5 sweeps using the new parameters, shown in the left panel, is comparable to a stack of 90 sweeps using the historic parameters. Figure 46 shows the frequency spectrum from the 3 datasets (5 sweep stacks with 90s acceleration, 5 sweep stack with 30s acceleration, and 90 sweep stack with 30s acceleration). Note the data with 90s acceleration sweep contains flatter frequency response. Also the frequency content of the data from the new sweep parameters is stronger from 22 to 32 Hz and from 60 to 80 Hz when compared to the old sweep parameters. Figure 47 shows the NMO corrected 2D line acquired with the 90s acceleration with 5 sweeps stacked on the left panel. The middle panel is the data acquired in the same day for the historic sweep design, also stacked with 5 different sweeps. The right panel a stack of 90 different sweeps,

acquired during February, using the usual sweep with 30s acceleration. The new sweep with 90s acceleration presents better resolution and stronger signal. However, the improvement was not sufficient yet to detect clear reflections from the injection interval.

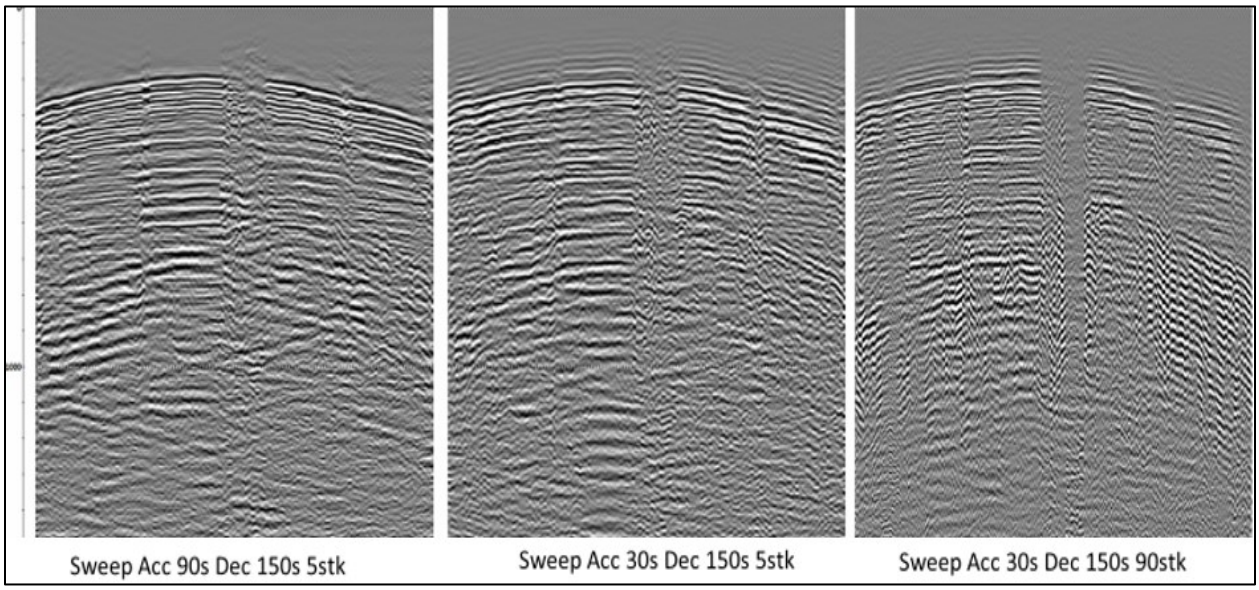

Figure 45. Data acquired with NW line and SOV#4, after noise attenuation. The left panel is the test with 90s acceleration with 5 sweeps stacked. The middle panel is the data acquired in the same day for the usual (30s acceleration) sweep design, also stacked with 5 different sweeps. The right panel a stack of 90 different sweeps, acquired during February, using the usual sweep with 30s acceleration.

Figure 46. Frequency spectrum comparison of the new sweep parameters vs. historic using SOV#4.

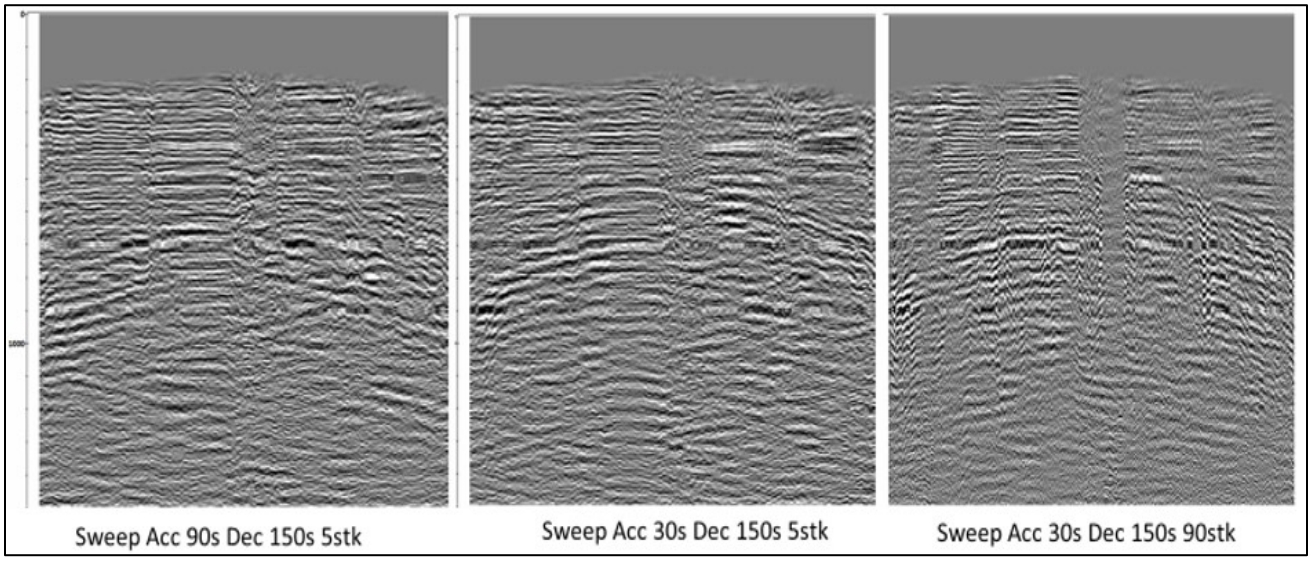

Figure 47. SOV#4 with NMO applied for the test sweep and the previous sweep.

Peak Force Test

We tested changing the signal impulse force of the sweep from a peak force of 70% to a peak force of 100%. Figure 48 shows the data from the NW DAS line using SOV4. The data after increasing the peak force to 100% shows stronger reflections, especially at the near surface. However, no significant improvement is seen in the dataset. We decided to program the sweeps with increased peak force given it still presented an improvement, though small, on shallower reflections.

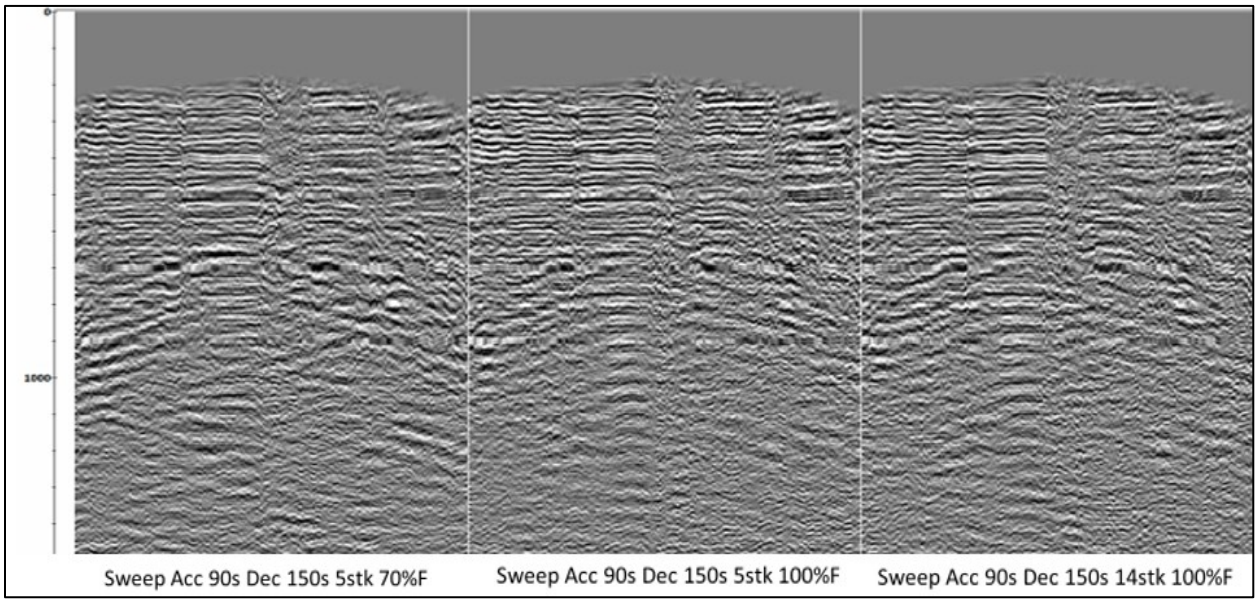

Figure 48. Data acquired with NW line and SOV#4. Sweep with 70% peak force on the left panel with 5 sweeps stacked. Sweep with 100% peak force on the middle panel with 5 sweeps stacked. Sweep with 100% peak force on the right panel with 14 sweeps stacked.

Repeatability Test

A repeatability test was conducted using the sweep data acquired using SOV4 on the NW DAS line. The repeatability was tested by comparing the data acquired in January 2019 and the data acquired in February 2019. The lower the repeatability value, the more similar are the two datasets. Repeatability is important in monitoring the injected CO_2 plume in the reservoir because we want to insure that any changes observed in the amplitudes of the dataset are related to changes in the reservoir conditions caused by the injected CO_2. Figure 49 shows the repeatability calculated for the NW line and SOV4 dataset between January and February. The datasets have 90 days of sweeps stacked and they have noise attenuation applied. Repeatability up to 40% can be seen until approximately 500ms. Below 500 ms the data repeatability is poor. To improve the repeatability, the signal levels should be stronger relative to the noise levels. For this, an option is to increase the strength of the source signal. However, the low levels of signal in the seismic are mostly attributed to the strong angle sensitivity of the DAS measurement, which only records one component of the wavefield. For a horizontally deployed fibers, DAS is mostly sensitive to waves

polarized horizontally, that is ground roll and S-waves. The deployed HWC improves the angle sensitivity for P-waves given that the fibers are horizontally deployed. However, for reflection arrivals of above 500 ms, the signal levels appear to be not sufficient.

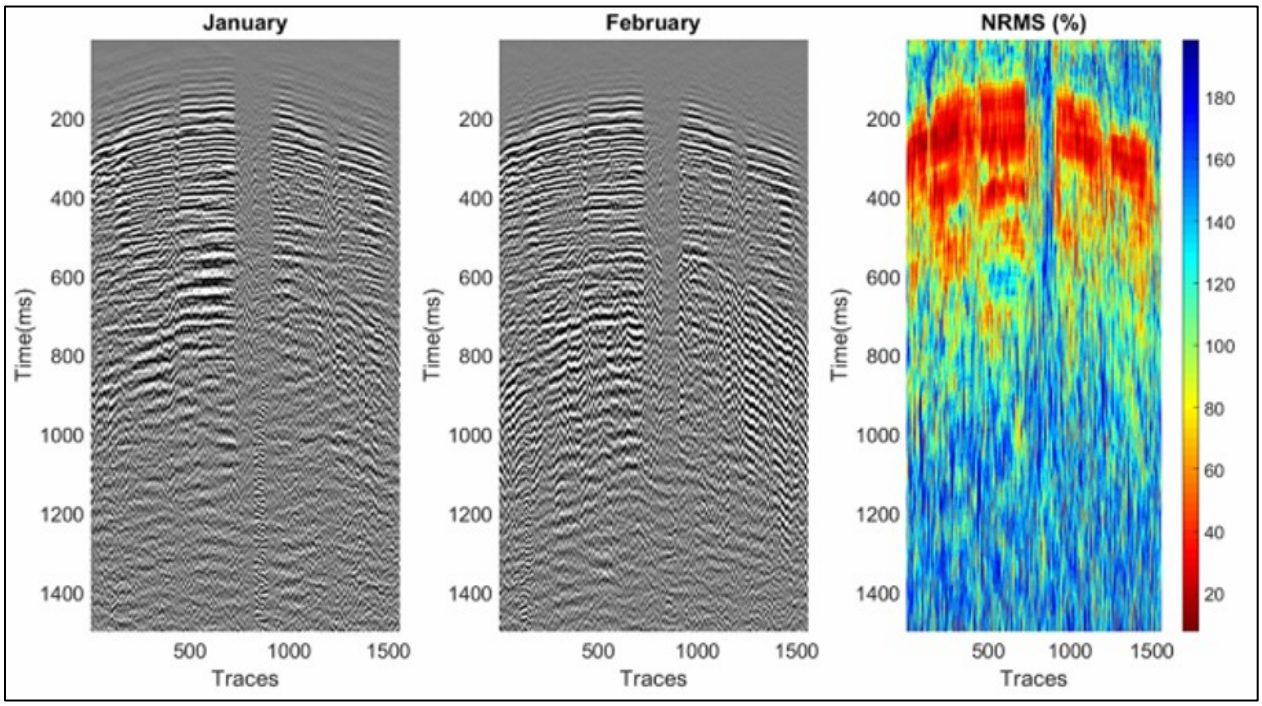

Figure 49. Calculated NRMS for data on NW/SOV#4.

Engineered fiber data analysis

One of the options to overcome the low signal sensitivity of the DAS data on site is to use engineered fibers. Both NW line and NE surface lines are instrumented with high-sensitivity fibers, manufactured by Silixa (Naldrett et al., 2020). A survey was conducted in July 2019, with the objective to test and analyze the any improvement in data quality when acquiring the DAS data using engineered fiber. The engineered fiber can only be connected to a different version of the interrogator unit (the iDASv2 is used on-site, and the engineered fiber can only be connected to iDASv3). For this, we scheduled a field work with Silixa from the 1-2 of July in order to acquired data using the high sensitivity engineered fiber and Silixa's interrogator unit iDASv3. During the field work, we acquired data on all five SOVs. Figure 50 shows an example of a sweep acquired using SOV4. Note the section of the cable containing the engineered fiber (Constellation) is significantly more sensitive in detecting signal than the section of the cable containing single-mode fiber.

The acquired data with the engineered fiber was processed using Vista seismic processing software. The seismic processing flow involves sweep stack (15 sweeps stacked for each direction), summation of CW and CCW directions, noise attenuation (signal scaling, band pass filter from 10 to 80 Hz, frequency variant median filter, FX predictive decon). After noise attenuation, the velocities were picked on the filtered data set to generate a velocity model (Figure 51). Using the picked velocities, a brute stack for NW/SOV4 line was generated and then migrated (finite difference post-stack migration).

Figure 52 shows the NW/SOV4 migrated 2D seismic line. The line shows reflections associated with the main geological layers. However, strong noise patterns and lack of continuity of reflections are still issues that need to be addressed. A synthetic seismogram was created using the density log and sonic log acquired in CCS2 well. The synthetic seismogram was tied to the seismic line, and with this, a time-depth curve was generated. The comparison of the synthetic seismogram and the 2D seismic line shows that the reflections at 460 ms, 750 ms, 800 ms, and 980 ms match well. The reflection at 750 ms corresponds to the Eau Claire sequence, which is the cap rock for the Mt. Simon (monitoring zone). Mt. Simon reflection on the 2D line also corresponds well with the reflection in the synthetic seismogram. The Mt. Simon is the target sequence for monitoring. For this reason, we recommended that the preferred interrogator for the data acquisition would be a Carina iDASv3, which supports the use of engineered fibers.

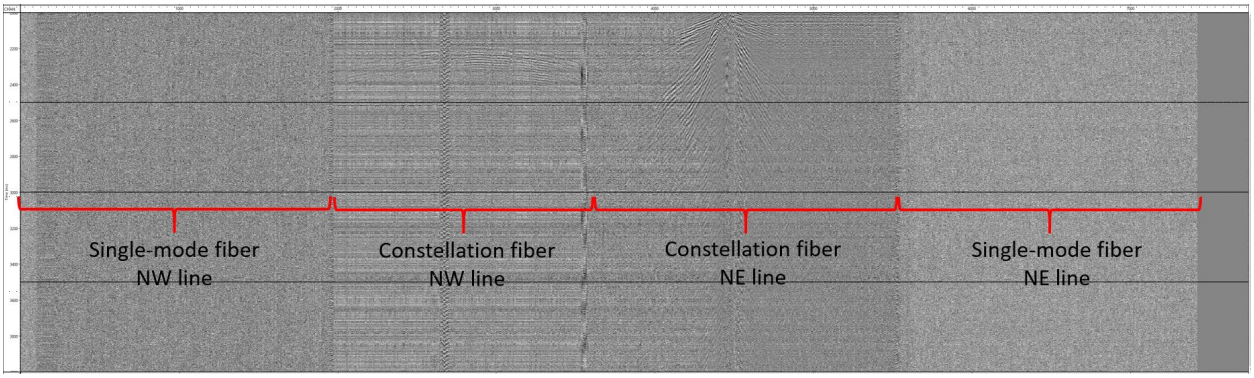

Figure 50. Example of one sweep recorded on the fiber-optic cable installed on the surface on NW and NE lines. The cable contains a combination of single-mode fiber and engineered fiber (Constellation) deployed from CCS2 well towards NW line (single-mode), then returning to CCS2 well (Constellation, and deployed on NE line (Constellation), and returning to CCS2 well (single-mode).

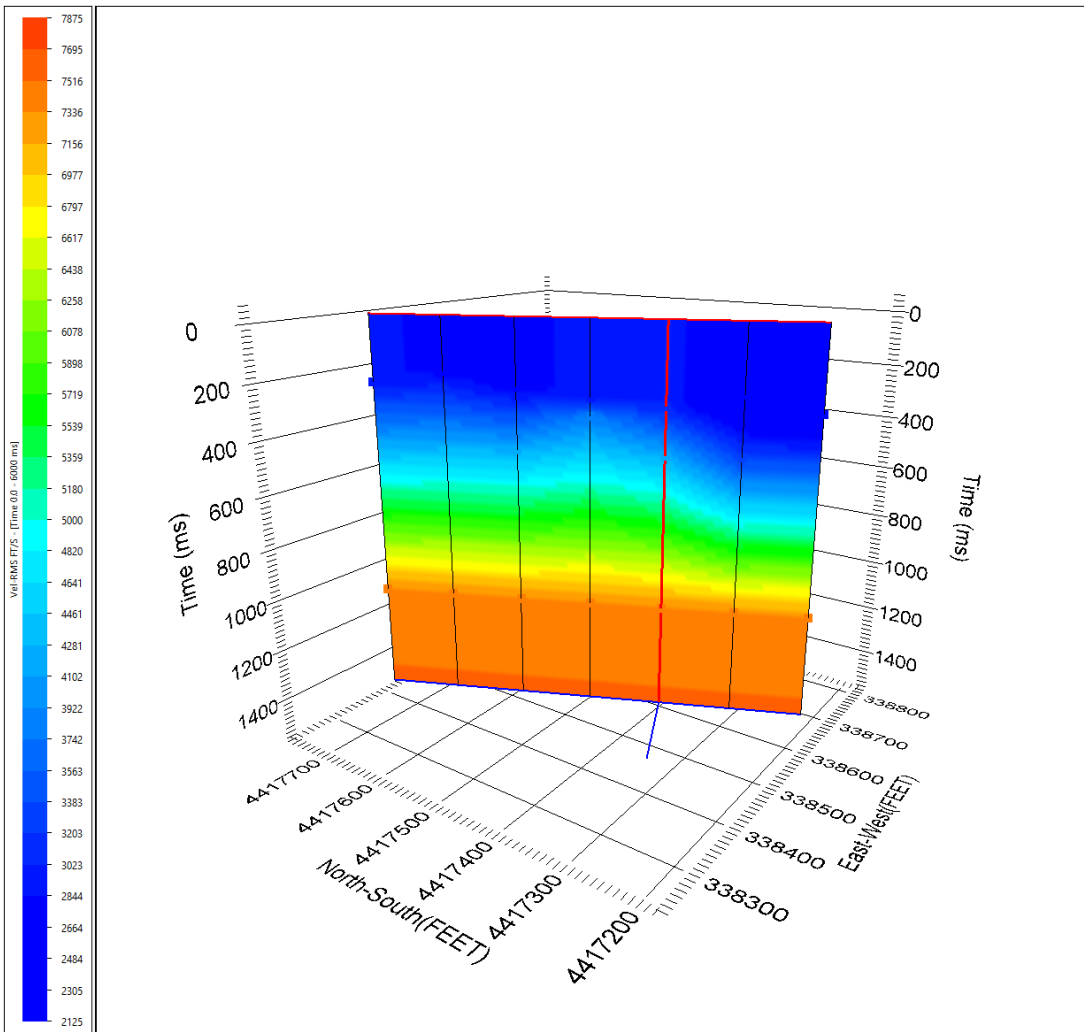

Figure 51. RMS velocity picked on filtered data acquired on NW line with SOV4.

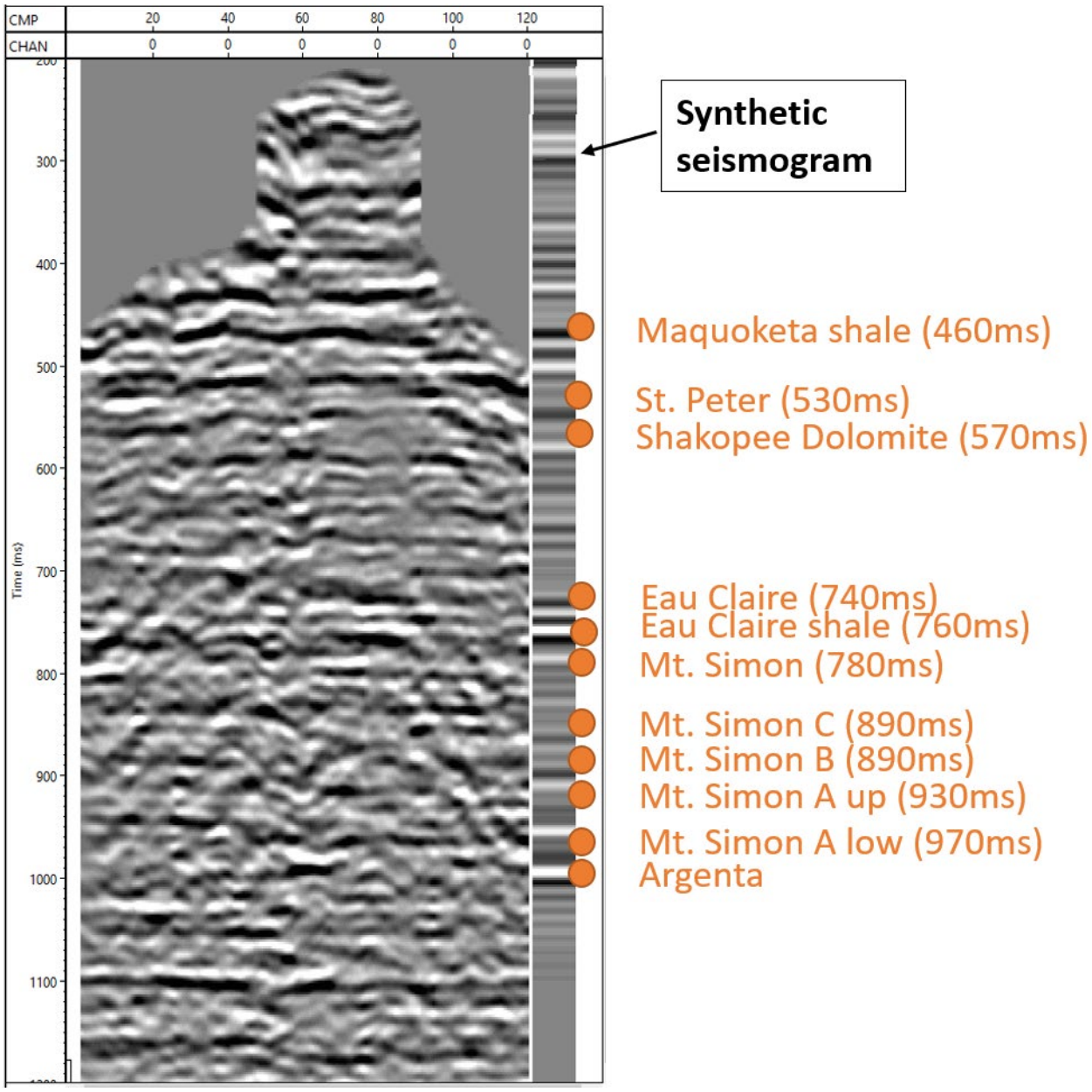

Figure 52. 2D seismic line (left) after migration acquired on NW line with SOV4 using Silixa's engineered fiber (Constellation). A synthetic seismogram was generated (right) using the sonic and density logs form CCS2 well. Markers for the main sequences are displayed in orange.

To further investigate if the reflections seen on the data correspond to real reflections from geological interfaces, we perform raytracing using the well-top information. The raytracing exercise is meant to simulate the P-wave reflection response, using the SOV4/NW geometry. The shot gather acquired with engineered fiber on NW line and SOV4 shows a strong reflection at approximately 800ms (Figure 53). The reflection is mostly seen on the close offset traces, and the continuity of the reflection is affected possibly due to issues in coupling along the well. From the

raytracing response, the reflection correspondent to the Eau Claire Shale (cap rock), matches with the reflection at ~800 ms seen on the shot gather. This indicates that this reflection seen on the migrated data and on the shot gather are related to real interfaces.

Although we can see P reflections on the DAS data acquired with engineered fiber, the data quality is still not sufficient to perform time-lapse monitoring. One of the most significant limiting factors on the data quality is the strong angular sensitivity of the DAS method to broadside waves, which means the amplitudes of P-waves on DAS decay as cosine square of the angle of incidence (Kuvshinov, 2016). Although the helically wound cable improved the angular sensitivity, in practice the improvement was not sufficient to detect P-wave reflection from the target interval. Additionally, the presence of strong ground roll noise limited the usability of the near-offset sources as the ground-roll was masking any possible reflections. Ground roll is a type of coherent noise generated by a surface wave, typically a low-velocity, low-frequency, high-amplitude Rayleigh wave. Ground-roll noise was found to significantly affect the quality of the data on-site, especially for the SOV sources located close to the DAS line (i.e. SOV1, SOV2, and SOV3 are near the NW line). Because ground roll noise is generated by slow moving surface waves, they arrive at a similar time as the SOV generated P-wave reflections moving through the target area (injection zone - Mt Simon Sandstone). Regarding the more distant SOV sources, the surface waves arrive after the reflected P-waves and have little effect on data quality (i.e. SOV4 on NW line).

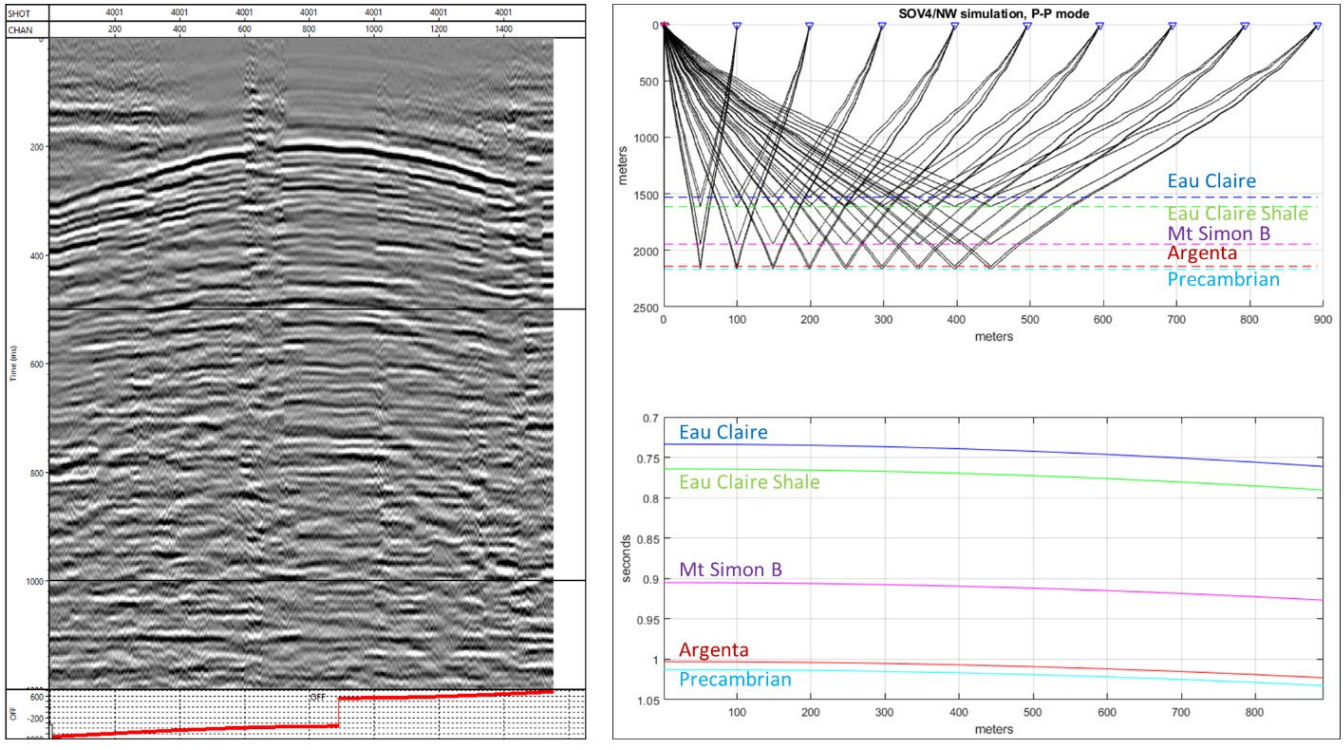

Figure 53. Shot gather acquired with engineered fiber on NW line (northwestern portion of the fiber-optic cable) with SOV4 after noise attenuation flow (left). Raytracing for simulated P response for SOV4/NW line (right) using well-tops information.

4.5 IMS Hydrogeological Inversion

A principal software component for the integrated IMS architecture is the inverse flow-modeling framework. Inverse (flow) modeling refers to the process of estimating those CO2 reservoir model parameters that have the primary influence on CO2 flow behavior over space and time. One primary model parameter type is permeability, which measures the ability of rock material to transport liquids or gases. Essentially, the inverse flow-modeling process will facilitate the development of a refined reservoir permeability model that is suitable for forecasting CO2 flow behavior. The more spatially refined the permeability model is, the better the forecasting ability, thus making monitoring and management decisions about the future injection process maximally informed.

The model-refinement process involves the integration of continuous flow and seismic measurements into the mathematical inversion process. Integration of seismic data, or other geophysical data, into an inverse flow-modeling framework is a methodologically and computationally elaborate process. We have developed an integrated framework that allows for different methodologies in order to make maximum use of the seismic data when the system will be online.

The first part of this chapter described the hydrological inverse modeling that was carried out in order to establish a baseline permeability model for subsequent coupled hydrogeophysical modeling. The second part will describe the approach for fully coupling flow modeling and the corresponding reservoir state prediction to seismic modeling.

PART 1: RESERVOIR PERMEABILITY MODEL DEVELOPMENT

History-matching through inverse modeling of pressure monitoring data delivers a first-order approximation of a reservoir model at an industrial-scale CO2 injection site. The reservoir model forms the backbone of an integrated monitoring system (IMS) for subsurface CO2 storage, which will ultimately encompass the integrated analysis of pressure-temperature and geophysical seismic monitoring data. First inversion results confirm the existence of a hydraulically isolating thin layer in the lower injection interval, known as mudstone baffle.

An essential component of the IMS is a reservoir model capable of (1) adequately simulating the injection process, (2) accurately predicting pressure responses in monitoring zones, and (3) coupling to a seismic modeling framework. The latter is described in Part 2 below and will ensure that reservoir properties and their fluid-induced alterations are properly mapped to seismic properties and corresponding seismic signal responses.

In Part 1, we address the requirements 1 and 2 as a preface to a coupled hydro-seismic reservoir modeling framework. Here, we summarize history-matching results of year-1 pressure monitoring data. These results yield a first-order approximation to a reservoir model, which is then refined by later data sets. The approach takes into account continuous data addition, once the seismic data stream would be fully established.

Curve-fitting of relative-permeability and capillary-pressure data

Fig. 39 shows measured curves of relative permeability and capillary pressure and their model predictions. Measurements pertain to Rock type I, which was identified by Zaluski & Lee (2019) as the rock type with the largest porosity and permeability. Commonly used models for predicting relative permeability and capillary pressure, like the van-Genuchten-Mualem or the Brooks-Corey model, were originally developed for conventional oil and gas reservoirs.

To obtain a better curve fit than can be obtained through fitting of common-model coefficients, we implemented a polynomial curve-fitting approach. Its predictions are shown in Fig. 39 together with the corresponding observations. Polynomial-function coefficients were pre-determined by means of curve-fitting and were kept fixed during all subsequent hydrological inverse modeling. Hysteretic effects were neglected during these inversions.

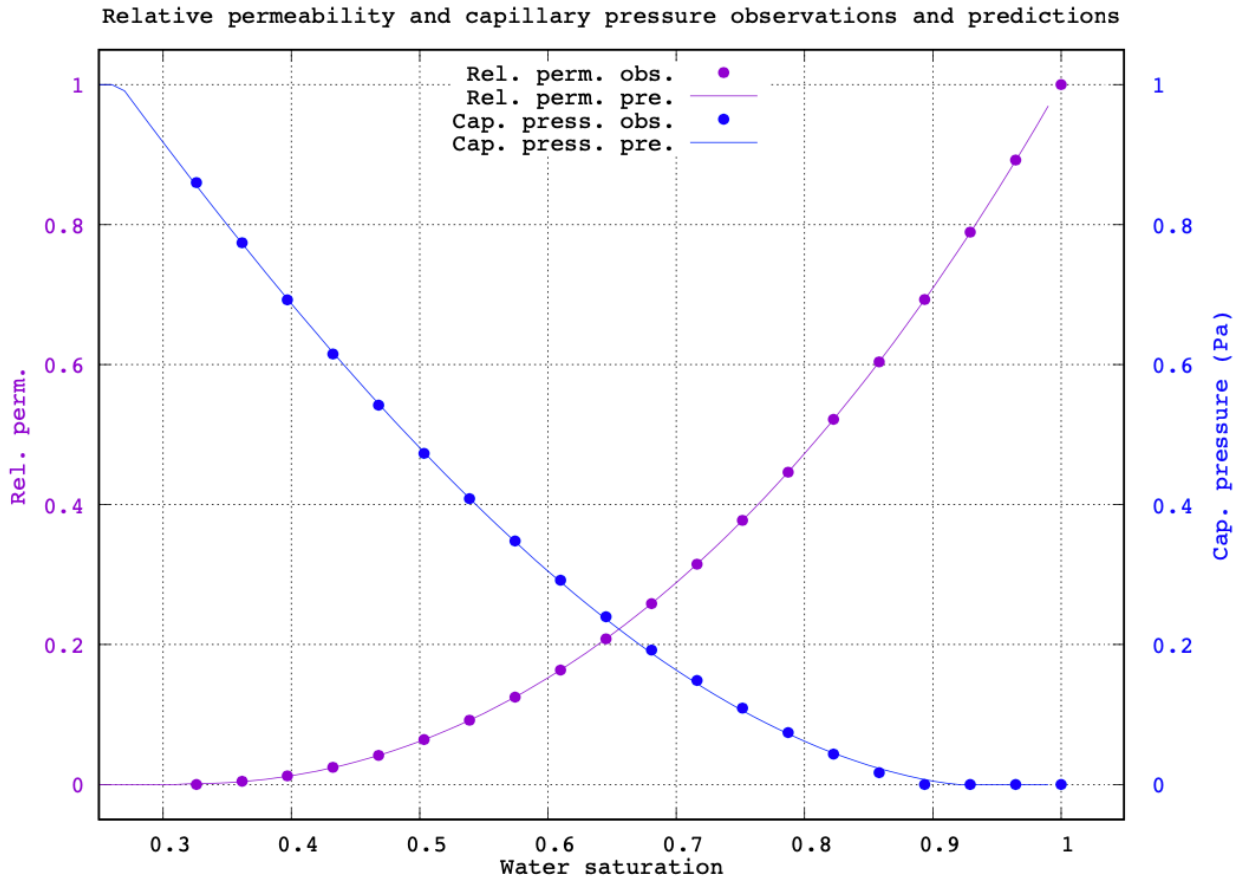

Figure 54. Relative permeability and capillary pressure data and their predictions. Predictions are obtained by means of polynomial curve-fitting.

Inverse modeling of pressure data using MPiTOUGH2 and radially symmetric flow model

We employ the inverse modeling framework MPiTOUGH2, which is a derivative of iTOUGH2 (Finsterle et al., 2016) combined with the parallel-computing capabilities of TOUGH-MP (Zhang et al., 2008), and further includes various geophysical simulators for electrical and seismic data types (Commer et al., 2014, Commer et al., 2020).

A radially symmetric TOUGH2 mesh with 11,288 cells and minimum horizontal/vertical cell size of 10m/5m describes the injection zone between the injection well CCS#2 and one of the monitoring wells (VW#2) at 2600 ft distance (Fig. 40). The injection occurs between 6630 and 6825 ft and is divided into four perforated intervals. Inverse modeling analyzes data from 5 pressure-monitoring zones spanning the depth range 4902-7041ft. The original VW#2 data covers the period 04/01/2017 to 03/31/2019 (total of 730 days), comprising 17717 hourly samples for each of the 5 zones (Fig. 40b). Pre-processing steps are de-spiking and removal of outliers so that the final data set totals 17321 samples per monitoring zone. Note that spikes in the pressure data occurred because of occasional reservoir fluid sampling, which shuts down the monitoring. The corresponding pressure drops cannot be modeled with the temporal discretization considered here.

Fig. 40b reveals that the pressure response dominates in Zone 2, which lies within the injection interval. The degree of response in the other four zones correlates with their vertical distance from the injection zone, that is, the gradual increases are rather linear, where Zone 5 remains mostly constant.

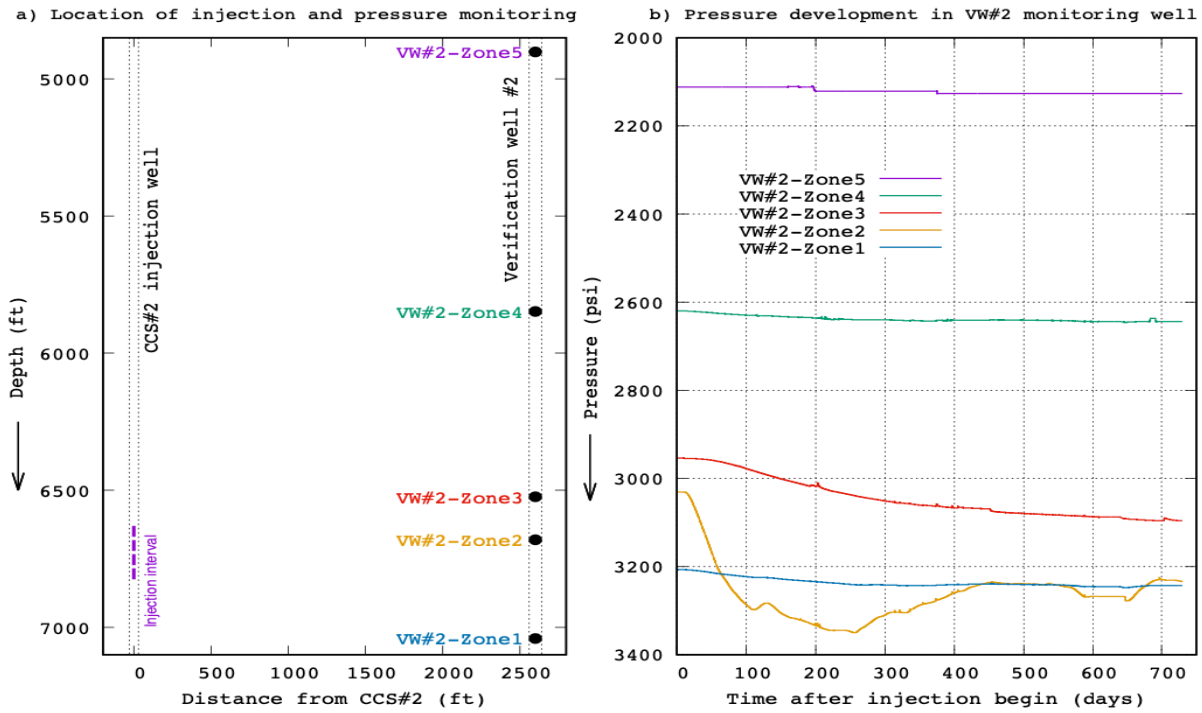

Figure 55. Hydrological inversion for a layered permeability model. (a) Schematic view of reservoir zone between injection well (CCS#2) and monitoring well (VW#2). (b) Five vertical monitoring zones in VW#2 produce pressure time-series data over the 730-day injection period. Note that the *y*-axis points downwards (with increasing pressure).

Incremental inversion approach for an intelligent monitoring system

The architecture of the intelligent monitoring system's flow-modeling component involves a multi-step inversion approach. An initial inversion analyzes the first data set that would be available during the injection process; here, this subset covers the first 260 days of the injection. The multi-step inversion further involves the addition of model parameters at a later stage when more data is available. In our case, the initial model is designed such that it describes gross permeability structures with few parameters.

Preparatory steps for the initial gross-structure inverse modeling include the delineation of the interfaces for a horizontally layered model of the intrinsic reservoir permeability. The fast computing enabled by MPiTOUGH2 (parallel forward-modeling combined with parallel Jacobian calculation) let us experiment with a pseudo Monte-Carlo approach, which involved approx. 100 trial inversion realizations. A true Monte-Carlo search would require many more realizations. A random scheme searched for the optimal number of layers with fixed interfaces, varying in number between 3 and 15. The Monte-Carlos modeling yielded that a 6-layer model parameterization suffices to describe the main characteristics of the observed pressure responses over the 260-day data set. The permeabilities is assumed isotropic.

P-data inversion for one-dimensional gross-structure (6-layer) permeability model

A 20-iteration Marquardt-Levenberg inversion run with the 6-layer setup took approx. 35 minutes using 72 cores of the Intel cluster purchased by ADM for this project.

Figs 41 and 42 summarize the final data fitting and model outcome after 20 inversion iterations, where the data fits in Fig. 3a are calculated from the final iteration's parameter estimates. In contrast to all other zones, the characteristic pressure development in Zone 2 involves an initially steep increase and a much more pronounced drop and rebound, correlating well with the large injection decrease at around 100 days (Fig. 41b). This correlation also appears in the data fits for Zone 2, although amplitudes of the pressure differences remain underestimated. On the other hand, the pressure difference during the first 50 days is overestimated for the adjacent Zone 3. However, we found that including additional thin layers between these two zones did not lead to improved data fits for these zones, indicating generally more complex model structures than given by the layered model.

The final model in Fig. 42 shows the estimated permeability, which ranges from 0.01 mD to close to 1000 mD over the 6 layers. No smoothing constraints were imposed on the estimation process, that is, we allowed for discontinuities at layer interfaces, as their existence is also suggested by well log data (see the geological section in Fig. 42).

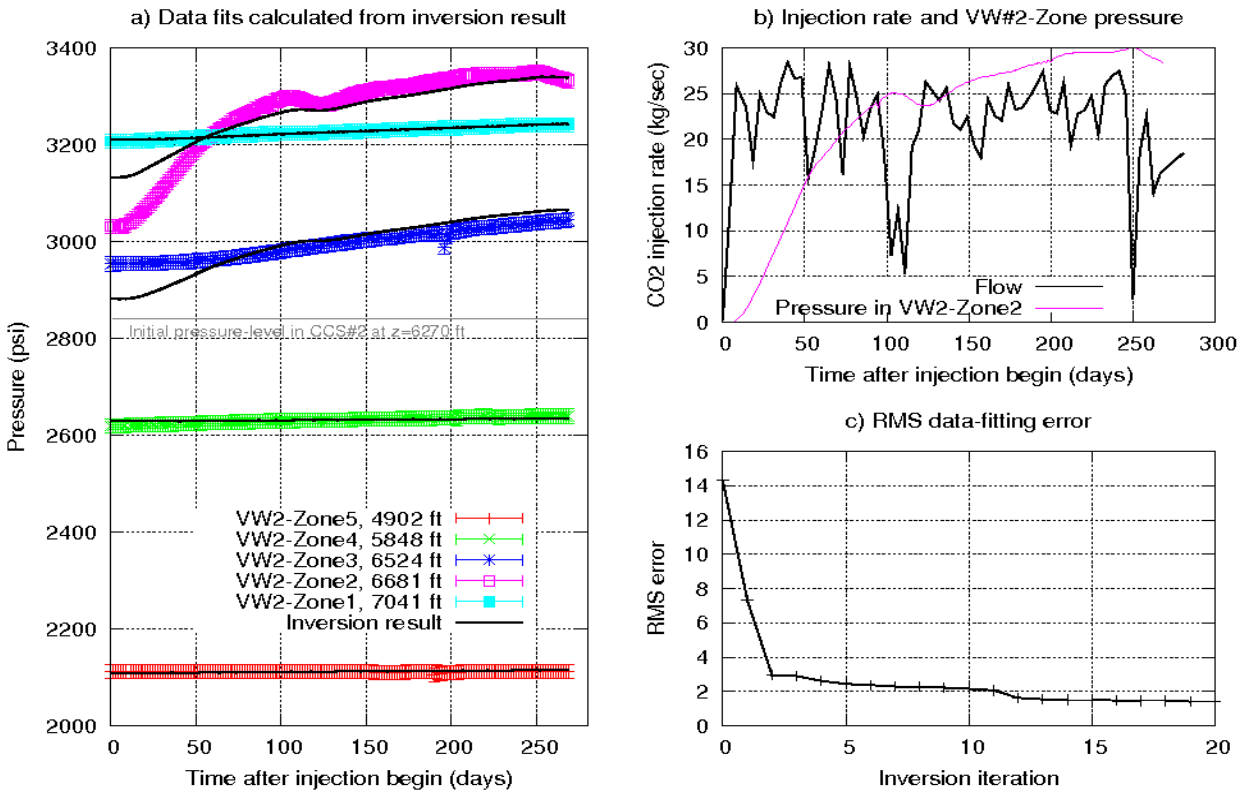

Figure 56. Hydrological inversion for a 6-layer permeability model. (a) Data fits (black curves) are shown together with observations and corresponding error bars. (b) Flow rate (in kg/sec) is shown together with the pressure evolution in VW#2 (Zone 2). (c) Total RMS fitting error over 20 inversion iterations. Error convergence occurs at the RMS of 1.4.

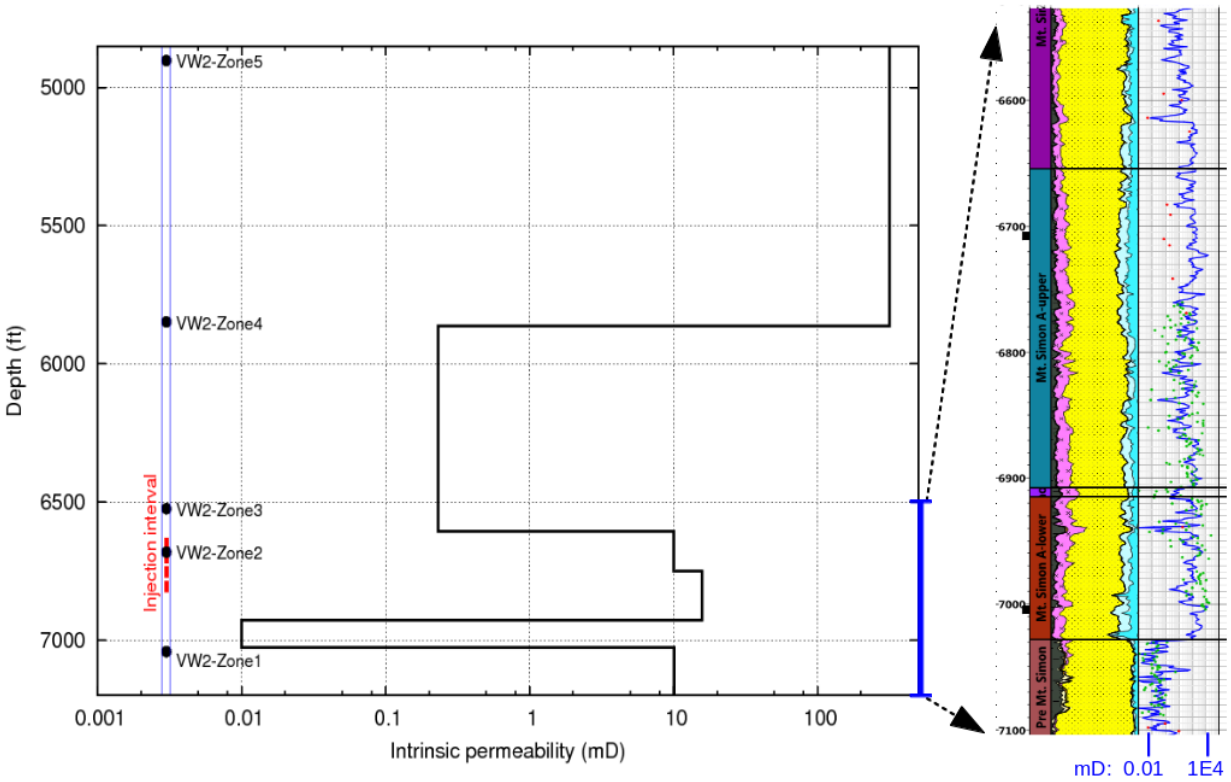

Figure 57. Hydrological inversion for a 6-layer permeability model. Model result shown together with geological section and permeability log.

P-data inversion for one-dimensional fine-structure (83-layer) permeability model

One notes that despite the proximity of Zone 1 to the injector, its increase is as flat as observed for the more distant Zone 4 (Fig. 41). This suggests the presence of a pressure-dampening shielding layer (baffle facies) between Zone 1 and 2. Our above-mentioned search for an optimal model parameter set also strongly indicated the necessity of a thin layer between Zone 1 and 2. These results are consistent with the baffle facies that were introduced in dynamic flow models prior to the CCS2 injection begin. The baffle facies are thin and continuous low permeability zones between Mt. Simon A Lower and Upper, to isolate the pressure response above the Mt. Simon A Lower to Mt. Simon A Upper. Further model refinement by Zaluski & Lee (2019) involved a 3D baffle structure as shown in Fig. 43.

The strong indicators for possibly multi-dimensionally structured low-permeability baffle facies inspired the second model-refinement step. The initial 6-layer model was refined into a much finer parameter set with 83 permeability layer parameters. Each layer has a vertical extent of 5 m.

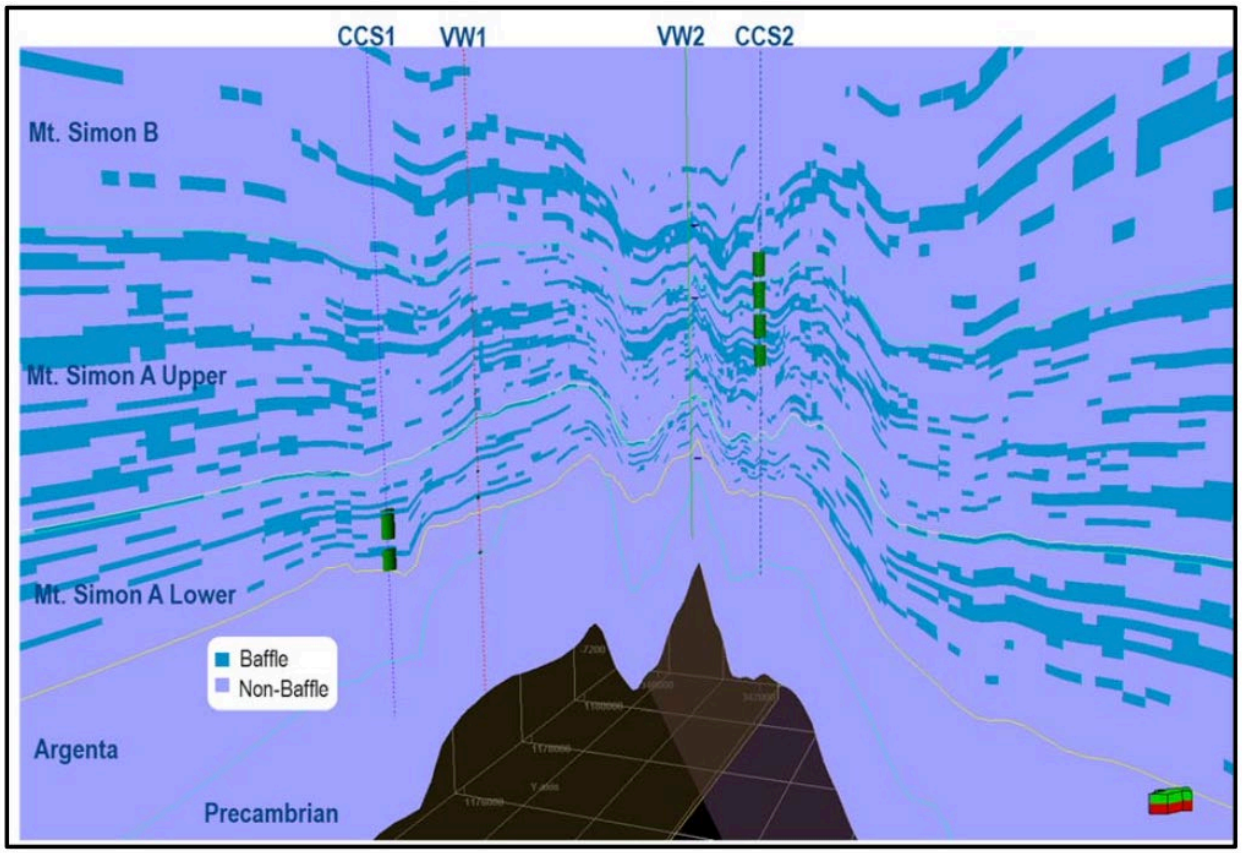

Figure 58. Low permeability baffles within the Mt. Simon formations (figure from Zaluski & Lee, 2019).

Fig. 44 summarizes the final data fits achieved after 18 inversion iterations, where the data fits are calculated from the final iteration's parameter estimates. The higher-fidelity model does not improve the fits of the general pressure amplitude variations in Zone 2 and 3. Fig. 45 compares the vertical permeability trend of the inversions result against permeability logs from well CCS#2. For the depth range 6000-7000 ft, it can be seen that the general trend is approximated by the inversion result. Two likely reasons for disagreement, particularly above Zone 4 are the sparse data coverage above 6000 ft and multi-dimensional permeability structures as indicated by earlier history-matching studies (Fig. 43).

Given the approximation of the general trends, we deem the layered model as an adequate starting model for a subsequent two-dimensional inversion.

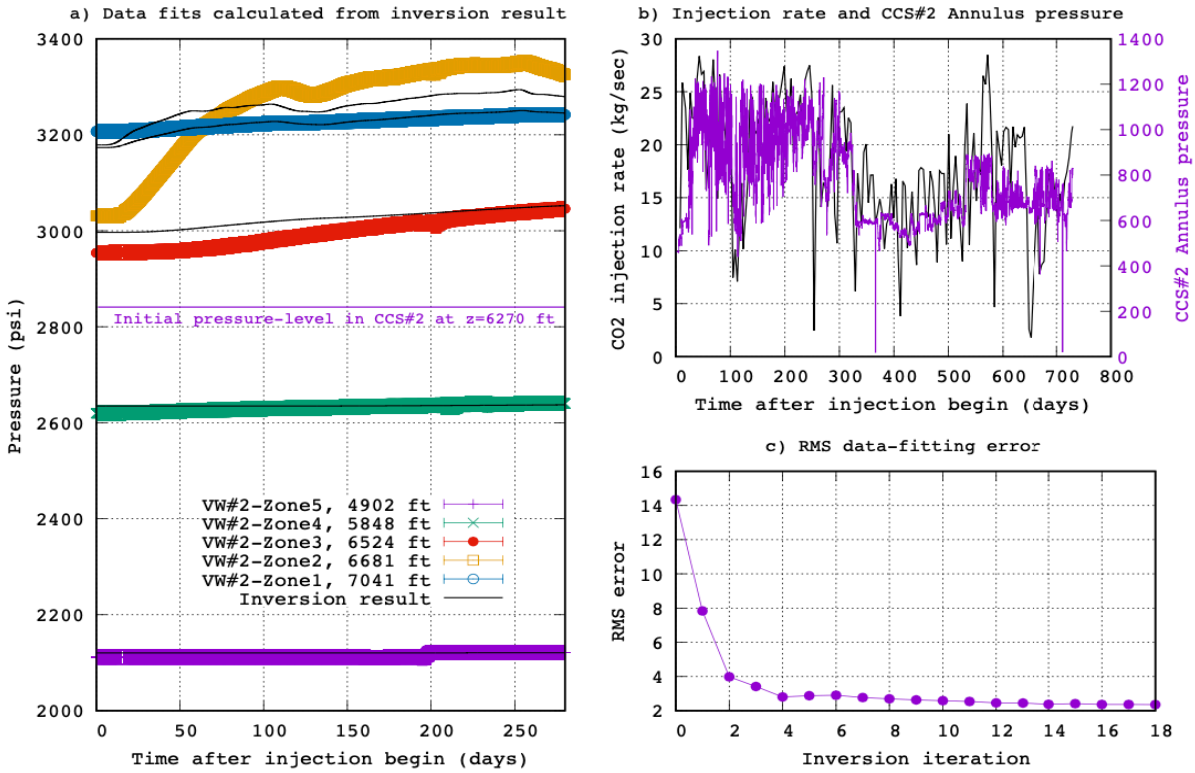

Figure 59. Hydrological inversion for an 83-layer 1D permeability model. (a) Data fits (black curves) are shown together with observations and corresponding error bars. (b) Flow rate (in kg/sec) is shown together with the pressure evolution in CCS#2 (Annulus pressure). (c) Total RMS fitting error over 18 inversion iterations, where the final RMS error is 2.36.

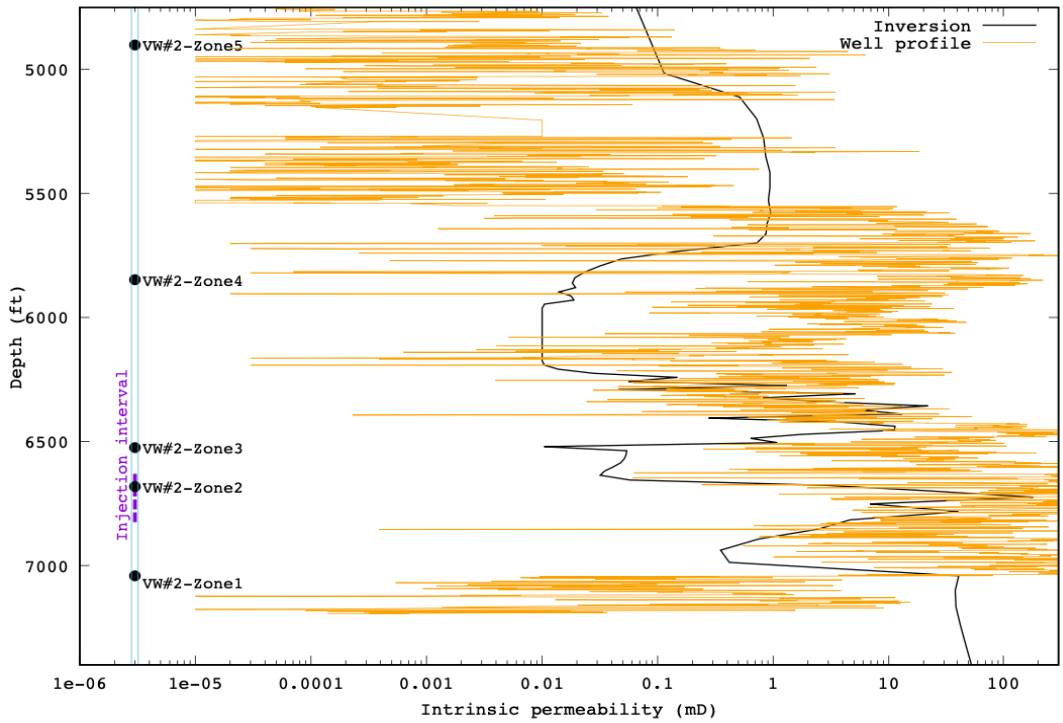

Figure 60. Hydrological inversion for an 83-layer permeability model. Model result (black line) shown together with geological section and permeability log from well CCS#2.

Hydrological inversion for a two-dimensional anisotropic permeability model

The final model-refinement step utilizes the finely layered model outcome of the preceding one-dimensional (83 layers) inversion as starting guess for a two-dimensional (2D) inversion. The 2D model features a parameter refinement within the depth range from 6500 to 6900 ft. Within this zone, 260 mesh-cell parameters cover the refined zone. Their vertical extent is 5 m, while their horizontal size starts at 5 m and increases logarithmically away from the mesh center (at CCS#2). For this inversion, anisotropic permeability is taken into account. Hence, each mesh cell of the inversion domain involves two parameters, amounting to a total of 520 permeability unknowns. The 2D inverse-modeling is ongoing. First results indicate a further RMS error improvement of approx. 10 percent with respect to the final RMS error (2.36) achieved by the 83-layer inversion result (Fig. 59c).

PART 2: Demonstration of the integrated IMS software modules

The second part summarizes the coupling of the hydrological inverse-modeling framework described in Part 1 to the modules used for seismic-data simulation. The most rigorous approach of integrating seismic data into the permeability model estimation is the directly coupled way. This method is outlined in Fig. 8. For this demonstration, we have reduced the reservoir model to a simplified layered model with 5 parameters. Permeability values range from 5E-16 to 1E-14 m^2, that is, 0.5 to 10 mD (Fig. 46a). We simulated a CO2 injection process over a 6-month time period.

Fig. 46b shows the CO2 saturation after a time of 4 months. The inverted seismic data is synthetic, that is, calculated from the true permeability values assumed here (Table 1).

Steps b and c in Fig. 46 constitute the link to the geophysical component, that is, getting a hold of the seismic signature of the evolving CO2 plume shown in Fig. 46b. We have implemented a suite of rock-physics models that essentially transform hydrological properties such as CO2 saturation (S) into rock properties relevant for seismic modeling. Fig. 46c contains a snapshot of the seismic P-wave velocity (V_p) derived from the flow state in step b, using a rock-physics function $V_p=V_p(S)$. Note that other hydrological properties such as water saturation, pressure and temperature also influence the seismic properties. The current implementation allows for choosing different functions for this transformation. Moreover, rock-physics function parameters can be made part of the whole parameter estimation process. However, the latter would require spatially exhaustive data in order to obtain a representative data set for an adequate curve-fitting procedure. This step is not carried out in this demonstration, that is, the rock-physics dependence is fixed and assumed known.

Steps c and d in Fig. 46 represent the geophysical (seismic) modeling component of the IMS. We have implemented two seismic modeling modules, allowing for two degrees of model complexity. The first one is a one-dimensional convolutional modeling approach. Seismic source and earth response functions are treated in the frequency-domain via Fourier transform. This method is computationally fast and thus ideal for feasibility and sensitivity studies. It was employed for the present demonstration.

The second seismic modeling module contains a two-dimensional finite-difference code that allows for full seismic waveform tomography (code name is DENISE version 1.0, written at the Institute of Geosciences, Kiel University, Germany, available in the public domain). This module lets us simulate seismic responses from spatially complex distributions of seismic properties. We have also developed a three-dimensional hydrological permeability model for later purposes. This model was obtained through transformation of the Schlumberger reservoir model into the TOUGH2 formats. The inclusion of the TOUGH2 3D model into the hydrogeophysical scheme is pending. The combination of a 3D reservoir model with the 2D finite-difference seismic modeling component would enable us to estimate very subtle reservoir parameter changes due to the injection process. While a 3D reservoir parameter estimation will require sufficient data coverage, the involved steps are identical to the work flow outlined in Fig. 46.

Our convolutional seismic modeling method allows only for vertically varying seismic properties beneath each common midpoint (the model location where seismic data is measured). Nevertheless, the increasing CO2 saturation causes a decreasing seismic P-wave velocity in the layers at the injection level, as can be seen by the reduced V_p values near the injection zone (Fig. 8c). Different permeability values in the layers near the injection zone would cause different CO2 saturations, thus also causing a footprint in the seismic traces that are influenced by the plume.

Fig. 46c shows a 900 m long surface profile of common midpoints (CMP), where the origin is at the injection zone (location of CCS#2). Seismic traces of length 300 ms calculated from one CMP are shown in Fig. 46d. The true-model response (red curve) stems from the true permeability model

(a). The start-model response (green curve) was calculated from a homogeneous (1E-15 m^2=1 mD) permeability model. The subtle difference between these seismic responses (blue curve) was sufficient to estimate the true permeability model, starting from the homogeneous case as an initial guess. This demonstrates the core IMS component, i.e., the ability to achieve improved reservoir modeling using time-lapse CASSM data.

The whole model-estimating and updating procedure is represented by step e in Fig. 46. Its implementation involves the parallel hydrological parameter estimation method as described above in Part 1. Table 1 summarizes the initial and final model parameters, estimated through the directly coupled seismic-flow modeling process.

Table 5: Permeability layer parameters of the reservoir model. Compared are true model parameters versus starting-model values of the inversion and final estimated values.

Layer parameter number	True value	Starting-model value	Estimated value
1	-15	-15	-15.00
2	-15.3	-15	-15.30
3	-15	-15	-15.00
4	-14.5	-15	-14.49
5	-14	-15	-14.00

Our implementation of the IMS architecture allows for another inverse modeling approach, using traditional full-waveform tomography results as input to the hydrological parameter estimation process. The 2D seismic modeling code DENISE can be used to obtain a spatial CO2 saturation distribution, which can then become input data to a purely hydrological parameter estimation. This process provides an alternative approach for an optimal use of all available monitoring data.

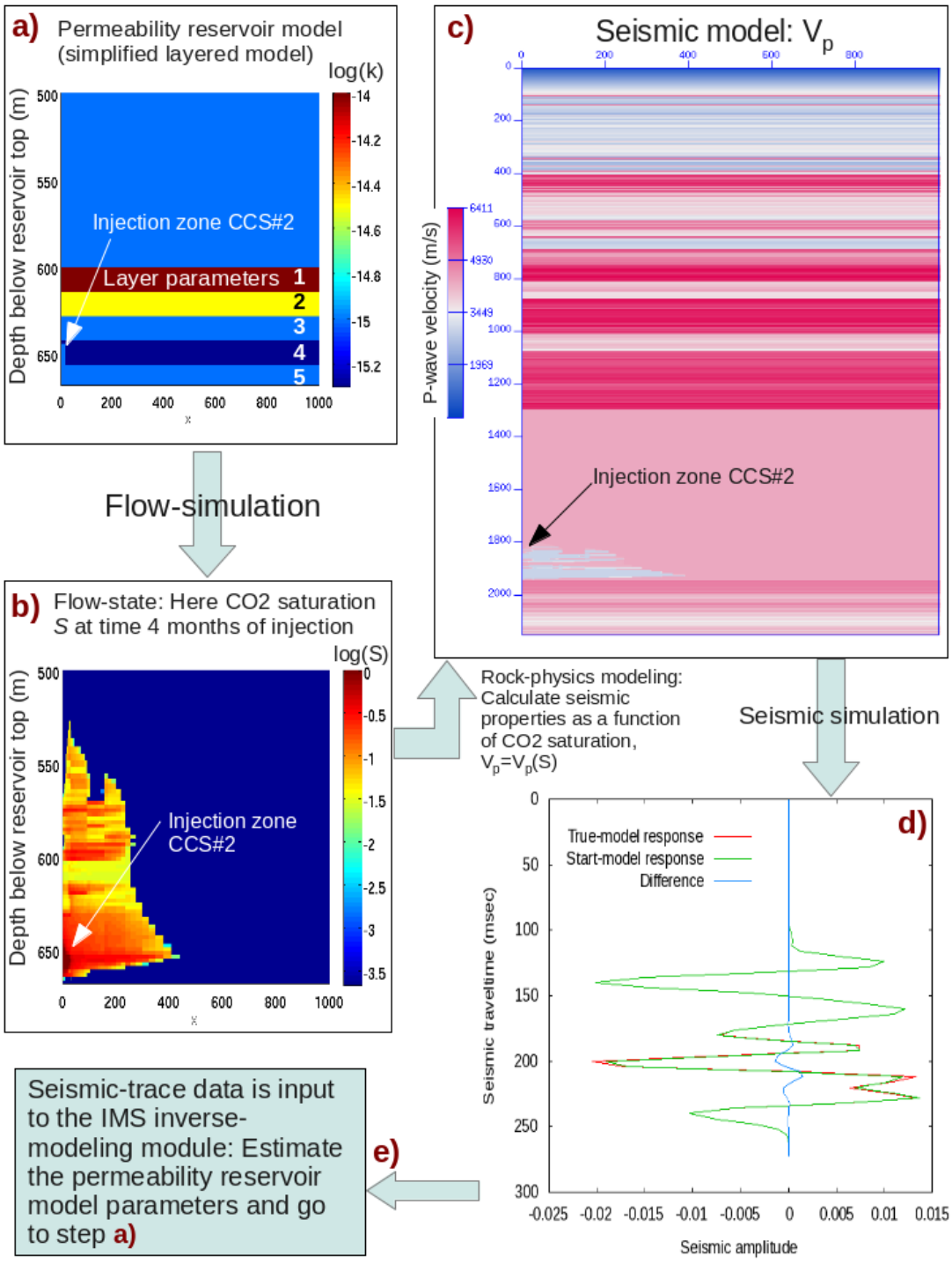

Figure 61. Demonstration of the integrated IMS using synthetic seismic (CASSM) data. The workflow involves hydrological reservoir simulation (a,b) and seismic data simulation (c,d) due to a change in seismic P-wave velocity in the reservoir zone. Shown is the reservoir state and exemplary seismic trace responses after 4 months of CO2 injection (d). The inversion driver involves a deterministic inversion process to update the reservoir model in an iterative manner (e).

5 Lessons learned

CO_2 geosequestration projects require robust long-term monitoring to verify the permanence of emplaced CO_2 and ensure no risk of leakage. The use of DAS coupled with permanent orbital vibrators offers a cost-effective approach for permanent reservoir monitoring. We have built an autonomous seismic monitoring system with DAS and SOV sources at the ADM ICCS project as part of the monitoring of a large-scale CO_2 injection. The system was successfully acquiring data in semi-autonomous fashion for approximately 2 years, with minimum intervention. While the acquisition of the continuous DAS/SOV data was successful, a series of data quality limitations hindered the integration of the DAS/SOV into the monitoring program. Nonetheless, the challenges allowed us to understand the limitations of the system and develop workarounds for some of the issues.

One of the most significant limiting factors on the data quality was the strong angular sensitivity of the DAS method to broadside waves. Although the helically wound cable improved the angular sensitivity, in practice the improvement was not sufficient to detect P-wave reflection from the target interval using a standard single-mode fiber. Additionally, the presence of strong ground roll noise limited the usability of the near-offset sources as the ground-roll was masking any possible reflections. Another aspect that degraded the signal quality was the presence of ghosts in the reference geophone signature. The quality of the source signature improved after installation of the shallower geophone. A last challenge was managing the substantial data flow from the site (6-12 TB/wk); while an on-site processing server with a RAID array was deployed to manage edge analysis needs (e.g. deconvolution & stacking), internet bandwidth at the site was quite limited, resulting in bottlenecks in both quality control and processing parameter testing. While data transfer of raw records on HD via USPS was sufficient for off-line analysis, a more comprehensive solution would be required for deployment of such a system in a commercial monitoring context.

For future deployments of DAS/SOV for seismic reflection monitoring using surface cables, we would make the following recommendations: (1) investigate and model ground roll as part of the process of selecting SOV source locations, (2) install the source recording geophone directly under the SOV at depths shallow enough to avoid ghosting, and (3) use engineered fiber to improve signal sensitivity (Correa et al., 2017). There are other changes that can lead to DAS/SOV improvements that we have noted from work conducted at other field sites. These include developing optimal SOV sweeps, such as a quadratic ramp up in velocity (Correa et al.2021), that flattens the recorded DAS spectrum, as well as options for running larger and multiple motors from a single SOV location. Given the operational success of the ADM DAS/SOV network, the method holds promise for providing cost-effective high-resolution time-lapse seismic data.

6 References

Ajo-Franklin, J., S. Dou, T. Daley, B. Freifeld, M. Robertson, C. Ulrich, T. Wood, I. Eckblaw, N. Lindsey, E. Martin, and A. Wagner, 2017, Time-lapse surface wave monitoring of permafrost thaw using distributed acoustic sensing and a permanent automated seismic source: SEG Technical Program Expanded Abstracts, 5223–5227.

Cheng, F., J. Correa, S. Dou, B. Freifeld, T. Wood, K. Nihei, D. Guerra, J. Birkholzer, B. Chi, and J. Ajo-Franklin, 2021, Testing of a permanent orbital surface source and distributed acoustic sensing for monitoring of unconventional reservoirs: Preliminary results from the Eagle Ford Shale: Geophysics, 86, P1–P12.

Commer, M., M.B. Kowalsky., J. Doetsch, G.A. Newman, and S. Finsterle, 2014. MPiTOUGH2: A parallel parameter estimation framework for hydrological and hydrogeophysical applications, Computers and Geosciences, 65, 127-135.

Commer, M., Pride, S.R., Vasco, D.W., Finsterle, S., Kowalsky, M.B., 2020. Imaging of a fluid injection process using geophysical data - A didactic example, Geophysics, 85, W1-W16.

Correa, J., B. M. Freifeld, R. Revzner, T. Wood, K. Tertyshnikov, and A. Bona, 2018, Continuous DAS VSP monitoring using surface orbital vibrators: Field trials for optimal configuration at the CO2CRC Otway Project: 80th EAGE Conference and Exhibition 2018 Workshop Programme, cp-556-00040.

Correa, J., Isaenkov, R., Y., Sinem, Yurikov, A. Tertyshnikov, K. Wood, T. Freifeld, B., Pevzner, R., 2021, DAS/SOV: Rotary seismic sources with fiber-optic sensing facilitates autonomous permanent reservoir monitoring, Geophysics, Accepted.

Correa, J., A. Egorov, K. Tertyshnikov, A. Bona, R. Pevzner, T. Dean, B. Freifeld, and S. Marshall, 2017, Analysis of signal to noise and directivity characteristics of das VSP at near and far offsets-A CO2CRC Otway Project data example: Leading Edge, **36**, 994a1-994a7.

Daley, T. M., M. Robertson, B. M. Freifeld, D. White, D. E. Miller, F. Herkenhoff, and J. Cocker, 2014, Simultaneous acquisition of distributed acoustic sensing VSP with multi-mode and single-mode fiber optic cables and 3-component geophones at the Aquistore CO 2 storage site: SEG Technical Program Expanded Abstracts 2014, 5014–5018.

Daley, T. M., and D. Cox, 2001, Orbital vibrator seismic source for simultaneous P-and S-wave crosswell acquisition: Geophysics, 66, 1471–1480.

Finsterle, S., Commer, M., Edmiston, J.K., Jung, Y., Kowalsky, M.B., Pau, G.S.H., Wainwright, H.M., Zhang, Y., 2017. ITOUGH2: A multiphysics simulation-optimization framework for analyzing subsurface systems, *Comput. Geosci.*, 108, 8-20.

Gritto, R., T. M. Daley, and L. R. Myer, 2004, Joint cross-well and single- well seismic studies at Lost Hills, California: Geophysical Prospecting, 52, 323–339.

Harris, K., D. White, and C. Samson, 2017, Imaging the Aquistore reservoir after 36 kilotonnes of CO 2 injection using distributed acoustic sensing: Geophysics, 82, M81–M96.

Isaenkov, R., R. Pevzner, S. Glubokovskikh, S. Yavuz, A. Yurikov, K. Tertyshnikov, B. Gurevich, J. Correa, T. Wood, B. Freifeld, M. Mondanos, S. Nikolov, and P. Barraclough, 2021, An automated system for continuous monitoring of CO2 geosequestration using multi-well offset VSP with permanent seismic sources and receivers: Stage 3 of the CO2CRC Otway Project: International Journal of Greenhouse Gas Control, 108, 103317.

Johnston, D. 2013, Practical Applications of Time-lapse Seismic Data, Distinguished Instructor Series, Society of Exploration Geophysicists.

Kaven, J. O., S. H. Hickman, A. F. McGarr, S. Walter, and W. L. Ellsworth, 2014, Seismic monitoring at the Decatur, IL, CO2 sequestration demonstration site: Energy Procedia, 63, 4264–4272.

Köhn, D., De Nil, D., Kurzmann A., Przebindowska, A., Bohlen, T., 2012. On the influence of model parametrization in elastic full waveform tomography. Geophysical Journal International, 191, 325-345.

Kragh, E., and P. Christie, 2002, Seismic repeatability, normalized rms, and predictability: The Leading Edge, 21, 640–647.

Kuvshinov, B. N., 2016, Interaction of helically wound fiber-optic cables with plane seismic waves: Geophysical Prospecting, 64, 671–688.

Lazaratos, S., and B. Marion, 1997, Crosswell seismic imaging of reservoir changes caused byCO2 injection: The Leading Edge, 16, 1300–1306.

Majer, E. L., T. M. Daley, V. Korneev, D. Cox, J. E. Peterson, and J. Queen, 2006, Cost-effective imaging of CO2 injection with borehole seismic methods: The Leading Edge, 25, 1290–1302.

Mateeva, A., J. Lopez, D. Chalenski, M. Tatanova, P. Zwartjes, Z. Yang, S. Bakku, K. de Vos, and H. Potters, 2017, 4D DAS VSP as a tool for frequent seismic monitoring in deep water: The Leading Edge, 36, 995–1000.

Naldrett, G., T. Parker, S. Shatalin, M. Mondanos, and M. Farhadiroushan, 2020, High-resolution Carina distributed acoustic fiberoptic sensor for permanent reservoir monitoring and extending the reach into subsea fields: First Break, **38**, 71–76.

Pevzner, R., M. Urosevic, K. Tertyshnikov, B. Gurevich, V. Shulakova, S. Glubokovskikh, D. Popik, J. Correa, A. Kepic, B. Freifeld, M. Robertson, T. Wood, T. Daley, and R. Singh, 2017,

Stage 2C of the CO2CRC Otway Project: Seismic Monitoring Operations and Preliminary Results: Energy Procedia, 114.

Skov, T., H. G. Borgos, K. A. Halvorsen, T. Randen, L. Sonneland, R. Arts, and A. Chadwick, 2002, Monitoring and characterization of a CO2 storage site: 72nd Annual International Meeting, SEG, Expanded Abstracts, 1669–1673.

Wang, Z., M. Cates, and R. Langan, 1998, Seismic monitoring of a CO2 flood in a carbonate reservoir: A rock physics study: Geophysics, 63, 1604–1617.

Williams-Stroud, S., H. Leetaru, R. A. Bauer, S. Greenberg, and S. Whittaker, 2019, Overview of active and passive seismic data acquisition and monitoring at the Illinois Basin: Decatur project: SEG Technical Program Expanded Abstracts 2019, 4923–4927.

Zaluski, W., Lee, S.-Y., 2019. 2018 IBDP/ICCS Static Geological Model Development and Dynamic Modelling Updates, Schlumberger technical report.

Zhang, K., Wu, Y.-S., Pruess, K., 2008. User's Guide for TOUGH-MP - A massively parallel version of the TOUGH2 code. Report LBNL-315E. Lawrence Berkeley National Laboratory, Berkeley, CA, USA, 108 pp.